ULTRAFAST ALL-OPTICAL SWITCHING AND OPTICAL PROPERTIES OF MICROCAVITIES AND PHOTONIC CRYSTALS

Promotiecommissie:

Promotor:	prof. dr. W. L. Vos
Voorzitter:	prof. dr. G. van der Steenhoven
Overige leden:	prof. dr. K. J. Boller
	prof. dr. C. Denz
	prof. dr. H. J. S. Dorren
	prof. dr. J. M. Gérard
	prof. dr. A. Lagendijk
Paranimfen:	R. Hartsuiker
	dr. ir. B. H. Hüsken

The work described in this thesis is financially supported by the "Nederlandse Organisatie voor Wetenschappelijk Onderzoek" (NWO). This work was carried out in the group *Photonic Bandgaps*, at the *Center for Nanophotonics*, *FOM Institute for Atomic and Molecular Physics* (AMOLF), Amsterdam, The Netherlands, and in the group *Complex Photonic Systems* (COPS), *MESA$^+$ Institute for Nanotechnology* and *Faculty of Science and Technology*, *University of Twente*, Enschede, The Netherlands.

This thesis can be downloaded from *www.photonicbandgaps.com* and *www.amolf.nl*.

Printed: Gildeprint drukkerijen B.V.,
Enschede, The Netherlands.
ISBN: 978-90-77209-35-6

ULTRAFAST ALL-OPTICAL SWITCHING AND OPTICAL PROPERTIES OF MICROCAVITIES AND PHOTONIC CRYSTALS

PROEFSCHRIFT

ter verkrijging van
de graad van doctor aan de Universiteit Twente,
op gezag van de rector magnificus,
prof. dr. H. Brinksma,
volgens besluit van het College voor Promoties
in het openbaar te verdedigen
op vrijdag 1 oktober 2009 om 16.45 uur

door

Alex Hartsuiker

geboren op 3 februari 1980
te Arnhem

Dit proefschrift is goedgekeurd door:

prof. dr. W. L. Vos

Wilt gij naar verre hoogten, gebruik dan uw eigen benen! Laat u niet omhoog dragen*, ga niet zitten op vreemde ruggen en koppen!*

- Friederich Nietzsche, Also sprach Zarathustra -

CONTENTS

CHAPTER 1

Introduction

1.1 Photonic cavities

1.1.1 Principles

Light is essential for myriad processes around us: in nature, to human life, to technological applications, and in everyday appliances. Since light is extremely elusive there is a great interest to store photons in a small volume for a certain time. Storage of photons in an applicable way can be achieved using solid state cavities [1]. Once the light is trapped inside the cavity it can be manipulated. The frequency of the light can for example be converted [2] or a photon can be coupled to a light source to form a new quantum state [3–5].

A schematic representation of light stored in a closed cavity is shown in figure 1.1 A. Since the cavity is closed light stored in the cavity modes do not interact with the environment, also called the bath [6]. The cavity modes have different resonance frequencies and therefore different photon energies. Figure 1.1 A, shows that the light is trapped within a certain volume, the so-called mode volume. The mode volume is an important figure of merit to characterize the quality of the cavity: the smaller the mode volume the more locally the light is stored. A photon trapped in a closed cavity will remain there forever and has therefore an infinite cavity storage time τ_{cav}. Furthermore, the undamped resonance has an infinitely narrow linewidth $\Delta\omega$ as shown in figure 1.1 C. This infinitely small linewidth corresponds to the infinite cavity storage time, given the relation $\tau_{cav} = 1/\Delta\omega$. Figure 1.1 C shows a schematic representation of the spectral solutions of the closed cav-

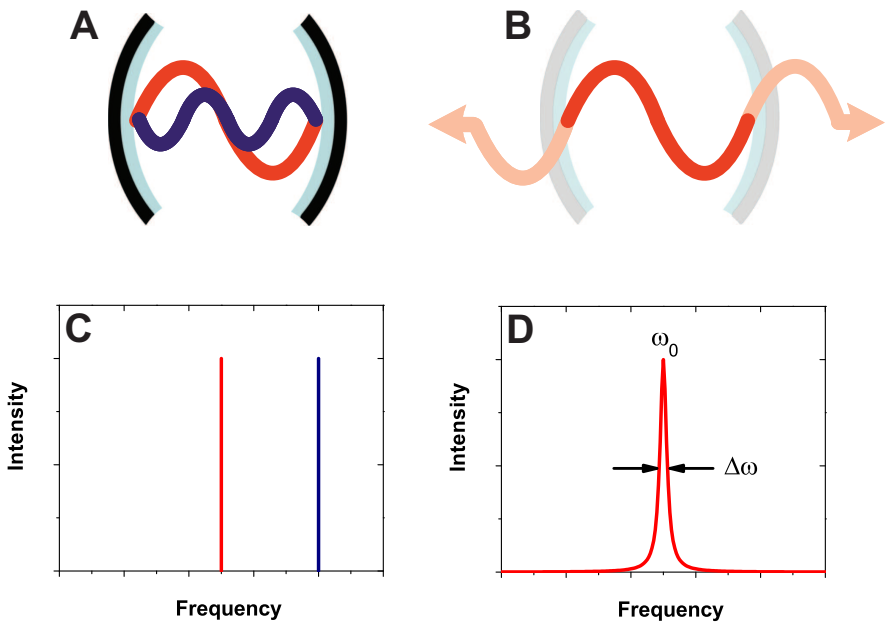

FIGURE 1.1: (A) Schematic representation of a cavity with ideal 100 % reflecting mirrors. No interaction with the environment (bath) is possible, therefore the two shown modes can spectrally be represented as two delta functions as shown in (C). (B) Schematic representation of a cavity with interaction with the environment. The mirrors are not 100 % reflecting, coupling the modes to the infinite number of modes from the environment. Due to this coupling, the discrete modes present in the closed cavity, broaden to a finite width as shown in (D).

ity. Two delta functions at different energies mark the spectral positions of the two modes shown in figure 1.1 A. If the cavity is coupled to the bath by decreasing the mirror reflectivity, the resonances broaden and become finite as does the cavity lifetime. This situation is shown in figure 1.1 B and D. Due to the coupling between the discrete cavity mode and the bath, a continuum of infinitely close spaced modes form the broadened resonance. In the case of an open cavity it is no longer correct to speak of a mode, since a continuum of modes is measured [7]. Therefore, the term 'mode' in this thesis means the broadened resonance composed of an infinite number of infinitely closed spaced modes.

Figure 1.2 A shows the field in an open cavity as a result of a Gaussian input pulse charging the cavity. The field oscillates in time and the amplitude decreases exponentially. Figure 1.2 B shows the intensity in the cavity, which also exponentially decays after the charging pulse is gone. The actual response of the cavity to a Gaussian input pulse is the

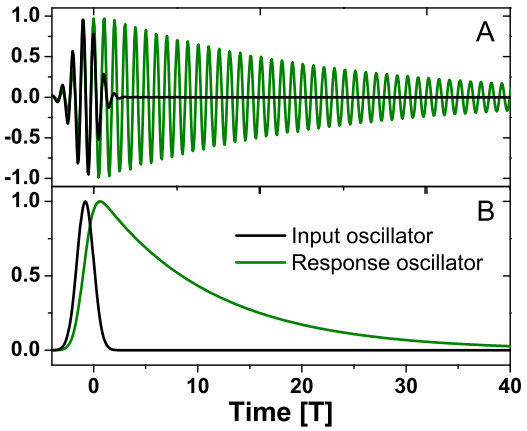

FIGURE 1.2: (A) Field as a function of time. (B) Intensity of an oscillator (light gray) due to a Gaussian shaped input pulse (dark gray). The decay time of the oscillator is given by the quality factor of the oscillator, which is about 40 in this case. The decay time is about 40 times the period T of the field in the cavity. The response of a cavity resonance to a Gaussian input pulse is the same as the oscillator response.

convolution of the response of the cavity to a Dirac pulse and the Gaussian lineshape of the input pulse. The cavity response to a Dirac pulse is an exponential decay with the cavity storage time τ_{cav} as a time constant. The response to the Dirac pulse is given by an exponential decay of the intensity $I(t)$ in the cavity resonance [8]:

$$I(t) = I_0 e^{-t/\tau_{cav}}, \tag{1.1}$$

with I_0 the initial intensity that the pulse stores in the cavity. However, in more complex cavities the behavior of the cavity can be very different from the single exponential case [9]. To compare cavities independent of their resonance frequencies ω_0, the widely used figure of merit is the resonance quality factor Q, which is defined as:

$$Q \equiv \tau_{cav}\omega_0. \tag{1.2}$$

Physically, the quality factor is proportional to the ratio between the total energy stored and the energy lost per cycle. At optical frequencies a cavity with a feasible high quality factor of $Q = 10^6$ [10] stores light with a long response time in the order of nanosec-

onds, but is thus also relatively slow. Conversely, a cavity with a moderate quality factor $Q = 1000$ is fast with a response time of picoseconds. The picosecond timescale allows ultrafast access and storage of light in the cavities.

A common procedure to estimate the quality factor of a cavity is to measure a transmission or reflectivity spectrum and extract Q from the relative linewidth of the cavity resonance [2–4, 10–13]. For a single resonance without dephasing, one can use the Wiener-Khintchine theorem, which relates the field autocorrelate to the intensity spectrum, to obtain

$$Q = \frac{\omega_0}{\Delta\omega}. \tag{1.3}$$

However, if there is significant dephasing, e.g., due to inhomogeneous broadening or thermal noise, $\Delta\omega$ will in general be larger and $Q \geq \omega_0/\Delta\omega$.

From many resonating systems in condensed matter and solid state physics it is known that besides homogeneous broadening there is also the possibility of inhomogeneous broadening of a resonance [6, 14]. In the case of an ensemble of resonators inhomogeneous broadening of a resonance results from inhomogeneities in the resonance frequency. If the resonance frequency is different for each resonator the linewidth of the ensemble is broader than the linewidth of a single resonator and the ensemble linewidth is typically determined by the distribution of resonance frequencies. In the case of inhomogeneous broadening the linewidth will only give a lower boundary for the range of possible Q values. The true quality factor must in this case be determined from dynamic measurements, as is done in chapter 3.

1.1.2 Photonic cavity mirrors

Mirrors form a crucial part of a cavity. They determine the storage time and thereby the quality factor of the cavity. The importance can be made more explicit with another important figure of merit: the finesse of the cavity F^*. The finesse gives the ratio between the free spectral range $\delta\omega$ and the linewidth $\Delta\omega$ of a Fabry-Pérot cavity [14]. The finesse is given by

$$F^* = \frac{\pi\sqrt{R}}{1-R} = \frac{Q}{N}, \tag{1.4}$$

with R the mirror reflectivity and N the order of the resonance [14]. It is clear from Eq. 1.4 that a higher mirror reflectivity leads to a higher finesse and thereby a longer cavity storage time.

Conventional metal mirrors have the disadvantage that they absorb light, which yields a reflectivity in the order of 95 % to 98 %. In this case the maximal finesse is $F^* = 156$, which is equal to the minimum quality factor for normal incidence ($\theta = 0$). Mirrors without absorption therefore are preferable. Semiconductor Bragg mirrors are suitable for this purpose. They consist of stacked semiconductor layer pairs with a well-defined thickness and with a high refractive index contrast, as schematically shown in figure 1.3. The reflec-

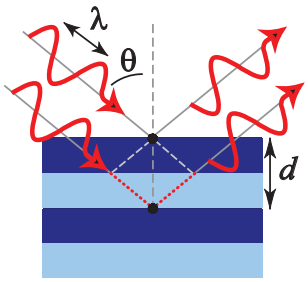

FIGURE 1.3: Schematic representation of reflection of a Bragg stack. The Bragg stack consists of alternating layers of optically equal thickness with high and low refractive index, represented as dark an light colored, respectively. Part of the light impinging on the stack is reflected from the top layer, while part penetrates the structure, reflecting partly from the second interface. The light reflected from the interfaces interferes. If light reflected from the interfaces is in phase it interferes constructively. The Bragg condition is than fullfilled and the penetration length of the light into the stack is given by the Bragg length L_B.

tivity of the Bragg mirror or Bragg stack is the result of interference and scattering of light from the interfaces of the alternating layer pairs. From each layer pair, light is partially reflected and, if the thickness of the layer pairs is chosen well, light reflected from subsequent layer pairs interferes constructively, thereby increasing the reflectivity of the stack. The more layers the stack has, the higher the reflectivity of the stack. The condition for this effect is given by Braggs law, which was first studied in X-ray diffraction experiments on bulk materials [15]:

$$\lambda_0 = 2n_{avg}dcos(\theta), \tag{1.5}$$

with λ_0 the center wavelength of the reflected band of light, n_{avg} the effective refractive index of the stack, d the thickness of a layer pair, and θ the angle of incidence. It is clear from Eq. 1.5 that the wavelength of the Bragg reflection depends on the angle of incidence. The bandwidth of the Bragg reflection is given by the photonic strength S,

which is defined as the ratio of the polarizability of each structural unit cell to the physical volume [16]. The photonic strength can be identified with the relative bandwidth $\frac{\Delta\omega}{\omega}$ of a stopgap [17], which leads to the expression:

$$S = 3\Phi\frac{m^2-1}{m^2+2}g(K,r), \tag{1.6}$$

where Φ is the volume fraction of high index material, m is the ratio of the refractive indices and $g(K,r)$ is the structure factor [18]. It is clear from Eq. 10.6 that the photonic strength increases when the refractive index contrast increases or when the average refractive index decreases [19]. A higher photonic strength means that the contribution of a layer pair to the total reflection of the stack is larger. The characteristic length for the

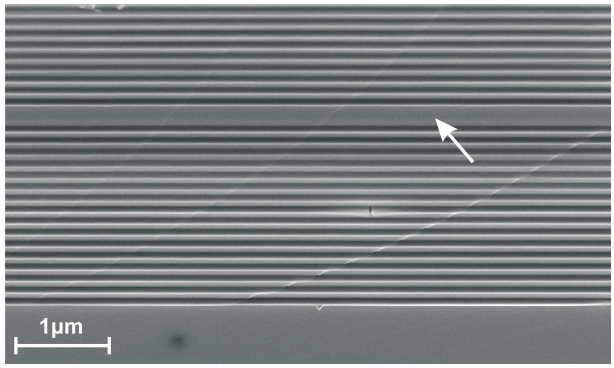

FIGURE 1.4: Scanning electron micrograph of planar microcavity. The microcavity consists of a λ-thick GaAs layer (indicated by the white arrow) sandwiched between layers of AlAs (light) and GaAs (dark) on a GaAs substrate. Structure made by group of J.M. Gérard at CEA Grenoble [20].

intensity reflectivity of a stack is the Bragg length L_B, which is given by

$$L_B = \frac{2d}{\pi S}. \tag{1.7}$$

It is clear that the Bragg length becomes shorter if the photonic strength increases. The reflectivity R of a Bragg mirror is now determined by the thickness L and the Bragg length by

$$R = 100\%\left(1-\exp\left(-\frac{L}{L_B}\right)\right). \tag{1.8}$$

From Eq. 1.8 we can see that the reflectivity of a Bragg stack can approach 100 % given that the stack is infinitely thick. With a sample thickness 5 times the Bragg length $\frac{L}{L_B} = 5$, the reflectivity of the stack is already 99.3 %, similar to what we find in our experiments.

A realization of a cavity with Bragg stacks as mirrors is shown in the scanning electron micrograph in figure 1.4. The Bragg stacks consist of alternating $\lambda/4$ layers of GaAs (light) and AlAs (light) layers on top of a GaAs substrate. Sandwiched between the two Bragg stacks is a λ-thick GaAs layer [20]. The λ-layer is as a planar defect that breaks the crystal symmetry of the Bragg stack [21].

The dispersion relation of light is strongly modified by the structure of the stack and is given together with the linear homogeneous medium dispersion relation in figure 1.5 A. The stack's dispersion relation bends in the vicinity of the Bragg relation, which is

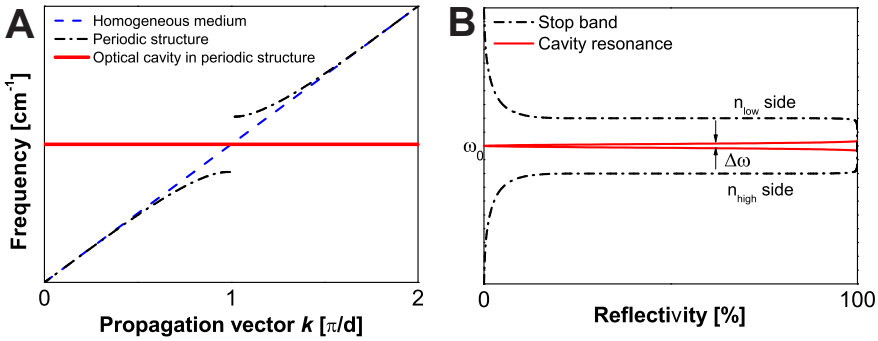

FIGURE 1.5: (a) Dispersion relation of light in a homogeneous medium (dashed line), a periodic structure (dash dotted lines), and an optical cavity in a periodic structure (solid line). The dispersion relation of the homogeneous medium follows a straight line whereas the photonic crystal shows a stopgap $\Delta\omega$. The mode at ω_0 that is present in the stopgap is a result of an optical cavity. (b) Schematic representation of the reflectivity spectrum of a periodic structure. The stopband is visible (dash dotted line) at the frequencies of the stopgap $\Delta\omega$, as indicated with the dotted lines. The stopband has 100% reflectivity, while the cavity results in a trough at the resonance frequency ω_0 (solid line).

fulfilled at a wavevector with a modulus k = π/d. At k = π/d a gap opens up in the dispersion relation with a width determined by the photonic strength S. This modification of the dispersion relation can be attributed to the Bragg stacks. In the middle of the gap a band of modes is present, indicated by the line [22]. This band of modes is the result of

the planar defect layer, which breaks the symmetry of the Bragg stacks. Thereby confined states, which act as cavity, are created inside the gap. The width of the band is determined by the cavity storage time τ_{cav}. If we would measure a reflectivity spectrum of such a structure it would schematically look as shown in figure 1.5 B. A stopband with a width determined by the photonic strength appears in the spectrum. In the stopband a trough due to the cavity resonance is present.

From figure 1.5 A it is clear that at the edges of the stopgap and at the cavity resonance light is not propagating, since the bands are flat. At the edges of the stopband the standing waves are dominantly in the high and low index material, respectively [21]. The field profile on resonance calculated by finite difference time domain simulation is shown in figure 1.6 A [23]. The stack is shown above the cavity and the edges of the cavity and

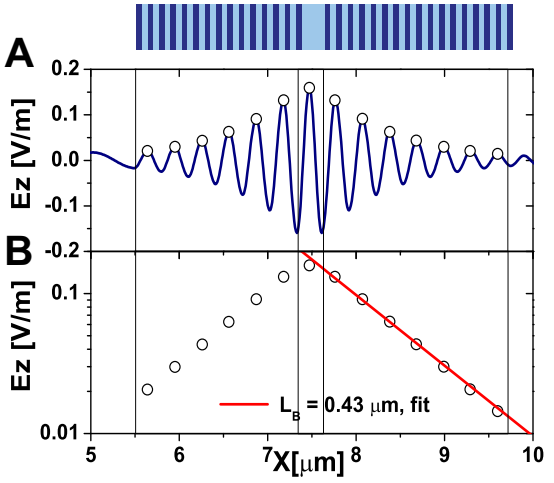

FIGURE 1.6: (A) Calculated spatial field distribution in the cavity stack. The circles indicate the amplitude of the field, plotted in (B) on a log scale. The dashed line gives a fit to the spatial field distribution, the solid line gives the field distribution expected from the calculated Bragg length. FDTD simulation courtesy of Allard P. Mosk

stack are represented as solid lines inside the figure. Inside the stack the fields oscillates with an amplitude that decreases into the mirrors. The amplitude of the field is shown on a log scale in figure 1.6 B, showing that the amplitude decreases exponentially with distance

from the mirror. The field penetration into the stacks is given by the Bragg length:

$$Ez(x) = Ez_0 \exp\left(\frac{-x}{2L_B}\right). \tag{1.9}$$

From the fit to the data we find a Bragg length of $L_B = 0.43\ \mu m$, which surprisingly differs from the calculated value of $L_B = 0.82\ \mu m$. We have currently no explanation for the difference. We calculated the Bragg length by substituting $S = \frac{4}{\pi}\left|\frac{n_{GaAs}-n_{AlAs}}{n_{GaAs}+n_{AlAs}}\right|$ and Eq. 1.5 for normal incidence ($\theta = 0$) into Eq. 1.7, yielding

$$L_B = \frac{|n_{GaAs} + n_{AlAs}|}{|n_{GaAs} - n_{AlAs}|}\frac{d}{2}. \tag{1.10}$$

The expression for the photonic strength that we have used is valid for a Bragg stack with $\lambda/4$-thick layers [24].

From this section we conclude that the confinement in the axial direction is given by the Bragg length. In the transversal direction the structures we discussed so far are infinite. To obtain a smaller mode volume it is necessary to also confine the resonances laterally. The lateral confinement can be achieved using micropillar resonators.

1.1.3 Three-dimensional confinement of light

For lateral confinement of the cavity resonance the cavity stack is structured into micropillar resonators. As in an optical fibre, due to internal reflection of light at the air-micropillar interface, the resonances are confined [25]. Figure 1.7 shows the combination of the pillar and Bragg stack schematically. As in an optical fibre, spatial field profiles emerge for each resonance, by laterally confining the cavity resonances. An example of this is given in the schematic micropillar resonator shown figure 1.7. The field pattern that is shown corresponds to the fundamental micropillar resonance and has a maximum in the middle and a minimum at the edges. Micropillar resonators can very well be modeled using the theory for Bragg stacks and for waveguiding theory as shown in chapter 7 and [20, 26]. Figure 1.8 shows a scanning electron micrograph of a micropillar resonator with a diameter of 6 μm. The layers of the Bragg stack can be recognized at the side of the pillar. The ring pattern at the base of the pillar result from the fabrication process.

Micropillars cavities consist usually of GaAs/AlAs layers [3, 20, 27, 28], but also pillars with HfO_2/SiO_2 layers for operation in the ultraviolet are reported in literature

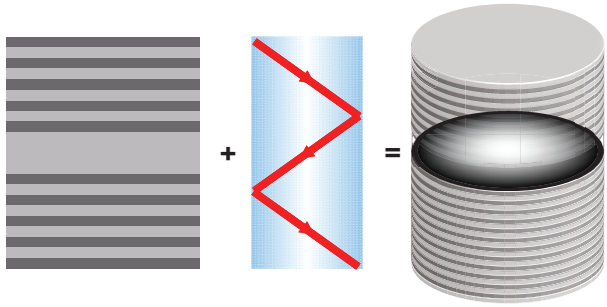

FIGURE 1.7: Schematic representation of the model of a micropillar cavity: a micropillar cavity can be thought of as a combination of a planar microcavity which is laterally confined like a fiber. Due to this lateral confinement, the micropillar cavity supports multiple resonances like a fiber, depending on the diameter of the pillar. Each resonance has its own field profile, an example of which is shown in the micropillar cavity.

[29]. Typical quality factors are in between 4.000 and 10.000, but even quality factors exceeding 150.000 are observed [28]. The mode volumes are in the range of 0.3 μm^3 [25]. In chapter 7, we present a method to optically address a single mode in a multimode micropillar cavity.

Another way of in-plane confinement is to fabricate a two- or three-dimensional photonic crystal with a point defect as shown schematically in figure 1.9. The structure shown in figure 1.9 confines light in-plane. Not only in the two directions shown in the Bragg stacks, but also in all other directions light is Bragg reflected. The crystal shown in figure 1.9 can be extended to the third dimension. Extending the structure in three dimensions

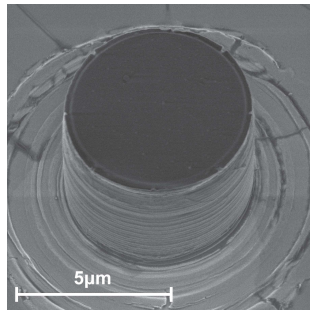

FIGURE 1.8: Scanning electron micrograph of a micropillar cavity on a GaAs substrate. Careful observation shows the GaAs AlAs layers of the cavity. The rings at the base of the pillar result from the fabrication process.

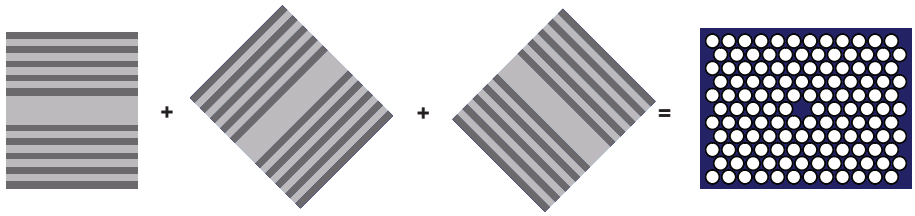

FIGURE 1.9: Schematic representing three planar microcavities that behave like a two-dimensional photonic crystal. A two-dimensional point defect breaks the crystal symmetry and acts as a two-dimensional cavity.

means that the circles in figure 1.9 become spheres and that the symmetry of the circles also extends into the third dimension. Ultimate three-dimensional confinement of light thus requires the realization of a point defect in a three-dimensional photonic bandgap crystal [30]. Interesting steps towards the fabrication of such cavities have been made by [31, 32]. Figure 1.10 A shows the first ever realization of a three-dimensional silica

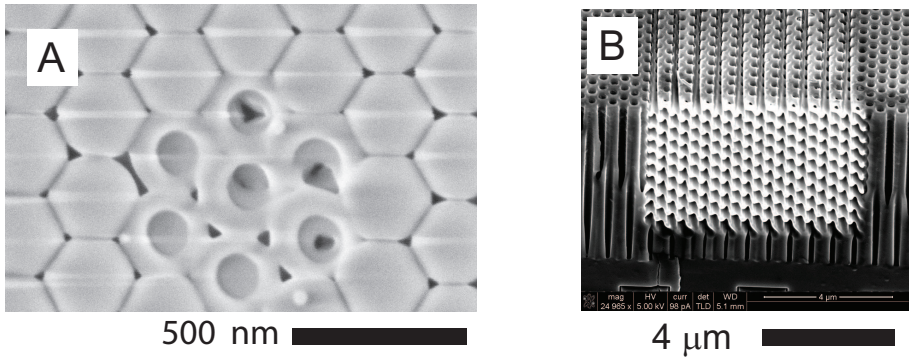

FIGURE 1.10: (A) Scanning electron micrograph of a silica opal with an intentional point defect that will act as a cavity [33]. The silica opal functions as a mirror. The mirror around the cavity becomes three dimensional if a second layer of opal photonic crystal is grown on top of the layer shown in the micrograph. (B) Scanning electron micrograph of a three-dimensional silicon photonic crystal. The larger array of vertical pores is etched using reactive ion etching, while the horizontal set of pores is etched using a focussed ion beam [34].

opal photonic crystal with an intentional point defect, consisting of 7 holes milled with a focussed ion beam [33]. On top of this structure additional layers of opal photonic crystal can be grown to bury the defect and thereby creating a photonic nanocavity in a

three dimensional photonic crystal. In chapter 10, we will extensively study the properties of opals that act as three-dimensional cavity mirrors. Figure 1.10 B shows a silicon three-dimensional photonic crystal milled in a two-dimensional photonic crystal with a focussed ion beam. The two-dimension photonic crystal consists of vertical pores in a crystal structure as shown in figure 1.9. In the bright area in figure 1.10 B a new set of pores is milled perpendicular to the holes with a focussed ion beam. In this way a three dimensional woodpile photonic crystal is created. A photonic cavity can be created by locally breaking the crystal symmetry, for example by not etching one of the horizontal and one of the vertical pores. On the intersection of these pores a local field enhancement as in a cavity is expected [34].

1.2 Light source in a cavity

1.2.1 Spontaneous emission control

It is known that an elementary light source such as an atom emits a photon either spontaneously or stimulated by an external field [35]. It is also well-known that the rate of spontaneous emission is not an immutable property of an atom [36, 37]. The rate also strongly depends on its surroundings. In quantum mechanics, the rate of spontaneous emission of an excited two-level atom is described by Fermi's golden rule [38]: the rate is determined by a product of atomic matrix elements of the dipole operator with the local density of optical states (LDOS), that typifies the surroundings. The LDOS is thereby a measure of the number of modes in which a photon can be emitted, and it can be interpreted as the density of vacuum fluctuations at the atom's position. It should be noted that Fermi's golden rule is not exact but is a weak-coupling approximation [6, 39], that is, the bath does not act back on the source. A main feature of spontaneous emission is its dynamics: an emitted photon is measured at a random time after the atom is excited with a short pulse. Both the distributions of emitted photons and of the excited-state population decay exponentially in time, and are determined by the decay rate [40].

A well-known tool to modify the average spontaneous emission rate of a source in the frequency domain is a resonant cavity tuned to the source's emission frequency. At the cavity resonance, the local density of optical states has a distinct peak that increases the emission rate. It was first realized by Purcell that the emission rate of an atom can be increased [41], known as the Purcell effect. The Purcell factor F_p gauges the change

of the radiative emission rate Γ_{cavity} in a cavity relative to the rate Γ_0 in a homogeneous medium: $F_p \equiv \Gamma_{cavity}/\Gamma_0$. Following the pioneering work by Gérard et al. [11], many groups have demonstrated the Purcell effect with quantum dots embedded in solid-state microcavities [1, 27]. To date, impressive progress has been achieved in controlling spontaneous emission in the frequency domain with nanophotonic structures. Recently, this progress has culminated in the observation of vacuum-Rabi splitting of a quantum dot in a cavity [3–5]. In this situation, the weak coupling limit is broken: the quantum dot resonance and the cavity resonance hybride to form novel states of matter that show promise for, e.g., quantum information processing [42].

1.2.2 Ultrafast spontaneous emission switching

In all microcavities and photonic crystals, however, the control is stationary in time. Thus, the distribution of emitted photons and the emission rate do not change in time. Therefore an important motivation for this thesis is to take steps to modify or "switch" spontaneous emission ultrafast on time-scales faster than the atoms' typical lifetime [43]. Eventually, we anticipate that a strongly and quickly modulated bath is no longer a bona-fide bath. This will lead to novel ultrafast quantum electrodynamics where the weak-coupling limit is broken in the time domain.

Figure 1.11 A and B show schematically a cavity with time-dependent properties that change the emission of the light source in the cavity, depicted by a sphere. By changing the cavity resonance the emitter can be switched on or off resonance. In figure 1.11 A the cavity resonance has a different frequency than the emission frequency of the source in the cavity. When the cavity is switched such that the cavity resonance is equal to the emission frequency of the source see figure 1.11, the emission intensity increases. The increase results from the Purcell effect, which is shown to increase the decay rate for emitters on resonance. Since the emitted intensity is related to the decay rate, an increase in emitted intensity is to be expected for an emitter that is switched on resonance. This will be treated in more detail in chapter 8. An interesting feature of switching of spontaneous emission on time scales faster than the sources' lifetime is that we predict a burst of spontaneous emitted light. Thereby a certain determinism is introduced in an otherwise random quantum process.

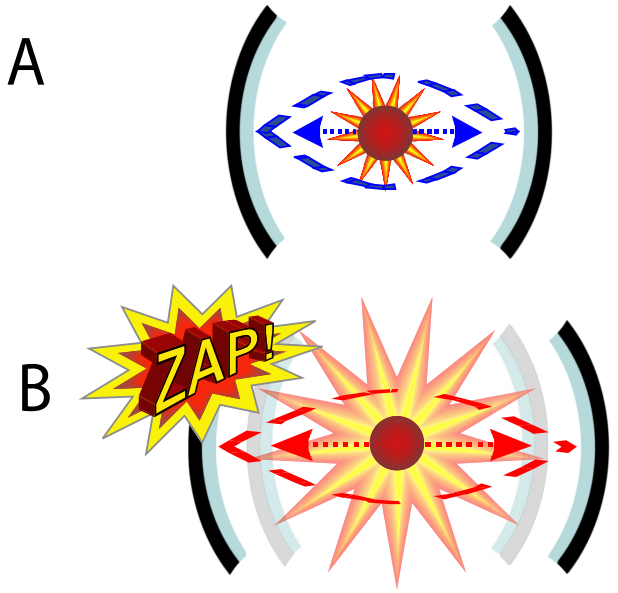

FIGURE 1.11: Schematic representation of switching an increase of emitted intensity if the cavity properties are switched. In the unswitched cavity (situation A), the source emits little light since the cavity resonance (dashed standing wave) is blue shifted compared to the light source. In the switched case, light is emitted with high intensity from the source, since the cavity resonance matches the emission wavelength of the source.

1.3 Ultrafast switching of a microcavity

1.3.1 All-optical switching mechanisms

We have investigated microcavities as shown in figure 1.4 and figure 1.8. In order to all-optically switch the properties we employed two switching mechanisms. The first mechanism comprises the well-known excitation of free carriers by an intense pump pulse and is discussed in chapter 4 and chapter 6. In the case of free-carrier excitation the refractive index is given by the Drude model for moderately high densities of excited free carriers [13, 24, 44–47]. We have studied the dynamics of the switched cavity as a result of the dynamics of the excited carriers. For the instantaneous switch of the structure, the refractive index is given by Kerr coeffcient [48–50, 89].

While free carrier switching is a powerful and fast mechanism, its speed is limited by material properties. Ultimate-fast instantaneous switching could be feasible by the electronic Kerr effect. However, the electronic Kerr effect is believed to be too weak to

switch a photonic cavity [43]. We explore in chapter 5 the Kerr switching of a photonic microcavity in both the photonic regime as in the long wavelength limit. To the best of our knowledge we demonstrate for the first time ever the Kerr switch of a cavity. The high speed of the Kerr switch could be of interest for high frequency data modulation [52].

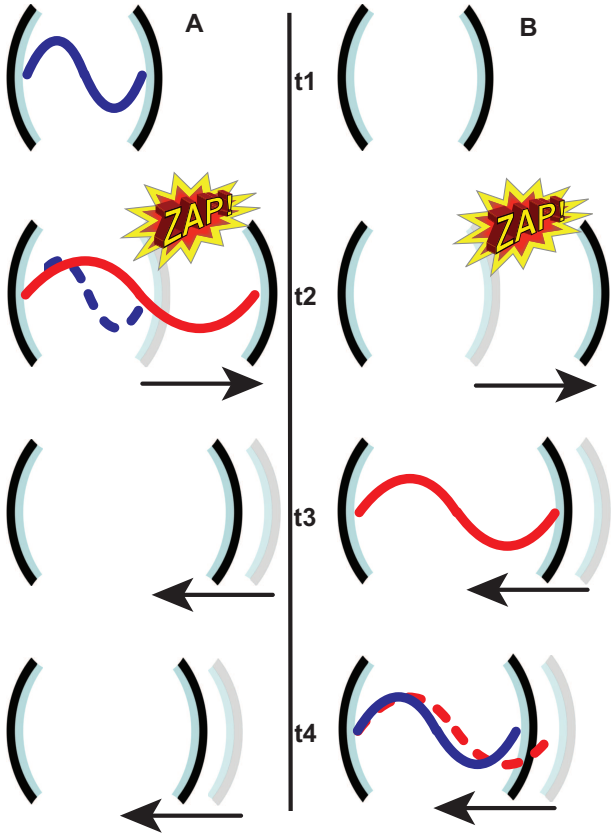

FIGURE 1.12: (A) Schematic representation of a loaded cavity that is switched. The blue light that is stored in the cavity red- shifts due to the switched cavity resonance. The empty cavity relaxes to its original resonance wavelength. (B) Schematic representation of an empty cavity that is switched. When the cavity is switched and relaxes to its original resonance wave- length, the cavity is loaded with photons. During the relaxation, the photons change color in absence of a pump pulse.

1.3.2 Light conversion in a switched optical microcavity

In order to manipulate light stored in a photonic crystal cavity it is necessary to change the cavity properties in time. Two different schemes for manipulating light by changing the cavity properties are shown in figure 1.12 A and figure 1.12 B. In scheme A light is stored in the cavity at time *t1*, after which the cavity resonance is changed at time *t2*. Light is in the cavity and its wavelength and thereby color is changed during the switch. At later times *t3* and *t4* the now empty cavity relaxes back to its initial state. Switching the cavity resonance can be achieved using a high intensity optical pump pulse. In scheme A it is essential that the pump pulse overlaps in both space and time with the light stored in the cavity [2, 53, 54]. Overlap in both space and time is also necessary in more conventional schemes like nonlinear optics, where a pump and probe pulse are overlapped in a nonlinear crystal [48, 55].

In scheme B the cavity is empty at time *t1* and its optical resonance frequency is switched using an optical pump pulse at time *t2*. When the pump pulse is gone, the cavity is loaded with another light pulse, which remains in the cavity during the cavity storage time, while the cavity relaxes to its initial state. During the relaxation of the cavity the wavelength and thereby the color of the stored light changes. The new feature in scheme B is that no overlap in space and time is needed between the pump and probe pulse. Scheme A and B while be discussed in more detail in chapter 6.

CHAPTER 2

Experimental setups and samples

2.1 Introduction

Photonic crystals have a strong interaction with light. They are composite dielectric structures with a periodicity in the order of the wavelength of light. Examples of state of the art microscopic photonic crystals are shown in figure 2.1. Figure 2.1 A shows a scanning electron microscope (SEM) picture of a three-dimensional silicon inverse woodpile photonic crystal (light colored pores perpendicular to vertical pores) embedded in a two-dimensional silicon photonic crystal consisting of 7 μm deep vertical pores. The crystal was made by first dry etching a large set of pores [56]. Subsequently, a second set of pores, perpendicular to the first set, was etched with a focussed ion-beam. The resulting photonic crystal is the most strongly interacting photonic crystal [57]. Figure 2.1 B shows a field of micropillars with different radii ranging from 1 μm to 20 μm. The micropillars consist of a λ-thick GaAs layer sandwiched between two Bragg stacks made from alternating $\lambda/4$ GaAs and AlAs layers. We will discuss in the next section the fabrication of planar microcavities. The reason is that these cavities are used throughout this thesis and form the basis for the micropillar cavities that are treated in chapter 7.

The structural properties of photonic crystals and cavities are usually studied with a scanning electron microscope (SEM), while the photonic properties of the photonic crystals are assessed by optical reflectivity or transmission measurements. The reflectivity and transmission spectra contain optical information on the photonic properties of the samples, such as the spectral position of the stopgap. The thickness of the sample can also

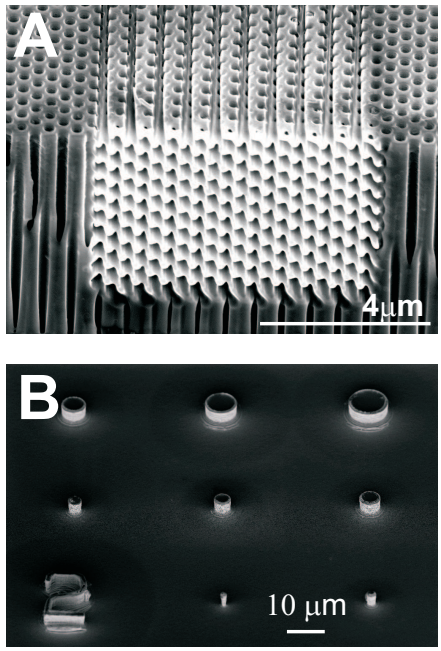

FIGURE 2.1: *(A) Silicon three-dimensional photonic crystal of $5\mu m \times 5\mu m \times 5\mu m$. The vertical pores are etched with reactive ion etching [56], while the horizontal pores are etched with focussed ion-beam milling. Picture by courtesy of R. W. Tjerkstra. (B) SEM picture of a field of micropillars consisting of a λ-thick GaAs layer sandwiched between two Bragg stacks made from $\lambda/4$-layers of GaAs and AlAs. Picture by courtesy of J. C. Claudon [20].*

be derived, if the measured spectrum contains Fabry-Pérot fringes [58]. In this chapter we describe the reflectivity microscope that is used in this thesis for linear reflectivity and transmission measurements. We also describe an ultrafast two-color pump-probe setup, which we use to switch planar microcavities. With the latter setup both time- and frequency-resolved broadband measurements are feasible.

2.2 Fabrication of planar microcavities

We have studied two microcavity samples, one with a resonance near λ = 980 nm and one near 1300 nm. The 980 nm and 1300 nm structure consist of a GaAs λ thick layer sandwiched between two Bragg stacks consisting of 12 and 16 pairs of $\lambda/4$ thick layers

of nominally pure GaAs or AlAs. The thickness of the λ-layer is 277 nm in the case of the 980 nm sample and 373 nm in the case of the 1300 nm sample. The same 980 nm structure was studied in [13, 59]. A scanning electron micrograph of the 1300 nm cavity is shown in figure 2.2. The alternating layers of GaAs (light gray) and AlAs (dark gray)

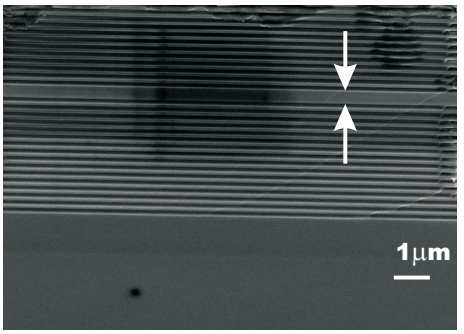

FIGURE 2.2: *Scanning electron micrograph of the microcavity with a resonance at 1300 nm. A λ-thick layer, indicated with white arrows, is sandwiched between two Bragg stacks. The GaAs substrate is visible at the bottom.*

can clearly be seen. The λ-thick cavity layer is indicated with two white arrows. The samples are grown with molecular beam epitaxy at 550°C to optimize the optical quality [20]. For experiments outside the present scope the samples were doped with 10^{10}cm^{-2} InGaAs/GaAs quantum dots, which hardly influence our experiment [(1)]. There is a spatial gradient in the cavity thickness of the 980 nm sample $\frac{\delta d}{\delta x} = 5.64$ nm/mm [59]. The spatial gradient results in a position dependent resonance frequency. In our measurements we average the transmitted intensity over the area of the focal spot. The different resonance frequencies cause the resonance to broaden inhomogeneously.

2.3 Broadband reflectivity microscope

Typical conventional opal photonic crystals have dimensions in the order of 100 μm, but state of the art photonic crystals and micro pillar cavities made with nanofabrication techniques have dimensions in the order of 1-10 μm. In order to measure the reflectivity of

[(1)] The maximum unbroadened refractive index change of the dots amounts to only 10^{-8}, while the absorption at resonance is less than 0.02 cm^{-1}.

such small structures we need a focus diameter comparable and preferably smaller than the photonic structures (see for example chapter 7 and chapter 9). If the focus is larger, the reflected spectrum will not be solely from the sample, which complicates analysis. Furthermore, we need to accurately position the focus on the photonic sample. For the small dimensions of our structures a dedicated setup is necessary.

We have designed and built a new reflectivity setup dedicated to focussing white light with a broad spectrum onto structures with 5 μm width and height, and positioning the focus in a controlled way. To achieve this we used a broadband supercontinuum white-light source, actuators with high resolution, a built-in microscope, and a Fourier Transform Interferometer (FTIR). The setup was tested by measuring the reflectivity spectra of aluminum, silver, and gold mirrors and a well known photonic sample, namely a woodpile photonic crystal. The latter sample has been studied extensively by Euser and Molenaar [24, 60].

2.3.1 Reflectivity

The setup used to measure reflectivity spectra is shown schematically in figure 2.3. The

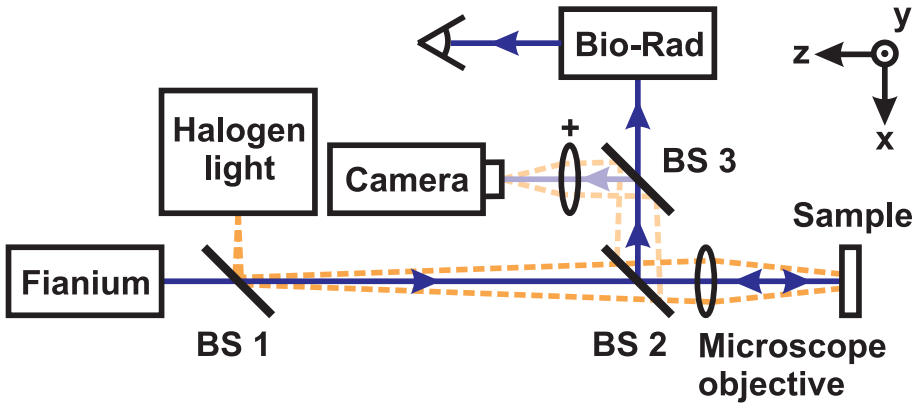

FIGURE 2.3: *Schematic of the reflectivity setup with Fianium supercontinuum white-light source, Biorad Fourier-transform spectrometer, and the microscope with the CCD camera.*

setup consists of a Fianium supercontinuum white-light source, a Fourier-transform spectrometer (Biorad FTS6000), a CCD camera (Dolphin F145b), a xyz automated translation stage and optics to guide the beam to the sample. The Fianium supercontinuum white-

light source has an output power of 2 W and an output wavelength range from 450 nm to 2500 nm. The light source is pulsed, with a pulse duration of 2 ps. The repetition rate of the white light source is 20 MHz. Since white light is generated in a fiber, the beam is highly collimated and can be focussed down to 2 μm, the output fiber diameter. A 2 μm focus is difficult to achieve with conventional white light sources, since a pinhole with a diameter of 2 μm in a collimator is needed. Due to this small pinhole very little light from the light source is transmitted through the collimator thereby decreasing the available power and the signal to noise ratio. The Fourier-transform spectrometer is similar to the one used by Thijssen *et al.* [61]. The resolution of the spectrometer is 1 cm^{-1}. With the automated translation stage it is possible to position the sample with 50 nm precision in all three directions. Automated positioning is necessary since the dimensions of the structures and the focus length is in the order of a few μm. We used aluminum mirrors to guide the beam to the sample. The type of detector used for the measurement was selected based on the spectral region of interest. Examples are Si, InGaAs and InAs diodes.

To be able to focus onto the small photonic crystals we built a microscope into the reflectivity setup. To view the sample it is illuminated through a gold-coated dispersionless reflecting microscope objective (Ealing X74) with numerical aperture NA = 0.65 by halogen light. Light reflected from the sample is collected by the same microscope objective and focussed onto a CCD camera with a 200 mm tube lens. The sample can be positioned with an accuracy of 50 nm using a translation stage and three motorized actuators. The camera is discussed in more detail in section 2.3.3

2.3.2 Characterization reflectivity measurements

The reflectivity spectra of the aluminum (Thorlabs, FP10-03-F01) and silver mirrors (Thorlabs, FP10-03-P01) are shown in figure 2.4. The reflectivity is gauged with the spectrum of a gold mirror. Both the aluminum and the silver mirror show a flat reflectivity spectrum at 100 % and 102 %, respectively. This agrees with the larger reflectivity of silver compared to gold. Furthermore, the reflectivity spectra of both the aluminum and silver mirror are flat as expected. In the reflectivity spectrum of the aluminum mirror we see a trough at 12500 cm^{-1} due to an increased absorption of the aluminum, which is caused by interband electronic transitions [62]. The decrease of 20% agrees with the value presented in [62]. The increased absorption of aluminum near 12500 cm^{-1} results

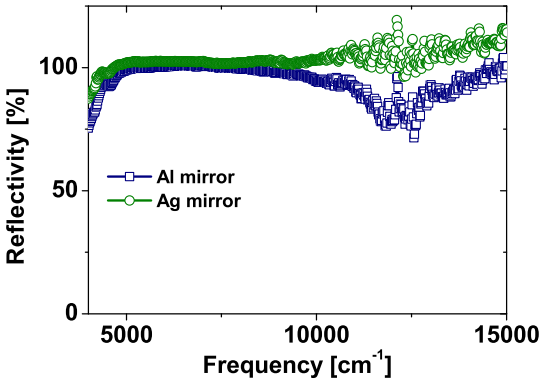

FIGURE 2.4: *Measurements of a silver and an aluminum mirror. The reflectance is normalized with the gold reflectance, yielding the reflectivity spectrum. The reflectivity spectrum of aluminum is flat and 100 %, except for a trough at 12500 cm^{-1} due to an increased absorption of the aluminum caused by interband electronic transitions [62].*

in noise. Since the signal at this frequency is decreased due to the aluminum mirrors used in the optical path, thereby decreasing the signal to noise ratio.

After the mirrors, a photonic crystal sample was measured. The reflectivity spectrum of a woodpile photonic crystal is shown in figure 2.5. A pronounced and broad stopband is present between 5000 cm^{-1} and 8500 cm^{-1}. A pronounced trough is visible at 7800 cm^{-1} (indicated with black arrow) in the stopband for light polarized parallel to the rods in the upper layer of the photonic crystal. The trough in the stopband appears for a polarization parallel to the upper layer of rods and is related to the superstructure of the crystal [24, 63]. In previous measurements on woodpile photonic crystals a strong dependence of the reflectivity spectrum on polarization was found by Molenaar [60]. The previous measurements were done by extensive laser scanning with the switch setup which also requires frequent realignment. Conversely, with our new setup the whole spectrum is quickly acquired. The measurements of Molenaar and the measurement with the new reflectivity setup are shown in figure 2.5. Figure 2.5 shows that the previous measurements are well reproduced with our reflectivity setup without polarizer. The maximum difference we found between the measurements is 12.5%, which is a very good agreement between the two measurements. The reflectivity spectrum from the reflectivity setup agree with the switch setup, since our white light source has one dominant polarization in the spectral

region from 4000 cm^{-1} to 10000 cm^{-1}. The ratio between the polarizations is about 85 %.

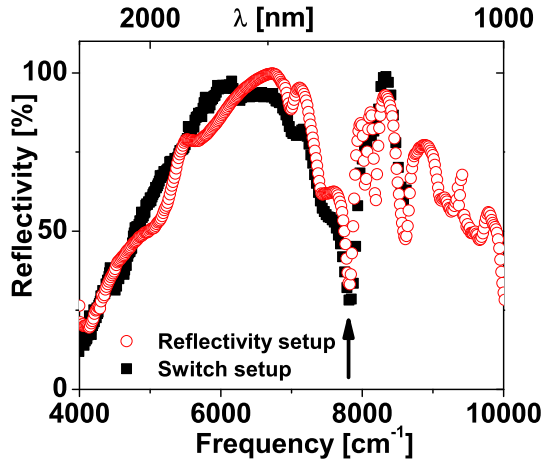

FIGURE 2.5: *Measurements of the stopband of a woodpile photonic crystal by laser scanning with the switching setup (solid squares) [24] and the new reflectivity setup (open circles). The black arrow indicates a trough in the stopband.*

2.3.3 Microscope

A CCD camera is built into the setup in order to align more precisely and to be able to make a map of the surface of the photonic samples under investigation. Figure 2.6 A shows a microscope image of the same 3D inverse woodpile photonic crystal as in figure 2.1. The top side of the picture shows air and the bottom side silicon. At the air-silicon interface a 7 μm thick layer of 2D photonic crystal is present seen as the vertical pores. The black arrow indicates the 3D photonic crystal, which is 5 μm wide. The white arrow indicates the white-light focus, which has dimensions equal to the 3D crystal. Figure 2.6 B shows a picture from a micropillar with a diameter of 20 μm similar to the one shown in figure 2.1 B. The white background is from the gold surface of the sample reflected light. The grey circle is the micropillar. The white dot on top of the micropillar is the focused white-light laser beam that is much smaller than the pillar.

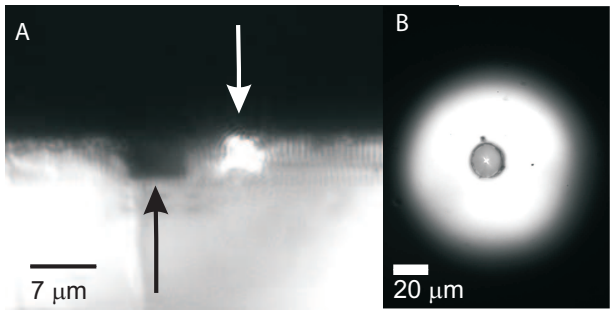

FIGURE 2.6: *Picture a 3D silicon inverse woodpile photonic crystal (A, black arrow) and a micropillar sample (B). The 3D photonic crystal is the same as shown in figure 2.1. The white arrow indicates the white-light focus. The diameter of the micropillar is 20 μm. The white background is the gold surface and the grey circle is the micropillar. The white spot in the middle of the micropillar is the white-light laser beam, whose focus is smaller than the pillar.*

2.3.4 Reflectivity measurements

Optical reflectivity measurements with the new setup are shown in figure 2.7. Figure 2.7

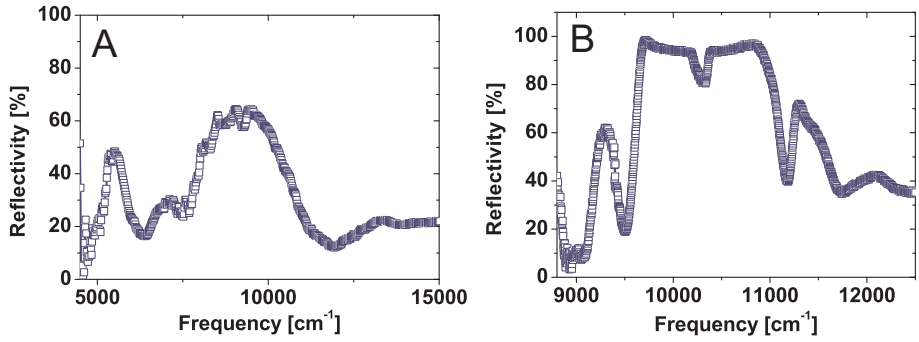

FIGURE 2.7: *Reflectivity spectra of a 2D photonic crystal (A) and of the micropillar shown in figure 2.3 B (B). The spectra were measured with different detectors therefore the frequency scale is different in figure 2.7 A and B.*

A shows the reflectivity spectrum of a 7 μm thick two-dimensional photonic crystal. The spectrum of the two-dimensional photonic crystal shows two reflection peaks. The first peak at 5000 cm^{-1} is due to the $\Gamma - K$-gap while the second peak at 8000 cm^{-1} is due to Bragg reflection (see also chapter 9). Figure 2.7 B shows the spectrum of the micropillar depicted in figure 2.6 B, which has a diameter of 20 μm. The reflectivity spectrum of

the micropillar shows a broad stopband around 9000 cm^{-1}. In the middle of the stopband a trough is present due to the λ-layer that acts as an optical cavity. The measured linewidth of the cavity resonance is broadened due to the high NA of the objective. The homogeneous linewidth is in the order of 0.05 %, corresponding to a Q of 2000.

2.4 Ultrafast switch setup

2.4.1 Pump and probe beams

Figure 2.8 shows a schematic representation of our ultrafast switching setup. It has been extensively described before [24, 59, 64], therefore we provide a short overview. The setup consists of a regeneratively amplified Ti:Sapphire laser (Spectra Physics Hurricane), which drives two independently tunable optical parametric amplifiers (OPAs, Topas) with a repetition rate of $\Omega_{\text{rep}} = 1$ kHz. The frequencies of both OPAs are computer controlled and have a continuously tunable output frequency between 0.44 and 2.4 eV. The pulse duration is $\tau_P = 120 \pm 10$ fs (measured at $E_{\text{Pump}} = 0.95$ eV) [(2)], and the spectral width $\Delta E/E_0 = 1.33\%$ [(3)], so the pulses are nearly transform limited (transform limited pulses would have a duration of $\tau_P = 110$ fs). The delay stage is computer controlled and can introduce a path difference of 40 cm to the probe, corresponding to a time delay of 1.3 ns, much longer than typical recombination times in III-V semiconductor or polysilicon structures that we studied. The resolution is 10 fs, and thus much higher than the pulse durations. The pump is focussed onto the sample under an angle of $\theta = 15°$ by an achromatic lens of NA = 0.01.

The peak intensity for a focussed Gaussian pulse is given by

$$I_{\text{pump}} = \frac{4\sqrt{\ln 2}G}{\pi^{\frac{3}{2}} r^2 \tau_P}, \tag{2.1}$$

where r is the waist radius at the focus and G the energy of the pulse. Because r depends on the pump frequency E_{pump}, it is important to take into account the variation in intensity in experiments where the pump frequency is scanned. The diameters were obtained by measuring the reflected intensity of the pump beam as a sharp-edged Si wafer is scanned

[(2)] τ_P denotes the FWHM of the pulse intensity, see e.g. [55], and was measured using an intensity autocorrelator, see also chapter 3.
[(3)] Measured with an OceanOptics USB2000 spectrometer.

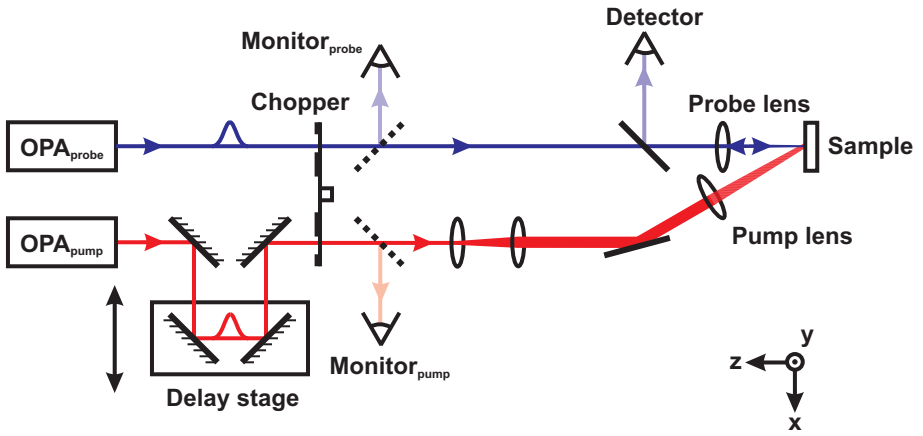

FIGURE 2.8: *Schematic drawing of the setup. The pump and probe OPA's (TOPAS) are driven by a Hurricane (not shown) emitting 120 fs pulses. The pump pulses are delayed via a delay stage. After the pulses pass through a chopper, both probe and the pump pulses are separately monitored by diodes. The pulses are focussed onto the sample via achromatic lenses, and the intensities of the reflected probe pulses are measured via an InGaAs diode detector. The intensity of each monitored and reflected pulse is sampled and held by a boxcar averager, which offers the integrated intensity to a PC, that stores every single pulse for later evaluation. In the frequency resolved setup, we replaced the diode detector with a spectrometer.*

through the focus. The reflected intensity is the integral of the light distribution in the focus, and is an error function for a Gaussian beam. We therefore fitted the derivative of the measured intensity to a Gaussian, from which the widths are readily obtained. The resulting diameters are compared to the diffraction limited diameter under an angle of $\theta = 15°$ and excellent agreement is obtained.

The probe beam is normally incident ($\theta = 0°$) onto the sample, and is focused to a Gaussian spot of 32 μm FWHM (at $E_{\text{probe}} = 1.24$ eV) at a small angular divergence NA = 0.02. Because of the smaller probe focus with respect to that of the pump, only the flat part of the pump focus is probed, resulting in good lateral homogeneity. The reflectivity was calibrated by referencing to a gold mirror. To avoid carrier generation by the probe, we verified during all experiments that the probe pulses on the sample were ten times less intense than the pump pulses.

2.4.2 Broadband detection

We have performed two sets of switching experiments that differ through their detection schemes. In the first broadband scheme, we measured both the reflected probe as well as the pump and probe intensity monitors with InGaAs diode detectors. To reduce the possible noise caused by the low probe powers, and the possible background caused by the pump, a versatile measurement scheme was developed to subtract the pump background from the probe signal, and to compensate for possible pulse-to-pulse variations in the output of our laser [47, 64].

We measured both the reflected probe as well as the pump and probe intensity monitors with InGaAs diode detectors. A boxcar averager, synchronized to the pulse trigger, integrates and holds the detected signal before being read out by a digital to analogue converter (DAC). The signal J offered to the DAC card by the boxcar, neglecting electronic amplification factors, is equal to the magnitude of the time- and space integrated Poynting vector $\mathbf{S}$,

$$J = \pi R^2 \int_{-t_{\text{int}}/2}^{t_{\text{int}}/2} |\mathbf{S}| dt = \int_{-t_{\text{int}}/2}^{t_{\text{int}}/2} \sqrt{\frac{\epsilon_0}{\mu_0}} F(t)^2 dt \tag{2.2}$$

$$\approx \pi R^2 \sqrt{\frac{\epsilon_0}{\mu_0}} \frac{\tilde{F}_0^2}{2} \int_{-\infty}^{\infty} \left(\exp(-4 \ln 2 t^2/\tau_G^2)\right)^2 dt \tag{2.3}$$

$$= \pi R^2 \sqrt{\frac{\epsilon_0}{\mu_0}} \sqrt{\frac{\pi}{2\ln(2)}} \frac{\tau_P \tilde{F}_0^2}{4}, \tag{2.4}$$

where the electric field $F(t)$ reflected by a perfect mirror onto the detector can be separated in a Gaussian envelope $\tilde{F}(t)$ of FWHM τ_G and amplitude $\tilde{F}_0$ multiplied by an sinusoidal component with a carrier frequency ω_0 in rad/s [(4)]. The beam is collimated and has radius R. ϵ_0 and μ_0 denote the permittivity and permeability of free space, respectively. The squared oscillating term can then be integrated separately and yields $1/2$, and the time integration can be taken to infinity because $t_{\text{int}} >> \tau_P$. Since the integration time of the boxcar ($t_{\text{int}} \sim 150$ ns) is much longer than any probe interaction time [(5)], we essentially integrate all probe light that is stored or reflected by the cavity, given a set pump-probe

[(4)] This Slowly Varying Envelope Approximation (SVEA, see e.g. [55]) can be applied to pulses where $\tau_P >> 1/\omega_0$, and where ω_0 does not change over t, i.e., for bandwidth limited pulses. For pulses whose envelope is broadened by interaction with a cavity, the analytic expression obtained (Eq. 2.4) is not valid, but the approximation of the integration limits does not change.

[(5)] The probe interaction time is either τ_P or Q/ω_0, whichever is greater, and is in the 100 fs to 1 ps range.

time delay $\Delta\tau$. We note that it is not the instantaneous transmission or reflection that is measured, but the integrated intensity. Therefore we call the measured signal, transient reflectivity or transient transmission.

2.4.3 Frequency-resolved detection

In a second set of experiments, we used the large probe bandwidth to resolve spectral features with a high-resolution spectrometer. These narrow spectral features occurred in the microcavity samples discussed in chapter 4 and chapter 6. We accomplish this with a spectrograph (PI/Acton SP-2558), using a 1024 channel InGaAs detector (OMA-V), yielding a resolution of 0.12 meV at 1.24 eV [65]. The diode array is kept at a temperature of 100 K to reduce dark counts, measured to be 350 adu/(s pixel), only 1 % of the counts detected from probe pulses of several nJ. The transient reflectivity was determined by referencing the transient reflectance spectra to a gold spectrum at the end of the scan. Even though the effective repetition period ($\Omega_{\mathrm{rep}}/2 = 1/500$ Hz) of the laser is equal to the minimum exposure time of the detector electronics (2 ms), the OMA-V was operated in free running mode, with an integration time set to 1s, as no additional useful information was expected in single shot measurements. The measured spectra thus consist of 1s·500Hz = 500 pulses. The observed spectrum, again without amplification and conversion factors, is a Fourier Transform of $F(t)$:

$$J(\omega) = \pi R^2 (\epsilon_0 c)^{-1} \left| \int_{-\infty}^{\infty} dt F(t) e^{i\omega t} \right|^2 , \tag{2.5}$$

where c is the velocity of light in free space. A field leaking from a cavity whose resonance shifts in time might have frequency components whose amplitude is higher than that of a bandwidth limited pulse reflected off a gold mirror. In that case, the ratio of the reflected pulse to a reference pulse, the transient reflectivity, $J(\omega)_{\mathrm{sample}}/J(\omega)_{\mathrm{ref}}$ may exceed unity for some E_{Probe}.

CHAPTER 3

True quality factor of an ultrafast microcavity

3.1 Introduction

Since light is extremely elusive there is a great interest to store photons in a small volume for a certain time. Storage of photons in an applicable way can be achieved using solid state cavities. Tanabe *et al.* used cavities to create large pulse delays with small group velocities by storing light in a cavity inside a 2D photonic crystal slab [66, 67]. Another application where storage of light in a cavity plays a crucial role is changing the color of light as was studied by Preble *et al.* [2]. Ultimately, with a microcavity the strong coupling regime of cavity quantum electrodynamics can be entered [3, 4]. In the strong coupling regime a cavity and a two level system together form a new set of states. Normal-mode splitting of a coupled exciton-photon mode was observed in a planar microcavity [68]. Other interesting experiments have been performed on planar cavities, e.g, Bose-Einstein condensation of exciton polaritons [69] and the investigation of the limitations of a scanning Fabry-Pérot interferometer [70].

An important characteristic parameter of a cavity resonance is the storage time of light τ_{cav}. The storage time is defined by the response of the cavity resonance to a Dirac pulse. Excitation of the electromagnetic field in a cavity was studied in [71]. The response to the Dirac pulse is given by an exponential decay of the intensity *I(t)* in the cavity resonance [8]:

$$I(t) = I_0 e^{-t/\tau_{cav}}, \tag{3.1}$$

with I_0 the initial intensity that the pulse stores in the cavity. However, in more complex cavities the behavior of the cavity can be very different from the single exponential case [9]. To compare cavities independent of their resonance frequencies ω_0, the widely used figure of merit is the resonance quality factor Q, which is defined as:

$$Q \equiv \tau_{cav}\omega_0. \tag{3.2}$$

Physically, the quality factor is proportional to the ratio between the total energy stored and the energy lost per cycle. At optical frequencies a cavity with a feasible high quality factor of $Q = 10^6$ is relatively slow with a response time in the order of nanoseconds. A cavity with a moderate quality factor $Q = 1000$, however, is fast with a response time of picoseconds. The picosecond timescale allows ultrafast access and storage of light in the cavities.

A common procedure to estimate the quality factor of a cavity is to measure a transmission or reflectivity spectrum and extract Q from the relative linewidth of the cavity resonance [2–4, 10–13]. For a single resonance without dephasing, one can use the Wiener-Khintchine theorem, which relates the field autocorrelate to the intensity spectrum, to obtain

$$Q = \frac{\omega_0}{\Delta\omega}. \tag{3.3}$$

However, if there is significant dephasing, e.g. due to inhomogeneous broadening or thermal noise, $\Delta\omega$ will in general be larger and $Q > \omega_0/\Delta\omega$.

From many resonating systems in condensed matter and solid state physics, it is known that besides homogeneous broadening there is also the possibility of inhomogeneous broadening of a resonance [6, 14]. In the case of an ensemble of resonators inhomogeneous broadening of a resonance results from inhomogeneities in the resonance frequency. If the resonance frequency is different for each resonator the linewidth of the ensemble is broader than the linewidth of a single resonator and the ensemble linewidth is typically determined by the distribution of resonance frequencies. In the case of inhomogeneous broadening the linewidth will only give a lower boundary for the range of possible Q values. The true quality factor must in this case be determined from dynamic measurements.

A dynamic measurement to determine the quality factor is a cavity ring down experiment as was treated in [72]. In this case a cavity is excited by a pulse and the intensity

emitted from the cavity is measured as a function of time. In the case of storage times in the order of nanoseconds and very high quality factors ($Q = 10^6$) time correlated single photon counting can be used to determine the storage time [66]. In our case of ultrafast cavities that decay on a ps timescale with moderate quality factor ($Q = 1000$), an intensity autocorrelation function is the method of choice for determining the quality factor.

We measure a normalized intensity autocorrelation function G_2, following [55]

$$G_2(\tau) = \frac{< I(t)I(t-\tau) >}{I_0^2}, \tag{3.4}$$

where τ is the delay time between the pulses from each of the interferometer branches, I_0^2 is equal to maximum value of the unnormalized autocorrelation value, and $I(t)$ is the time dependent intensity. There is no phase in Eq. 3.4, which means that this is the proper autocorrelation function, also in case of dephasing. The autocorrelate has its maximum at delay $\tau = 0$, when the pulses in the two branches of the Michelson interferometer overlap. For example the autocorrelate of a Gaussian pulse is given by a Gaussian shape, where the width of the input pulse τ_{ip} and the autocorrelate are related as $\tau_{ac} = \sqrt{2}\tau_{ip}$. From the autocorrelate of a pulse stored in the cavity resonance, the storage time can be found from the full width at half maximum τ_{FWHM} of G_2, with $\tau_{cav} = 0.63\tau_{FWHM}$.

3.2 Experimental

For pulse transmission and the intensity autocorrelate, we used a Titanium Sapphire laser that emits $\tau_{ip} = 0.115$ ps pulses at $\lambda = 800$ nm at a repetition rate of 1 kHz (Hurricane, Spectra Physics). The laser drives an optical parametric amplifier (OPA, Topas 800-fs, Light Conversion), which generates the pulses used to probe the photonic cavity. The center wavelength of the OPA pulses can be tuned between 450 nm and 2400 nm. We used a fiber optic spectrometer (USB2000, Ocean Optics) to measure transmission spectra of the femtosecond pulses. We measured with an unfocused collimated beam with a spot diameter of 2 mm, and a numerical aperture NA = 10^{-4}. The intensity autocorrelation function was measured using a Pulse Check autocorrelator (APE GmbH). The autocorrelator consists of a Michelson interferometer with a scanned delay path and a nonlinear crystal that generates second harmonic light. The autocorrelator has a maximum range of 15 ps with a resolution of 1 fs. We used the same beam parameters as in transmission.

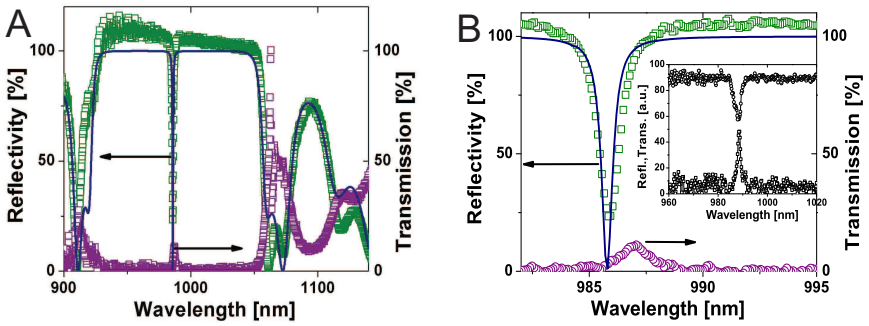

FIGURE 3.1: *(A) Linear reflectivity and transmission spectrum of the GaAs/AlAs microcavity. The solid line represents the fit with a Transfer Matrix (TM) model. A stopband is apparent in both reflection and transmission; the trough in the reflectivity spectrum and the peak in the transmission spectrum reveal the presence of the cavity. (B) Zoom-in of (A). From the linewidth of the trough and peak, an inverse relative linewidth of 830 was found in reflection and transmission. The resonance is slightly shifted between the transmission and reflection measurement due to realignment of the sample between the measurements. The inset in B shows a reflection and a transmission spectrum, measured at the same position. Here the trough and peak are clearly at the same wavelength.*

The intensity on the sample is 100 $kWcm^{-2}$, sufficiently low to avoid nonlinear effects.

Simulations were performed with the finite-difference time-domain (FDTD) method using a freely available software package with subpixel smoothing for increased accuracy [23].

3.3 Experimental results

In figure 3.1 A we show the reflection and transmission spectra of the 980 nm planar cavity. A prominent stopband with a reflection of 100 % and a transmission of 0 % is visible. Outside the stopband a Fabry-Pérot fringe pattern is visible, while inside the stopband a narrow trough in reflection and a narrow peak in transmission mark the position of the cavity resonance. An effect of the spatial gradient in the cavity thickness is visible in the spectra in figure 3.1 B: The frequencies of the peak and trough, which are measured at different sample position, differ slightly. Reflectivity and transmission measurements on the same spot are shown as an inset in figure 3.1 B. The trough and the peak are clearly at the same wavelength as expected.

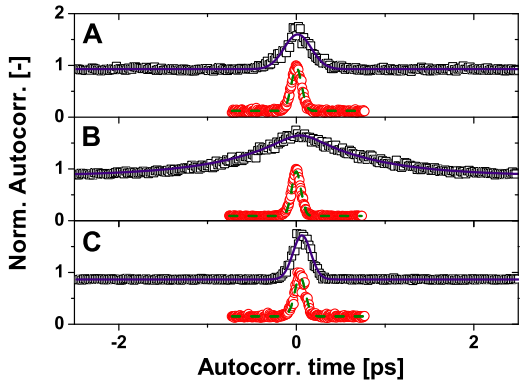

FIGURE 3.2: *Normalized intensity autocorrelation traces of pulses transmitted through a planar cavity at different OPA wavelength settings: 930 nm (A), 985 nm (B) and 1070 nm (C). The autocorrelation traces of the input pulses are given by the circles, while the autocorrelation traces of pulses transmitted through the cavity are offset by 0.9 and given by squares. The dashed and solid lines are fits to the autocorrelation traces, without and with sample, respectively. The shape of the autocorrelation trace is Gaussian for the pulses from the OPA. The pulses that are on resonance with the cavity show an autocorrelate that agrees very well with the autocorrelation trace from the damped oscillator model (B). The shape of the pulses transmitted through a non-photonic range of the sample remains Gaussian.*

The solid line in figures 3.1 A and 3.1 B represents a transfer matrix (TM) calculation, with fixed complex input parameters n_{GaAs} [73] and n_{AlAs} [74]. The thickness of the $\lambda/4$ layers (d_{GaAs} = 70.2 nm and d_{AlAs} = 83.2 nm) and the thickness of the cavity (d_{cav} = 277 nm) were obtained by fitting the results of the calculations to the measured spectrum. These values are in agreement with expected values from the fabrication process. The calculation fits well with respect to frequency and amplitude. The reflectivity of the measured stopband is higher than the calculated value of 100 % because of a small systematic error in the gold reference spectrum.

It is apparent from figure 3.1 B that the calculated linewidth of the cavity resonance is narrower than the measured linewidth. We attribute this discrepancy to inhomogeneous broadening of the measured linewidth, due to the spatial gradient in the cavity layer thickness. With the 100 μm diameter spot we average over different positions and therefore over different resonance frequencies. Broadening due to a spread in wavevectors can be neglected since the numerical aperture of the impinging beam was made very small

($NA < 0.05$), as opposed to [13], where a high NA was used. We find that the relative linewidth in both reflection and transmission equals $\frac{\lambda_0}{\Delta\lambda} = 830$, with $\Delta\lambda$ the full width at half maximum (FWHM) and λ_0 the resonance wavelength. The transfer matrix calculation yields an inverse relative linewidth of 1640 ± 100, about double the value of the inverse linewidth measured with white-light spectroscopy.

We measured the intensity autocorrelation traces to determine the true storage time and Q of the cavity resonance with a time-resolved measurement. Figure 3.2 shows the autocorrelation traces at values of the center wavelength of the OPA, $\lambda_{OPA} = 930$ nm (A), $\lambda_{OPA} = 985$ nm (B) and $\lambda_{OPA} = 1070$ nm (C). All figures show that the pulses that are transmitted through the sample are broader than the input pulses. The width of the input pulses is $\tau_{ip} = 0.115$ ps and the shape Gaussian, which we expect from the specifications of our laser system. The transmitted pulses are broadened by dispersion in the off resonance cases (A) and (C). In the case of figure 3.2 B the broadening is the result of the storage of the photons in the cavity.

The shape of the autocorrelation trace of the transmitted pulses is Gaussian for pulses transmitted outside the stopband, as expected. The autocorrelation traces measured on resonance with the cavity (B) are non-Gaussian. This is typical for autocorrelation traces near the cavity resonance, because of the exponential decay of the energy stored in the cavity. The autocorrelation traces calculated with a damped oscillator model is shown in figure (B) and fits the experimental data very well. From the width of the autocorrelation trace on resonance ($\tau_{FWHM} = 1.1$ ps), we conclude that the true storage time of our cavity is $\tau_{cav} = 0.78 \pm 0.05$ ps.

To further analyze the autocorrelation traces we plot the full width at half maximum of the measured autocorrelation traces. The results are shown in figure 3.3 A as a function of center wavelength of the laser. The width of the autocorrelate of pulses without the sample is $\tau_{ac} = 0.115 \times \sqrt{2}$ ps and essentially independent of laser wavelength, as expected from the OPA specifications. In the presence of the sample, we observe a more complex dependency on the wavelength, with three regimes: Transmission on resonance, transmission outside the stopband, transmission inside the stopband. Near the cavity resonance the width of the autocorrelate increases drastically to $\tau_{FWHM} = 1.1$ ps. The width of the autocorrelate at the cavity resonance is attributed to the storage of light in the cavity: The storage time of the cavity $\tau_{cav} = 0.78 \pm 0.05$ ps and the quality factor is equal to 1500 ± 100.

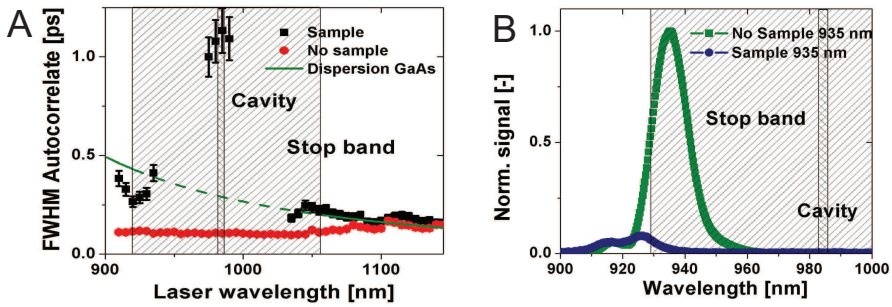

FIGURE 3.3: *(A) Pulse width as a function of wavelength setting. The pulses that passed through the sample (squares) are broadened with respect to the input pulses (circles). The solid/dashed line represents the FWHM of a 15 nm spectrally wide input pulse that is transmitted through a 350 μm GaAs wafer that is used as a substrate. (B) Normalized spectrum transmitted through the microcavity, and reference spectra of pulses directly from the OPA. For 935 nm wavelength setting (solid squares) the transmitted spectrum consists of the tail of the input spectrum that continues in the region on the blue side of the stopband (solid circles).*

Outside the stopband the pulses are broadened. The width of the autocorrelate outside the stopband is about $0.2\times\sqrt{2}$ ps. We attribute the broadening outside the stopband region to dispersion in the GaAs substrate. From figure 3.3 A it can be seen that the width of the autocorrelation traces matches well the expected width for a pulse transmitted through a GaAs wafer [75]. The expected width is calculated for a GaAs wafer with a thickness of 350 μm, from the dispersion given by Blakemore [73].

In figure 3.3 A, we observe datapoints inside the stopband, where a transmission of 0 % is expected. We measure values for the width that are close to the values outside the stopband. The situation in this case is sketched in figure 3.3 B where we see the transmitted spectrum with and without sample. We observe that the blue part of the spectrum is transmitted, which means that the measured width of the intensity autocorrelate is the value corresponding to the blue side of the stopband and not a value for outside the stopband.

3.4 Modeling

To obtain a physical picture of the decay mechanism inside the cavity and to verify what the true Q is, we model the behavior with a damped harmonic oscillator. We furthermore

performed FDTD calculations to calculate the Q of the cavity in the ideal case and to check the validity of the harmonic oscillator model [1].

The response of a damped harmonic oscillator with $Q = 1450$ to a Gaussian input pulse with a width of $\tau_{ip} = 0.2$ ps is shown in figure 3.4, together with the Gaussian input pulse and the cavity response as calculated with FDTD. No dispersion and no absorption was taken into account for the FDTD calculations. In the harmonic oscillator case and in the FDTD case the intensity decays exponentially and with the same rate. Therefore, we conclude that the harmonic oscillator is a suitable model to describe in a simple way the decay of the microcavity. Furthermore the quality factor of the cavity without absorption and dispersion is equal to $Q = 1450 \pm 100$.

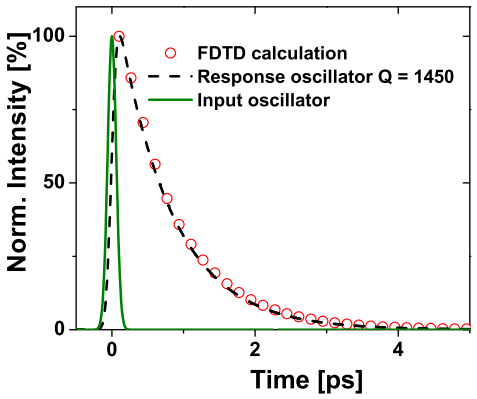

FIGURE 3.4: *Response of a damped harmonic oscillator with a quality factor Q = 1450 (dashed) to a Gaussian input pulse (solid). The output pulse is the input pulse convoluted with the impulse response of the oscillator. The symbols represent the resulting decay of the intensity in the cavity, as obtained from the FDTD calculation.*

With the damped harmonic oscillator model we have calculated the autocorrelates that are shown together with the measured data in figure 3.5 for a quality factor of the damped harmonic oscillator $Q = 1500$ and Gaussian input pulse with width 0.12 ps. Figure 3.5 shows a very good agreement between the measured autocorrelation trace and the calcu-

[1] We used $e^{-t\omega_0/Q}$ as the impulse response of intensity in the cavity.

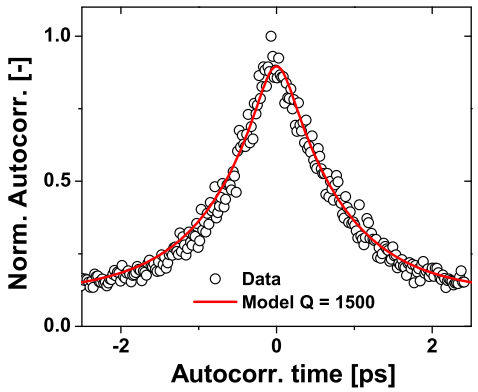

FIGURE 3.5: *Autocorrelate of pulse transmitted at the cavity resonance (circles). The solid line represents the result from a simple oscillator model with Q = 1500. The input pulse duration is 0.12 ps.*

lated autocorrelation trace for $Q = 1500$. The autocorrelate obtained from this model has a FWHM of 1.2 ps, which is in very good agreement with the measured value of 1.1 ps.

Table 3.1 presents the results of the various methods to determine the quality factor presented in this chapter. We see that the value for the inverse linewidth found from the transfer matrix model agrees well with the value found from the autocorrelator measurement. The slight discrepancy might be attributed to minor irregularities in the structure. We conclude that the quality factor of the cavity is 1500 ± 100 and the storage time of light 0.78 ± 0.05 ps. The inverse linewidth measured in reflection and transmission with white light spectroscopy is much smaller than the value from autocorrelator measurements. The difference results from inhomogeneous broadening due to the spatial gradient in the thickness of the cavity layer. For a quality factor of 1500 we expect a width of 0.64 nm, while we measure a width of 1.2 ± 0.1 nm. Because of the focus diameter of 100 μm and the spatial gradient of 5.64 nm/mm, we expect a broadening of 0.56 nm. We find a total width of 1.2 ± 0.1 nm if we add the broadening to the unbroadened width. The total width of 1.2 ± 0.1 nm is in perfect agreement with the measured value of 1.2 ± 0.1 nm. The FDTD calculation agrees very well with the measured value and the value obtained from the transfer matrix calculation. No absorption is taken into account in the FDTD calculation, which is the case for the TM model.

TABLE 3.1: Overview of inverse linewidths and cavity lifetimes measured and calculated with presented methods.

	Method	$\frac{\lambda_0}{\Delta\lambda}$	τ_{cav} (ps)
Measurement	Autocorrelator	1500 ±100	0.78±0.05
	Refl./Trans.	830 ±50	0.43 ±0.02
Theory	Transfer Matrix	1640 ±100	0.93±0.05
	FDTD	1450 ±100	0.75 ±0.05

The inverse relative linewidth of 830 that we find from the transmission and reflectivity measurements is the result of inhomogeneous broadening of the resonance. The origin of this inhomogeneous broadening is most likely the spatial gradient in the λ-thick GaAs layer. Because there is inhomogeneous broadening, the planar microcavity should be viewed as a static ensemble of microcavities of which each resonance frequency is slightly shifted [6]. This is in agreement with the results presented in [76], where the spatial extent of modes was investigated. The effective radius of the mode is given by $r_{eff}^2 = (Q/2\pi)(\lambda/n)^2$. In our case we find a spatial extent in the order of 5 μm, which is much smaller than the diameter of the probe beam. In general our results show that the true quality factor of a planar microcavity indeed can only be obtained from a time-resolved measurement.

3.5 Conclusion

In the case of an inhomogeneously broadened resonance we have shown that the intensity autocorrelate can be used to determine the storage time of a cavity resonance. For an inhomogeneously broadened microcavity resonance we have measured both the spectral width and the intensity autocorrelation trace. The intensity autocorrelation trace yields a value of the quality factor that agrees well with the values found from transfer matrix and FDTD calculations. The spectral width is affected by inhomogeneous broadening and leads to the wrong value for the quality factor.

CHAPTER 4

Three photon free carrier switching of GaAs/AlAs microcavity

4.1 Introduction

Recently, there has been a growing interest in switching cavities on ultrafast timescales. Switching cavities is important for dynamic control of light, such as optical wavelength modulation, bandwidth conversion, density of states switching, and trapping and releasing photons [43, 77–80]. Cavity switching becomes especially interesting when the photon storage time τ_{cav} is in the order of the timescales within which the cavity resonance changes [81]. In this regime, strong pulse chirping has been observed [82]. Furthermore, frequency conversion was observed when a resonator was switched at a femtosecond timescale [2].

Because of technical progress, the availability of strong, short optical pulses, the good reproducibility of the cavities, and the possibility of integration in all-optical networks has furthered the popularity of free-carrier switching of resonators or cavities, see, e.g., Refs. [13, 78, 83]. In this switching scheme, the carriers result in a change of both real (n') and imaginary (n'') part of the refractive index that is proportional to the induced carrier density N. The carriers recombine within a typical timescale ranging from ps to ns. The change of the refractive index leads to a change in the optical properties of the cavities. For example, the resonance frequency of the cavity changes. When the carriers recombine the cavity resonance relaxes to its unswitched value, with a relaxation time τ_{rec}. Surprisingly, the relaxation and broadening mechanisms have hardly been discussed,

mostly due to the lack of frequency- and time-resolved data. In general, studies are limited to either the reflectivity at two frequencies [78, 84–87] or to the reflectivity at two probe delays [88].

We present here a systematic study at frequencies covering the whole cavity resonance, and pump-probe delays covering the carrier recombination at three pump wavelengths, which allows us to investigate the dynamics of resonance and lineshape. We work in the three-photon absorption regime, because we want to explore the pump wavelength regime in which absorption is minimized and instantaneous switching using the electronic Kerr effect can be achieved at pump-probe coincidence [50, 89]. Previous experiments were performed in the two-photon regime [13]. We study both the dynamic shifting and broadening of a cavity resonance by performing time- and frequency-resolved pump-probe spectroscopy on planar GaAs/AlAs microcavities, with a frequency resolution being much higher than the dynamic cavity linewidth. We compare our results with a model based on transfer matrix calculations. We show that it is possible to decrease τ_{rec} by tuning the fabrication parameters of the sample.

4.2 Transfer matrix model

In this work we compare the experimental results to a transfer matrix calculation which included the dispersion of GaAs [73] and AlAs [74] and the Drude model [24]. The thickness of the GaAs (d_{GaAs} = 69.2 nm) and AlAs (d_{AlAs} = 81.0) layers are verified with a linear reflectivity measurement as is shown in figure 4.1. The recombination time and the initial free carrier density are the free parameters in the calculation. For each time delay $\Delta\tau$ the new free carrier density is calculated, which is the input for the Drude model that yields the refractive index as a function of frequency. The frequency dependent refractive index is the input parameter for the transfer matrix calculation that yields the spectrum at each time delay. From this spectrum the resonance position and linewidth are derived.

4.3 Results

4.3.1 Linear reflectivity and transmission

Figure 4.1 shows the measured linear reflectivity and linear transmission spectra of our 980 nm sample, together with a transfer matrix (TM) calculation. Both spectra show a

stopband with a cavity resonance and Fabry-Pérot fringes. In the reflectivity spectrum the cavity resonance reveals itself as a trough in the stopband, while a complementary peak arises in transmission. The relative linewidth of the cavity resonance derived from figure 4.1 is 0.12%, which is the inhomogeneous broadened width [59].

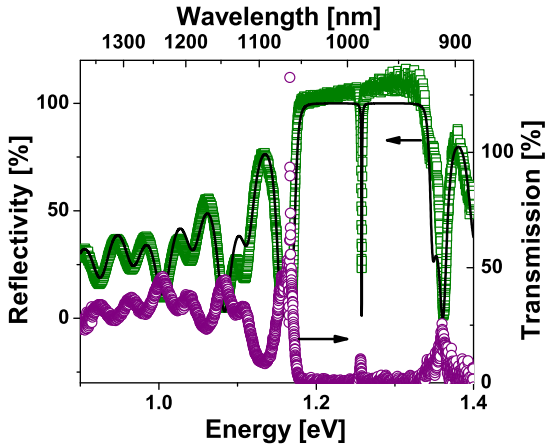

FIGURE 4.1: *Linear reflectivity (squares) and transmission (circles) spectrum. The reflectivity spectrum shows a broad stopband in which a trough due to the cavity resonance is present. The transmission spectrum shows a peak at the resonance frequency and no transmission in the rest of the stopband. The solid line represents a transfer matrix (TM) calculation of the reflectivity of the complete stack.*

The transfer matrix calculation reproduces the experimental resonance, stopband, and Fabry- Pérot fringes very well. The only free parameters in the model were the thicknesses of the GaAs (d_{GaAs} = 69.2 nm) and AlAs (d_{AlAs} = 81.0 nm). These values are in agreement with expected values from the fabrication process. The values differ from the ones found in chapter chap:ChPulseTCavity, due to a spatial gradient in the sample thickness, induced by the fabrication process.

4.3.2 Ultrafast switched transient reflectivity and transient transmission

Ultrafast transient reflectivity and transient transmission spectra of the sample pumped at 2000 nm, are shown in figure 4.2 A-D. The transient reflectivity spectra (figures 4.2 A and 4.2 B) show that the cavity resonance frequency depends on the delay between the pump and probe pulses. If the probe pulse arrives before the pump pulse (e.g. $\Delta\tau$ = -20 ps as shown in figure 4.2 A and figure 4.2 C), the cavity resonance is undisturbed and lies at 1.259 eV.

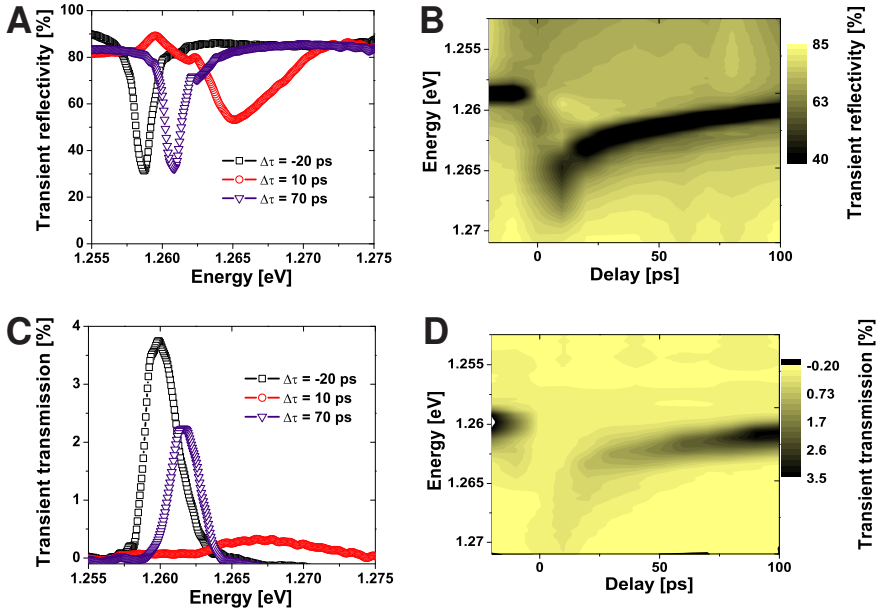

FIGURE 4.2: *Measured switched transient reflectivity (A,B) and switched transient transmission (C,D) as a function of time delay. The pump wavelength is 2000 nm and the pump intensities are 135 $GWcm^{-2}$ (A,B) and 90 $GWcm^{-2}$ (C,D). The data in figure A and C are cross sections as the data presented in figure B and D, respectively. At positive delay, the resonance shifts with respect to the resonance at negative delay, both in transmission and reflection. The observed blue shift is characteristic for free carrier generation.*

At coincidence of pump and probe pulse, the cavity resonance becomes less pronounced due to non-degenerate two-photon absorption. At positive delay, the resonance frequency changes due to free carriers that are excited in a three-photon absorption process by the pump pulse. The free carriers decrease the refractive index of the GaAs and thereby decrease the resonance frequency of the cavity. The maximum shift of the resonance frequency occurs at 10 ps when the frequency of the trough is at 1.265 eV. Furthermore, the minimum in reflectivity increases from 30 % to 50 %, when the resonance is shifted.

At 10 ps delay we do not only observe a shift of the resonance. After 10 ps delay, the excited free carriers start to recombine and thus the cavity resonance starts to shift back (4.2 B), yet it does not fully recover after 100 ps delay. Besides a shift of the resonance frequency, we also observe a broadening of the resonance. In the course of the recombination process, the width of the cavity recovers to its original value.

We see an enhancement of the reflection at the red side of the cavity for 10 ps and 20 ps delay. This enhancement is due to wavelength conversion by the shift of the cavity resonance. Because the cavity resonance shifts, the phase of light stored in the cavity shifts. The induced phase shift introduces new frequencies in the spectrum that appear on the red side of the cavity resonance. This is in agreement with the measurements presented in [59], see chapter 6.

Figure 4.2 C and 4.2 D show for a similar experimental situation the transient transmission. The resonance frequency of the unswitched cavity is 1.26 eV. This slightly differs from the resonance frequency in transient reflectivity because the spectra were measured at a different spot. At $\Delta\tau$ = -10 ps the transient transmission decreases and at pump and probe coincidence ($\Delta\tau = 0ps$) the resonance disappears due to non-degenerate two-photon absorption. The discrepancy between the transient reflectivity measurement and the transient transmission measurement is remarkable, since in the transient reflectivity case the resonance is clearly visible, while in transmission it almost disappears. We attribute this difference to induced absorption in the GaAs layers and in the GaAs substrate. For positive delay the resonance frequency shifts to 1.268 eV and the resonance broadens. After 10 ps, the free carriers start to recombine again. Therefore, the cavity resonance shifts back to its original resonance frequency and recovers its initial linewidth.

4.3.3 Double exponential decay

We will now quantitatively describe the relaxation of the cavity resonance, see also [89]. To a first order approximation, the change in dynamic cavity resonance is a linear function of the refractive index in the GaAs mirrors n_{gm} and in the GaAs λ-slab n_{gc}, which are weighted by field distribution coefficients a and b, respectively. If the field distribution does not change significantly during the switch, we can write for the shift in cavity resonance:

$$\Delta E_{cav}(\Delta t) = a\Delta n'_{gm}(\Delta t) + b\Delta n'_{gc}(\Delta t). \tag{4.1}$$

Since the induced change in refractive index is proportional to the carrier density N_0 for sufficiently small N_0, Eq. 4.1 can be written as

$$\Delta E_{cav}(\Delta t) = a' N_{gm}(\Delta t) + c' N_{gc}(\Delta t), \tag{4.2}$$

where $a' = \frac{a'' e^2}{2m_e^* n_g \epsilon_0 \omega_{pr}^2}$, where a'' is a field distribution weighting factor, m_e^* the effective electron-hole mass in GaAs, n_g the static refractive index of GaAs, ϵ_0 the vacuum permittivity, and ω_{pr}^2 the probe frequency in rad/s. Often, the time evolution of $N_{gm}(t)$ and $N_{gc}(t)$ are considered to be equal. Due to the *different* thicknesses, however, they are governed by *different* relaxation constants τ_1 and τ_2. Therefore, the change in cavity resonance can be written as

$$\Delta E_{cav}(\Delta t) = a' N_0 exp(-\Delta t/\tau_1) + c' N_0 exp(-\Delta t/\tau_2), \tag{4.3}$$

where N_0 is the initial carrier density in the both GaAs mirrors and in the cavity at $\Delta t = \tau_{on}$. In the present experiment, non-radiative recombination of free carriers at GaAs/GaAlAs interfaces is expected to be the dominant recombination process [90]. The behavior of the resonance is thus expected to be double exponential, and indicative of different recombination rates in the GaAs mirrors and in the λ-slab, due to the different thicknesses. The recombination rate in the mirrors is higher compared to the recombination rate in the λ-cavity because of the layers are thinner.

We emphasize that these two different recombination rates can significantly change the analysis of the dynamic field behavior in the cavity: even though an effective single exponential decay time can be orders of magnitude above the cavity dwell time, the composite shorter recombination times will give rise to significantly different field dynamics [81, 82]. To gain access to timescales comparable to τ_{cav}, several groups made use of the fast upswitch time τ_{on} = 1 ps [2, 81]. Here, we probe for the first time during the relax-

ation, whose timescale is controllable, and still comparable to τ_{cav}. The recombination rates in microcavities may further be increased controllably by growing samples with a larger number of recombination centers at the GaAs/AlAs interfaces [91]. Finally, we note that because the field of a photonic crystal cavity at resonance always extends somewhat into the surrounding photonic crystal lattice, our observation of the double-exponential decay is expected to apply also to other types of photonic crystal cavities.

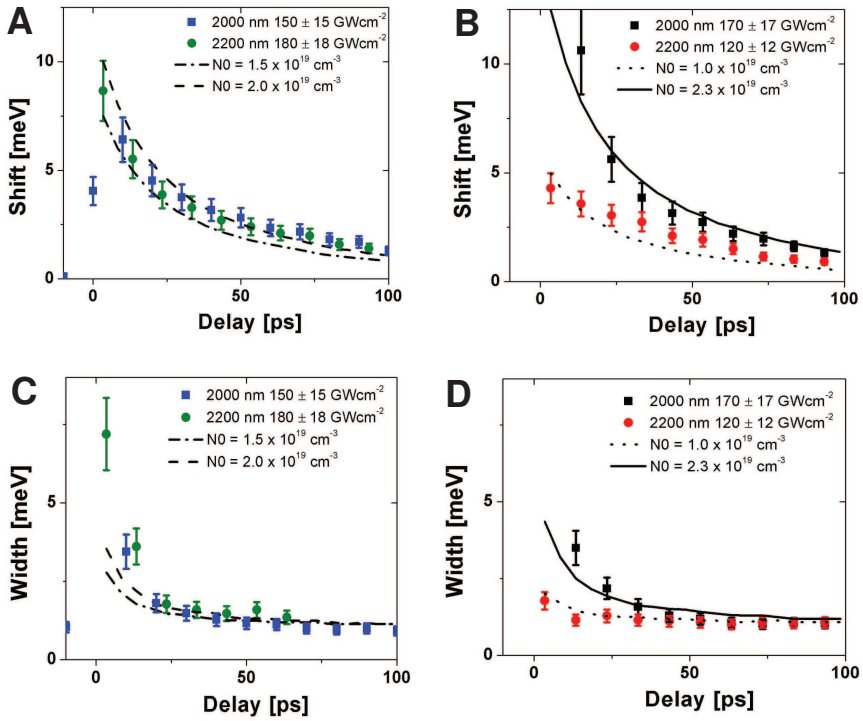

FIGURE 4.3: *Characteristics of the cavity resonance switched in reflection (A and C) and transmission (B and D) as a function of pump-probe delay. A and B show the shift of the center frequency of the resonance, while figure C and D show the width. The measurements are indicated with symbols, while the TM calculations are shown as lines. With an increasing pump-probe delay the shift of the cavity resonance decreases as shown in A and B. Similarly, the linewidth of the resonance decreases with delay, only at a different timescale, since it is determined mainly by the Bragg stacks. We pumped at 2000 nm and 2200 nm with 150* $GWcm^{-2}$ *and 180* $GWcm^{-2}$*, respectively.*

4.3.4 Shift and broadening of the cavity resonance

Figure 4.3 shows the measured and calculated shift (A and B) and width (C and D) versus time delay, for the switched cavity resonance measured in transient transmission and transient reflection. Figure 4.3 A shows that the calculated shift decreases with delay, which is in good agreement with the measured curves. The calculations were performed with relaxation time constants of the carriers of 14.7 ps and 62.9 ps for the free carrier densities in the Bragg stack and in the cavity layer, respectively. In the range of pump intensities measured, we observed that the relaxation times of the free carriers are constant. From the calculation we extract an initial carrier density of about 2×10^{19} cm^{-3} for both pump wavelengths. Although we pump at different intensities, the initial carrier density is equal due a three-photon absorption coefficient that decreases with increasing pump wavelength and is therefore smaller at 2200 nm than at 2000 nm [50].

Figure 4.3 B shows the resonance frequency shift versus pump-probe delay measured in transient transmission for two pump wavelengths. After an initial increase of the shift we observe a decrease with delay. The calculations show the same behavior. From the agreement between calculation and measurement we find that the carrier density is 1×10^{19} cm^{-3} in the case of a pump wavelength of 2200 nm and 2.3×10^{19} cm^{-3} in the case of a pump wavelength of 2000 nm. The carrier density with a 2000 nm pump wavelength is larger because of the higher intensity and the higher three-photon absorption coefficient compared to 2200 nm.

Figure 4.3 C shows the resonance linewidth versus pump-probe delay from the same measurements as shown in figure 4.3 A. The width initially increases with a 3 ps time constant, which is unresolvable with our delay resolution [13]. The initial increase of the width is attributed to thermalization of the carriers due to carrier-phonon interaction. After 10 ps, the linewidth of the cavity resonance starts decreasing with delay. There is good agreement between the measured and calculated linewidth for delays of 30 ps and larger. At shorter time delay, there is a discrepancy between the measured data and the calculation: The measured width is larger than the calculated one. This extra broadening might be a heating effect due to the thermalizing free carriers, but we were not able to reject or confirm this assumption.

Figure 4.3 D shows the resonance linewidth versus pump-probe delay as measured in transmission. The linewidth decreases with increasing delay and is constant within 1 meV after 30 ps. The calculation agrees well with the measured width. We find an initial

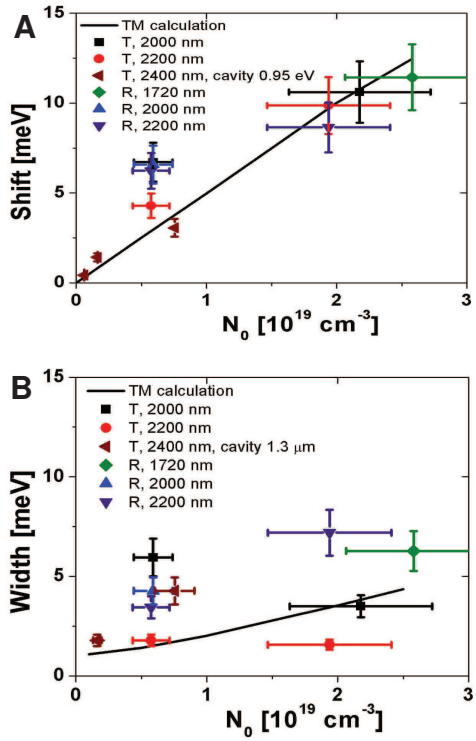

FIGURE 4.4: *(A) Measured (symbols) and calculated (line) shift versus carrier density at zero delay $\Delta\tau = 0$ for different pump wavelengths, measured in transient transmission and reflection. (B) Linewidth of the resonance versus carrier density. The symbols represent the measured values, the line represents the result of calculations using the TM model. For both the shift and the linewidth we measure an increase with increasing carrier density. We find a similar trend in the calculated data.*

carrier density of $1\times10^{19}\ cm^{-3}$ in the case of 2200 nm pump wavelength and $2\times10^{19}\ cm^{-3}$ in the case of 2000 nm pump wavelength. This is in agreement with the values extracted from the measured dependence of the resonance shift on time delay.

Figure 4.4 A shows the shift of the cavity resonance as a function of carrier density at zero delay. The symbols represent the measured data, while the line represents the transfer matrix calculations. We see a good agreement between the transfer matrix calculation and the measured data. We find a three-photon absorption coefficient of $12\times10^{-3}\ cm^3GW^{-2}$

at a pump wavelength of 2000 nm, 9×10^{-3} cm^3GW^{-2} at a pump wavelength of 2200 nm, and 6×10^{-3} cm^3GW^{-2} at a pump wavelength of 2400 nm.

Figure 4.4 B shows the linewidth of the cavity resonance versus the carrier density. The symbols represent the measured data and the lines the calculations. The measured width shows in general a poor agreement with the calculation. The measured width is larger than the calculated width. This extra broadening might be a heating effect due to the thermalizing free carriers, as mentioned above, but we were not yet able to incorporate this into the transfer matrix model to reject or confirm this scenario or other ones.

4.4 Recombination rate as a function of GaAs layer thickness

We further investigated the double exponential behavior of the cavity by fabricating a sample with a cavity resonance at 0.95 eV. To obtain such a sample, the layers of the stacks and the cavity are increased by about a factor of 1.3, which yields a resonance wavelength of 1300 nm in the telecom range. The result of a switch experiment performed on the cavity with a resonance at 0.95 eV compared to a switch experiment with the cavity resonance at 1.265 eV is shown in figure 4.5. It can clearly be seen that the shift of the 0.95 eV structure decays slower than the shift of the 1.265 eV structure. The initial shift is different because of the different pump intensities and the different three-photon absorption coefficients [50].

The deduced recombination rates are shown in figure 4.6 together with a fit for each sample. It can be seen that in both cases the recombination rate increases with GaAs layer thickness. Furthermore, the ratio of the recombination rate in the cavity and the recombination rate in the stack layers are in both cases equal to four. This is equal to the thickness ratio of the cavity layer and the layers in the stack. Figure 4.6 also shows that the recombination rate per unit thickness is not equal for both samples. The reason for the slower recombination rate of the 0.95 eV structure is attributed to a higher quality of the GaAs interface.

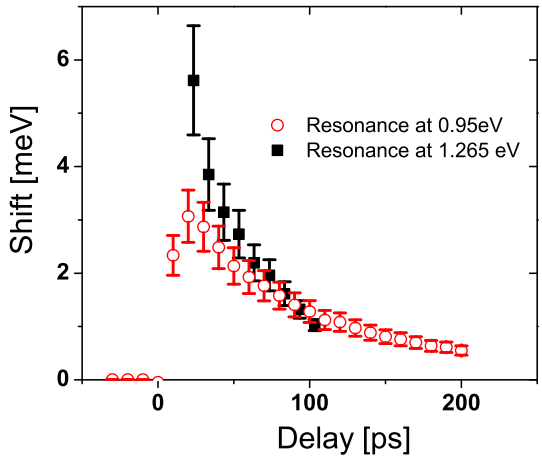

FIGURE 4.5: *Shift as a function of delay for a cavity with a resonance at 0.95 eV (circles) and a cavity with a resonance at 1.265 eV (squares). The 0.95 eV structure was pumped at 2400 nm, while the 1.265 eV structure was pumped at 2200 nm.*

4.5 Conclusion and outlook

We have studied ultrafast optical switching of a microcavity in both transmission and reflection. We studied the three-photon regime in order to minimize absorption and open the avenue to instantaneous electronic Kerr switching. We compared our results to transfer matrix calculations and found that the shift agrees very well with our model. The width of the cavity resonance has less agreement between measured width and calculated width: at earlier delays the measured width is larger, but at larger delays the theory agrees with the data.

We showed that our model applies also to microcavities with thicker layers and resulting larger resonance wavelengths. We obtained the recombination rate for both samples and showed that there is a linear dependence of thickness in each of the samples, as expected from our new model.

We found a relaxation time for the free carriers in the order of 60 ps. By tuning the sample properties it is expected that this time can be reduced to about 5 ps, which means we could achieve a rate of 0.2 THz. In the experiments discussed in this chapter we used a power of 1 μJ/pulse. One can considerably reduce the power per pulse needed for cavity

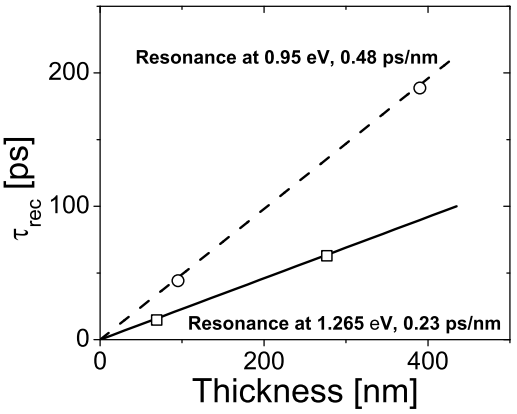

FIGURE 4.6: *Recombination rate as a function of GaAs layer thickness for two different samples. The solid line is a fit through the data points from the sample with a cavity resonance at 1.265 eV, the dashed line for the cavity with a resonance at 0.95 eV.*

switching by employing a smaller volume by using a pillar shaped sample with a cross section of 1 μm. If we only switch the λ-layer the homogeneity length can be relaxed to less than 280 nm, which means that we can pump in the one-photon absorption regime. Switching only the λ-layer can be achieved by making the Bragg mirrors transparent to the pump beam, i.e., using a stack of AlAs and $Al_xGa_{1-x}As$ with large electronic bandgap. Then, the pump wavelength can be chosen as short as 600 nm, such that the absorption length is on the order of 300 nm. In that case, the required pump pulse energy can be reduced by a factor of 10^2 Furthermore, in case of a pillar, the spot size of the pump can be much smaller than the 100 μm as described in this chapter, by a factor of 100^2. We can therefore conclude that it is possible to switch a pillar cavity with at least 10^6 lower pulse energy, or as little as 1 pJ/pulse.

CHAPTER 5

Ultimate fast all-optical switching of GaAs/AlAs nanostructure and microcavity

5.1 Introduction

Exciting prospects arise when photonic nanostructures are switched on ultrafast timescales. It has been predicted that this could lead to ultrafast control over the photonic density of states and thus to ultrafast cavity quantum electrodynamics [43]. Switching the directional properties of photonic crystals also leads to fast changes in the reflectivity, where interesting changes have been reported for one-dimensional Bragg stacks [92, 93], two-dimensional photonic crystals [94–96], first-order stopbands of three-dimensional opaline crystals [97, 98] and three-dimensional photonic bandgap crystals [46, 47]. Ultrafast control of the propagation of light is essential to applications in active photonic integrated circuits [99].

Of particular interest is the ultrafast switching of the resonance frequency of cavities, where light can be confined for a long time in a tiny volume; such switching permits the manipulation of the stored light, or of light sources in the cavity. Furthermore, switching would allow the capture or release of photons from photonic band gap cavities [43], which is relevant to solid-state slow-light schemes [100]. In order to switch a cavity, the induced refractive index change should be large enough. To shift the cavity resonance by one linewidth the refractive index change should exceed $\frac{\Delta n'}{n'} = \frac{1}{Q}$ [47]. Thus for an experiment or a device with a cavity having a moderate quality factor Q = 1000, this implies a refractive index change of 0.1%. Here we are pursuing the ultimate fast switching

speed of a microcavity with on and off switching times τ_{on} and τ_{off}. This extreme of fast switching could be used for capturing and releasing photons on demand for example in a vertical-cavity surface emitting laser [101]. It would be truly exciting to not only have the switching times faster than the cavity storage time τ_{cav}, but also of the order of the cycle time τ (=λ/c). In these cases novel physical phenomena are expected including non-adiabatic switching [43].

Several different physical mechanisms are possible for fast switching of photonic structures. The switching of photonic structures with free carriers [13, 94, 96, 102] and a structural phase transition of VO_2 [103] have been reported recently. The disadvantage of such a phase transition is that the material changes from a transparent material to a metal, which absorbs light. On the other hand free carrier excitation is ultrafast with minimal absorption [104], but the recombination of the carriers limits the switch-off time τ_{off} to a few picoseconds.

Instantaneous on- and off-switching is feasible with nonlinear refractive index that physically exploits the electronic Kerr effect. The instantaneous nature of the electronic Kerr effect can be seen from the expression for the polarizability **P** of a material pumped with a frequency ω_1 and probed with a frequency ω_2. The polarizability of a material with $\chi^{(1)}$, $\chi^{(2)}$ and $\chi^{(3)}$ measured at probe frequency ω_1 under the influence of a high intensity pump pulse with frequency ω_2 is given by

$$\mathbf{P} = \chi^{(1)}\mathbf{E} + \chi^{(2)}\mathbf{EE} + \chi^{(3)}\mathbf{EEE}. \tag{5.1}$$

In general the second term drops out due to inversion symmetry of the crystal [48], which leaves the first and third order term. Taking into account that we are interested in effects at the probe frequency ω_1 yields for the polarization $\mathbf{P}^{(3)}$ due to third order term $\chi^{(3)}$

$$\mathbf{P}^{(3)}(\omega_1, t) = 6\chi^{(3)}(\omega_1 = \omega_1 + \omega_2 - \omega_2)|\mathbf{E}(\omega_2, t)|^2\mathbf{E}(\omega_1, t). \tag{5.2}$$

It is clear from Eq. 5.2 that the polarizability depends on the instantaneous field amplitudes, making the Kerr effect truly ultimately fast.

In practice, the duration of the electronic Kerr effect is limited by the duration of the pump and probe pulses, which is in the order of femtoseconds rather than picoseconds as with free carrier switching. Therefore, this switching mechanism potentially allows beyond-THz modulation rates that could be of use for extremely fast datamodulation. It

is widely assumed (see [43]) that the magnitude of the refractive index change by the Kerr effect is much smaller than the change due to a free carrier switch. Therefore, most switching schemes use free carriers and are therefore limited to picosecond timescales. Furthermore, a problem which occurs at coincidence of pump and probe pulse is non-degenerate two-photon absorption [13, 48]. Here, a probe photon is absorbed together with a pump photon when the summed energy of the pump and probe photon exceeds the bandgap energy, see figure 5.1 B.

The origin of the absorption is explained in figure 5.1 A and 5.1 B, which show schematic energy diagrams at coincidence of pump and probe. In the densely hatched spectral region in figure 5.1 C, the pump and probe photon will be absorbed since the sum of the photon energies is higher than the bandgap of GaAs (situation figure 5.1 B). In the sparsely hatched (dispersive) spectral region in figure 5.1 C however, the sum of pump and probe photon energies is less than the bandgap of GaAs (as in figure 5.1 A). Therefore, absorption is low in this region and the behavior at coincidence is mainly dispersive. Only the real part of the refractive index *n'* changes. The regions are separated at a probe wavelength which corresponds to 1340 nm at a pump wavelength of 2400 nm. The change in imaginary part of the refractive index can be large compared to the change in the real part, giving rise to absorptive changes in the optical properties. Recently, however, a nonlinear figure of merit has been identified to find conditions where absorption can be minimized [89].

In this work we demonstrate a method to decrease non-degenerate two-photon absorption at pump and probe coincidence. Because of this, we observe that the electrical Kerr effect is surprisingly large and competitive with free carrier effects. We demonstrate that a cavity resonance with a moderate Q of 1000 is successfully switched instantaneously. We derive the Kerr coefficient and the three-photon absorption coefficient over a broad wavelength range. We demonstrate with a pump-probe experiment that the reflectivity of a cavity resonance at telecom wavelength, more precise its resonance frequency, and its width can be switched on an ultimate fast time scale.

5.2 Experimental

5.3 Linear reflectivity

Figure 5.1 C shows the measured linear reflectivity spectrum of the 980 nm sample and a transfer matrix (TM) calculation [105]. The transfer matrix calculation including the dispersion of GaAs [73] and AlAs [74] reproduces the experimental resonance, stopband, and Fabry-Pérot fringes. The only free parameters in the model were the thicknesses of the GaAs (d_{GaAs} = 69.2 nm) and AlAs (d_{AlAs} = 81.0 nm), which agree with fabrication parameters. The reflectivity spectrum shows the stopband with the cavity resonance at 10204 cm^{-1} (λ = 980 nm) and the Fabry-Pérot fringes. The spectrum can be divided into two spectral regions, namely 'Absorptive' (right, densely hatched) and 'Dispersive' (left, hatched), referring to the expected behavior if pump and probe coincide.

The origin of the dispersion is the electronic Kerr effect. There will be a change in the real part of the refractive index (*n'*), due to the pump field. The edge of the hatched regions in figure 5.1 C will shift to the red at a pump wavelength of 2000 nm, indicating that we expect absorption in a large part of the spectrum. The behavior at coincidence is therefore mainly absorptive, meaning a change in the imaginary part of the refractive index (*n"*).

With the 980 nm sample we focus on the spectral region indicated by the black rectangle in figure 5.1. In this region we expect to observe effects of the electronic Kerr effect but only little absorption at 2400 nm pump wavelength, while we expect mainly absorption at 2000 nm pump wavelength.

Figure 5.2 shows the measured linear reflectivity spectrum of the 1300 nm cavity. The measured reflectivity spectrum shows a stopband from 7100 cm^{-1} to 8100 cm^{-1} and cavity resonance at 7692 cm^{-1} (or λ = 1300 nm) and the Fabry-Pérot fringes. The transfer matrix calculation including the dispersion of GaAs [73] and AlAs [74] reproduces the experimental resonance, stopband, and Fabry-Pérot fringes very well. The only free parameters in the model are the thicknesses of the GaAs (d_{GaAs} = 96.3 nm) and AlAs (d_{AlAs} = 113 nm), and the thickness of the cavity layer d_{cav} = 373 nm. The measured reflectivity is a bit lower than the calculated one, because of a slight systematic error in the reference spectra.

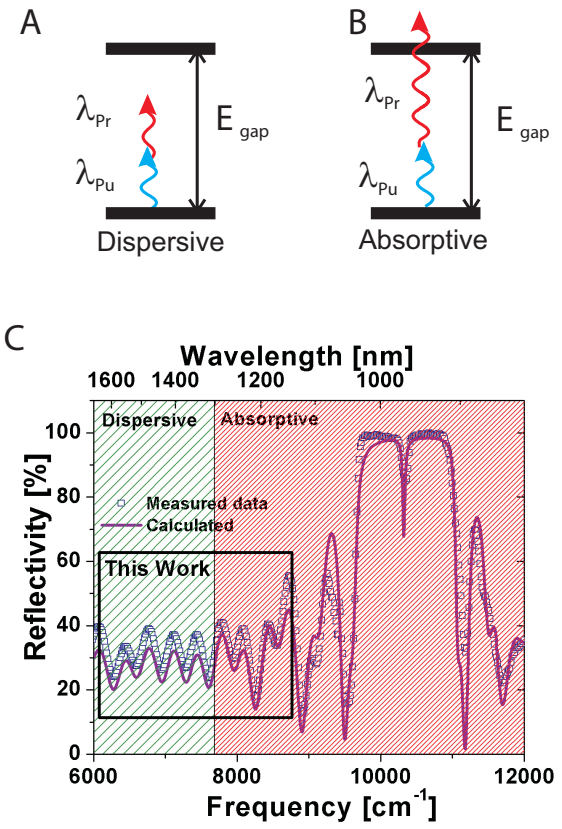

FIGURE 5.1: *(A,B) Schematic energy diagrams of GaAs. E_{gap} is the electronic bandgap of GaAs, λ_{Pr} is the probe wavelength and λ_{Pu} is the pump wavelength. In the dispersive spectral region the summed energy of a pump and a probe photon is smaller than the electronic bandgap (A), while the summed energy is larger in the absorptive spectral region (B). (C) Linear reflectivity spectrum and transfer matrix calculation of the GaAs/AlAs structure. The trough at 980 nm is due to the cavity resonance of the λ-thick GaAs layer. The slight difference in amplitude of the measured and calculated reflectivity on the red side of the stopband is caused by a small error in the normalization measurement. The edge between diagram A and B is at a probe wavelength of 1510 nm and 1340 nm at pump wavelengths of 2000nm and 2400nm respectively. We present measurements in the spectral region indicated with a box, to obtain a change in the real part of the refractive index.*

5.4 Electronic Kerr switching of Fabry-Pérot fringes

The two plots in figure 5.3 show the differential reflectivity of the 980 nm structure measured at pump wavelengths 2000 nm (A) and 2400 nm (C) as a function of probe wave-

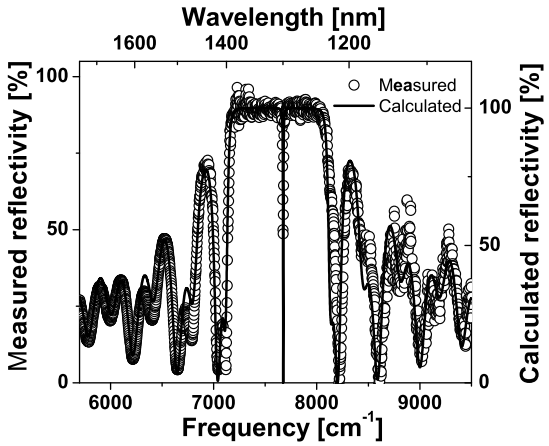

FIGURE 5.2: *Measured (symbols) and calculated (line) reflectivity spectra of the stack. Fabry-Pérot fringes are visible on both sides of the stopband. Within the stopband a trough in reflectivity indicates the cavity resonance at 7692* cm^{-1} *(or* $\lambda = 1300$ *nm).*

length and delay. A fringe pattern is visible in figure 5.3 A and C for coincidence of pump and probe and for positive delay.

The fringe pattern in figure 5.3 A and 5.3 C results from Fabry-Pérot fringes within the stack forming the optical microcavity. A change in *n'* modifies the optical thickness of the GaAs layers; it induces a spectral shift of the Fabry-Pérot fringes, which results in a periodic differential reflectivity. A change in *n"* decreases the modulation depth of the Fabry-Pérot fringes and also results in a periodic differential reflectivity.

Figure 5.3 B and D show cross sections of 5.3 A and C. The sign difference of differential reflectivity between pump and probe overlap and positive delay is apparent and is a result from the fringe patterns at coincidence and positive delay, which are spectrally shifted with respect to each other. This indicates that the switch mechanism at coincidence is different from the free-carrier mechanism at positive delay. Figure 5.3 D shows that there is a competition between the instantaneous effect and the free carrier effect. The traces in figure 5.3 B and D clearly reveal that the instantaneous effects occur over a time range of ±250 fs. This duration agrees well with the cross correlation of the pump and the probe pulse of $\sqrt{2}\times$140 fs = 196 fs. Therefore the data signal switch-on and switch-off times of 200 fs.

The differential reflectivity at positive delay is caused by excited free carriers. Figure 5.4 shows the power dependence of differential reflectivity ($\Delta R/R$) at positive delay. There is a linear relation between the differential reflectivity and the power cubed. We therefore conclude that the differential reflectivity is caused by free carriers generated by a three-photon absorption process.

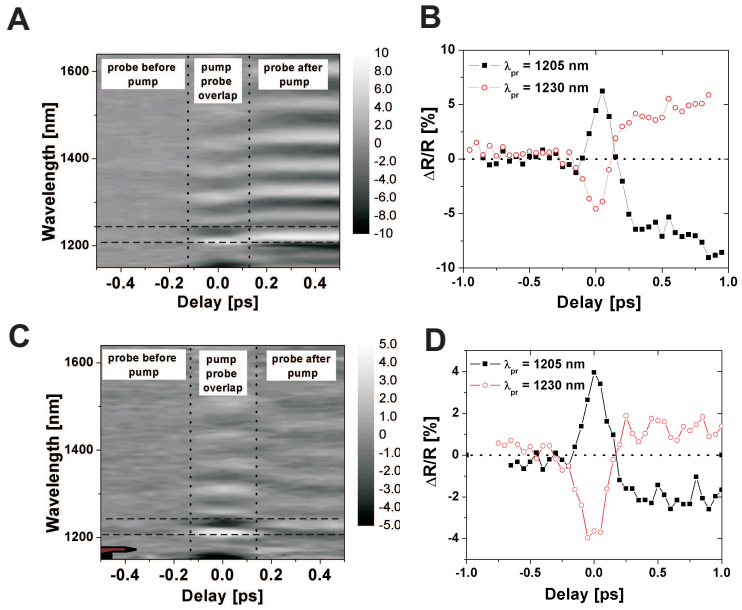

FIGURE 5.3: *Differential reflectivity per wavelength as a function of delay between pump and probe pulse. At negative delays the pump hits the sample before the probe. The scans were measured at different pump wavelengths. (A) λ_{pump} = 2000 nm, I_{pump} = 90 GW/cm^2, (C) λ_{pump} = 2400 nm, I_{pump} = 95 GW/cm^2. Cross sections indicated by dashed lines in A and C are shown in figure B and D respectively. Figure A and C show a fringe pattern due to a shift of the Fabry-Pérot fringes. The cross sections B and D show that the sign of the differential reflectivity at coincidence is different from the sign at positive delay.*

At a pump wavelength of 2000 nm we expect an instantaneous change in *n"*, since we are in the absorptive regime. At 2400 nm pump wavelength we expect an instantaneous change in *n'* and a negligible change in *n"*, since we are in the dispersive region (see figure 5.1). The differential reflectivity $\frac{\Delta R}{R}$ due to a change in the real part of the refractive

index depends on measured intensities as follows:

$$\frac{\Delta R}{R}(\tau, \omega_{pr}, \omega_{pu}) = \frac{I_{pu}(\tau, \omega_{pr}, \omega_{pu}) - I_{unpu}(\omega_{pr})}{I_{unpu}(\omega_{pr})}, \tag{5.3}$$

where τ is the delay between pump and probe, ω_{pr} is the probe frequency, ω_{pu} is the pump frequency, I_{unpu} is the reflectance measured if the structure is unpumped and I_{pu} is the reflectance measured if the structure is pumped. In case of a change in the real

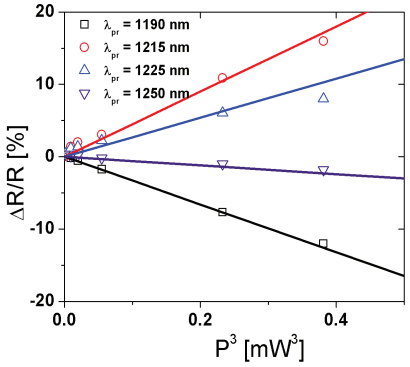

FIGURE 5.4: *Differential reflectivity at positive delay measured at different probe wavelengths at a pump wavelength of 2000 nm. The differential reflectivity is plotted as a function of pump power cubed. The relation between the differential reflectivity at positive delay and the power cubed is linear. We conclude that the carriers are solely generated through a three-photon process.*

part of the refractive index, the fringe pattern shifts spectrally $\Delta\omega_{pr} = \alpha n'$, with α a proportionality constant that depends on the exact structure of the fringe pattern. I_{pu} is then given by:

$$I_{pu}(\tau, \omega_{pr}, \omega_{pu}) = I_{unpu}(\omega_{pr} + \Delta\omega_{pr}(\tau, \omega_{pu})), \tag{5.4}$$

which can be Taylor expanded as

$$I_{pu}(\tau, \omega_{pr}, \omega_{pu}) = I_{unpu}(\omega_{pr}) + \frac{\partial I_{unpu}(\omega_{pr})}{\partial \omega_{pr}} \Delta\omega_{pr}(\tau, \omega_{pu}), \tag{5.5}$$

which yields a differential reflectivity:

$$\frac{\Delta R}{R}(\tau, \omega_{pr}, \omega_{pu}) = \frac{1}{I_{unpu}(\omega_{pr})} \frac{\partial I_{unpu}(\omega_{pr})}{\partial \omega_{pr}} \Delta\omega_{pr}(\tau, \omega_{pu}). \tag{5.6}$$

Equation 5.6 shows that in the case of a change in the real part of the refractive index a large differential reflectivity will be observed where the unpumped reflectivity has a large derivative, which is spectrally between successive maxima and minima of the Fabry-Pérot fringes. This is illustrated in figure 5.5, which shows results of a transfer matrix calcula-

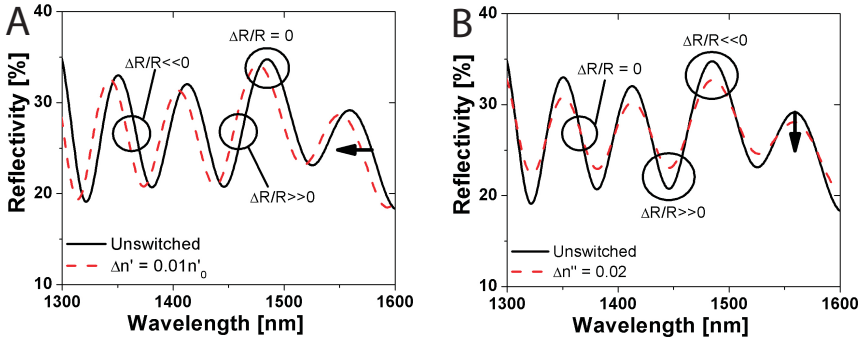

FIGURE 5.5: *Calculated switched and unswitched reflectivity for a change in the n' (A) and a change in n" (B). The calculation was done with a transfer matrix model using parameters relevant to our structure. (A) A change in n' causes a shift of the fringe pattern. The introduction of absorption* n" *mainly affects the modulation depth of the fringes (B). The differential reflectivity has maxima at different frequencies, which makes it possible to distinguish between a purely dispersive and a purely absorptive regime.*

tion using parameters relevant to our structure. In the case of a change in *n'* the frequency of the fringe pattern is shifted. Due to the shift in frequency the differential reflectivity is maximum at the frequencies were the slope of the fringe pattern is maximum, i.e., at the flanks of the fringes. In the case of a change in *n"* the modulation depth of the fringe pattern is affected. Due to the change in modulation depth, the maximum change in reflectivity is observed at the maxima and minima of the Fabry-Pérot fringe pattern. For this reason the differential reflectivity has maxima at different frequencies making it possible to distinguish between a purely dispersive and a purely absorptive regime.

Figure 5.6 shows a comparison between the measured and calculated differential reflectivity pattern. The intensity profile in the structure is homogeneous, leading to a homogeneous refractive index change, hence we can quantitatively interpret the spectra. The intensity profile is homogenous since we pump at a long wavelength in the three-photon absorption regime. The homogeneity length [104] is longer than the thickness of our sample. Comparing the measured and calculated patterns shows that the frequencies of the

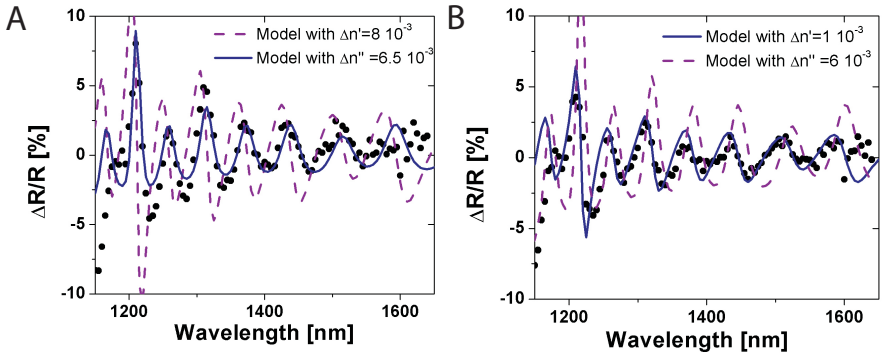

FIGURE 5.6: *Cross section of figure 5.3 (black solid circles) showing the differential reflectivity $\Delta R/R$ as a function of probe wavelength at pump-probe coincidence ($\Delta t = 0$ ps). The structure was pumped at 2000 nm (A) and 2400 nm (B). The solid and dashed lines are results from transfer matrix calculations. In (A) the dashed line represents a change in the real part of the refractive index while the solid line represents a change in the imaginary part of the refractive index. Conversely in (B) dashed represents a change in imaginary part, while solid represents a change in the real part of refractive index. As expected we see mainly a change in* n" *at 2000 nm pump and a change in* n' *at 2400 nm.*

peaks and troughs in the differential reflectivity pattern near zero delay are caused by a change in the imaginary part of the refractive index (n") in the case of 2000 nm pump and a change in the real part of the refractive index (n') in the case of 2400 nm pump. We conclude that in the case of 2400 nm pump wavelength the fringe pattern near zero delay in the differential reflectivity originates from an electronic Kerr switch, since the process is ultrafast, instantaneous with the laser pulse, and dispersive. Interestingly, there is a competition between the Kerr and free carrier effects, with the Kerr effect responsible for a $\Delta n' > 0$ and the free carrier effect for a $\Delta n' < 0$. Surprisingly, the electronic Kerr

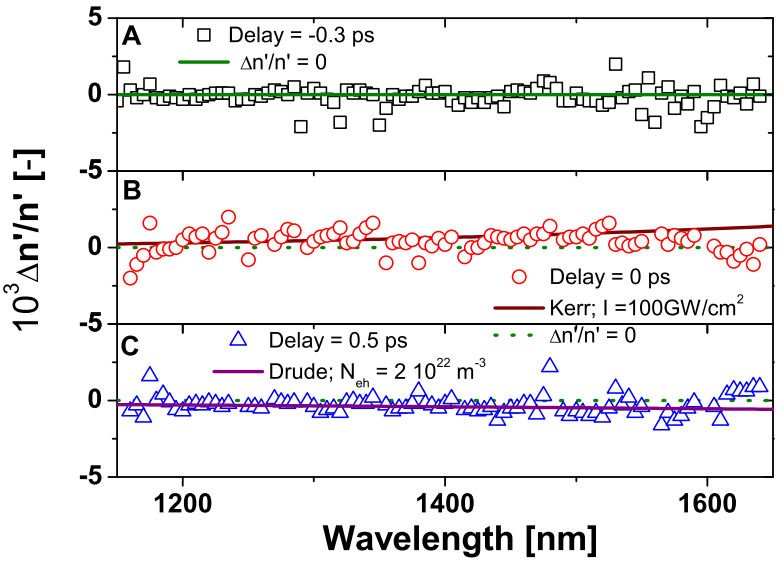

FIGURE 5.7: *Relative change of refractive index due to a 2400 nm pump as a function of probe wavelength at a delay of -0.3 ps (A), 0 ps (B) and 0.5 ps (C). The dashed line in all three cases represent no change in refractive index. The solid line in (B) represents the dispersion of the change in refractive index from [49]. The solid line in (C) is calculated with the Drude model for free carriers [24]. Points obtained from spectral regions close to extrema of the fringes were removed, because of their poor precision.*

effect is larger than the free carrier effect in this wavelength range. A comparable result to the present GaAs results has recently been obtained for Si photonic crystals [89].

In case of 2000 nm pump wavelength the fringe pattern originates from non-degenerate two-photon absorption. Furthermore, we see a slight deviation of our model near the blue side of the spectrum, indicating some dispersion in the nonlinear effect. We further conclude from figure 5.6 that absorption can be neglected at 2400 nm pump wavelength.

By varying the magnitude of the change in *n'* we have extracted the change in refractive index at each probe wavelength. The results are plotted together with dispersion curves in figure 5.7. Figure 5.7 shows no change in refractive index for a negative delay (A), a positive change for zero delay (B) and a negative change for positive delay (C). Furthermore there is a good agreement between the data and the dispersion of the electronic Kerr effect [49] and the dispersion of the free carrier excitation [24]. The scattered

symbols deviating strongly from the theoretical model can be attributed to small differences in shape of the measured and calculated reflectivity spectrum. A slight deviation is amplified by the fitting procedure since we extract the refractive index change by fitting the differential reflectivity at one wavelength position.

Figure 5.7 B shows that the change in refractive index induced by the optical Kerr effect is in the order of 0.1%. This is large enough to switch a cavity with a moderate quality factor $Q = 1000$. From our experiments two consequences follow for the design of a GaAs cavity that can be Kerr switched. First the cavity should be pumped at 2400 nm or higher. Furthermore, the resonance of the cavity should be in the spectral region of 1300 nm or higher (see figure 5.1 C), which is studied in the next section.

5.5 Electronic Kerr switching of microcavity

In order to interpret the results on the Kerr switching of a cavity, we show in figure 5.8 A the pulse scheme for three delay regions. The Gaussian-shaped pump pulse with a duration of 120 fs is shown at the top of the scheme. The probe pulse is shown at the bottom of the scheme. Since we probe the structure with light reflected and stored in the cavity, it has an asymmetric shape. The probe is shaped like the intensity in the cavity (see chapter 3). A fast increase in intensity when the probe pulse (120 fs) arrives followed by a much slower exponential decay. The duration of the probe is 2 ps, which is determined by the storage time of the pulse in the cavity and therefore by the quality factor of the cavity. In delay region I the cavity is probed before it is pumped, while in delay region III the cavity is probed after the pump pulse arrived. In delay region II, the pump pulse arrives simultaneously with the probe pulse. In delay region II we expect to find the electronic Kerr effect.

Figure 5.8 B shows transient reflectivity of the 1300 nm sample measured with the pump-probe setup as a function of frequency and delay. The measured reflectivity is not the instantaneous reflectivity but transient reflectivity. The probe pulse impinges at delay Δt and is stored during the storage time of the cavity. The measured transient reflectivity therefore contains information on the cavity resonance during the cavity storage time and not just at the delay Δt. In delay region I the resonance, the transient reflectivity trough at 7685 cm^{-1}, is not influenced by the pump. In delay region II, where pump and probe coincide, the resonance broadens and shifts rapidly to lower frequencies. Since the

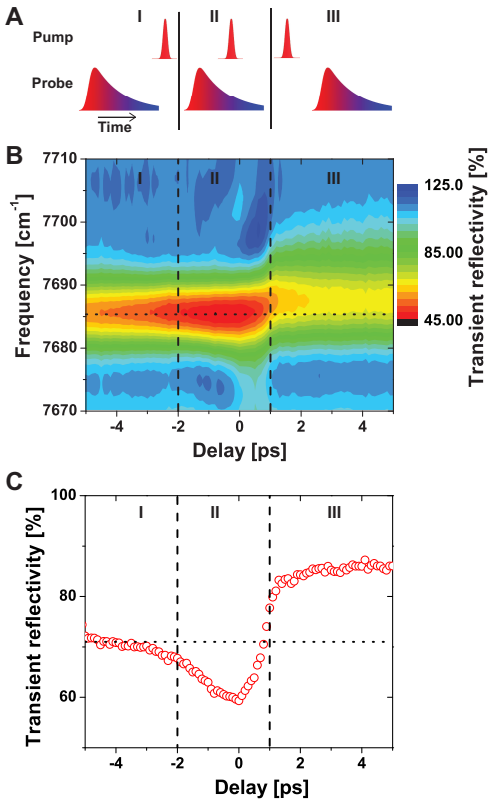

FIGURE 5.8: *(A) Schematic of pump and probe pulses in three time delay regions (I, II and III). The pump is Gaussian shaped and arrives in region I after the probe, while it arrives before the probe in region III. In region II the pump pulse arrives simultaneously with light stored in the cavity. (B) Reflectivity as a function of frequency and time delay between pump and probe. In delay region I the resonance, visible as a reflectivity minimum, is not influenced by the pump. (C) Transient reflectivity as at the unswitched cavity resonance frequency (7685.35 cm^{-1}) as a function of delay. In region I we see a constant reflectivity indicated by a dotted line. In region II the transient reflectivity decreases, with a minimum value at pump-probe coincidence. In the third region the reflectivity increases again.*

Kerr signal is a cross-correlate of pump and probe and since the probe is asymmetrically broadened (see figure 5.8 A) the cross correlate is also asymmetrically broadened. The shift to a lower frequency can be explained by the increase in refractive index, which corresponds to a positive Kerr coefficient as expected from theory and the previous section. The signature of the Kerr regime for GaAs in this frequency region is that the real part of the refractive index increases at pump-probe coincidence, which is the case in figure

5.8 B. From this observation we conclude that we are the first to ever switch a photonic microcavity using the electronic Kerr effect.

In delay region III the resonance shifts to the blue due to free carriers generated by the pump pulse. The regime in the third delay region has been studied extensively in [13, 94, 96, 102] and elsewhere in this thesis (chapter 6 and chapter 4).

Figure 5.8 C shows the transient reflectivity at the unswitched cavity resonance frequency (7685.35 cm^{-1}) as a function of delay. In delay region I and III we see a constant reflectivity, while in delay region II the transient reflectivity decreases, with a minimum value at pump-probe coincidence. The reflectivity in the third region is higher than in delay region I, because the resonance shifts to the blue due to the excited free carriers. The shape of the reflectivity decrease in delay region II results from the cross correlation between the cavity intensity and the pump pulse as indicated in figure 5.8 A. Figure 5.8 C shows that we are able to switch the reflectivity from 60 % to 50 % within 2 ps.

The counter-intuitive decrease in transient reflectivity in figure 5.8 C can be explained by the increase of the refractive index in the GaAs layers, resulting in a higher refractive index contrast in the Bragg stack and thereby an increase of the mirror reflectivity. The higher mirror reflectivity leads to a narrower cavity resonance enabling less probe-photons to enter the cavity resonance than in the unswitched case. Since less photons can excite the cavity resonance, we measure a lower intensity and therefore a lower transient reflectivity.

Since the Kerr signal is a cross correlate, one has to take into account that the 120 fs probe pulse excites the cavity, whose intensity decays with a typical 2 ps time constant. During about 2 ps there is still light in the cavity that probes the structure at the moment the pump pulse arrives (see figure 5.8 A). However the resonance only shifts while the 120 fs pump pulse is present. In the other 1.9 ps the resonance is unswitched. The measured spectrum is therefore the integral of unswitched and switched spectra and is influenced by the ratio of pump pulse duration and cavity storage time. This also explains why the shift is maximum at pump and probe coincidence, since at that moment the cavity is maximally charged and therefore the maximum effect is observed. The resonance shift due to the optical Kerr effect can be enhanced by matching the pump pulse duration to the photon dwell time in the cavity.

Figure 5.9 A shows the measured transient reflectivity spectrum (cross section of figure 5.8 B) of the unpumped structure and at pump-probe coincidence. The trough results from the cavity resonance. The width of the unpumped cavity resonance corresponds to a cavity quality factor of 1325, which corresponds to a cavity storage time of 0.9 ps. This is

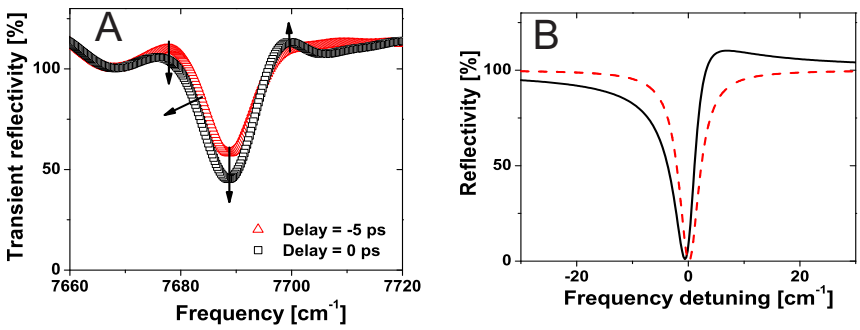

FIGURE 5.9: *(A) Measured reflectivity spectra of the unpumped structure (Delay = -5 ps, triangles) and of the structure at coincidence of pump and probe (Delay = 0 ps, squares). The width of the unpumped cavity resonance corresponds to a cavity quality factor of 1325, which corresponds to a cavity dwell time of 0.9 ps. This is in agreement with the time of the probe duration. At pump and probe coincidence the resonance broadens, shifts to the red and the trough becomes deeper. There is an enhancement of the reflectivity on the blue side of the resonance. The structure was pumped at 2400 nm wavelength with 1.5 μJ pulse energy. (B) Calculated reflectivity spectra of the unpumped (dashed) and pumped (solid) structure. At pump and probe coincidence the resonance broadens and shifts to the red. Furthermore, there is an enhancement of the reflectivity on the blue side of the resonance.*

in agreement with the time of the probe duration, which is twice the cavity storage time, as expected. At pump and probe coincidence we observe a red shift of the red edge of the resonance. Since we measure transient reflectivity the shift leads to a broadening of the resonance. Furthermore, we see a decrease in the resonance reflectivity and an enhancement of the reflectivity on the blue side of the resonance. The enhancement on the blue side of the resonance is the result of a fringe pattern that appears as a result of the interference between the first reflected probe pulse and a part of light stored in the cavity that is ejected at the moment the pump pulse arrives (see also [13]). The sum of the two pulses in the time domain yield a beating in the frequency domain. This generates the fringe pattern that causes the enhancement on the blue side.

Figure 5.9 B shows transient reflectivity of the unpumped structure and at coincidence of pump and probe calculated with a dynamic Fabry-Pérot model that is discussed in chapter 6 [70, 105]. The calculation at coincidence was performed with an increase in the real part of the refractive index of 0.0035, which is equal to about $\frac{\Delta n}{n_{GaAs}} = 0.1\%$. This value is in agreement with previous sections [50]. At pump and probe coincidence we observe a red shift of the red edge of the resonance, leading to a broadening of the resonance as

we observed in the measurement. Furthermore, we see an enhancement of the reflectivity on the blue side of the resonance, corresponding to the enhancement in the measurement.

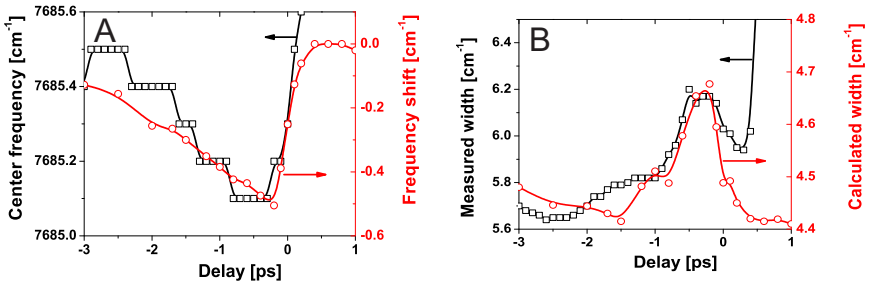

FIGURE 5.10: *(A) Measured (squares) and calculated (circles) resonance frequency versus pump-probe delay. The measured center frequency starts shifting at -2.5 ps and reaches its maximum shift of -0.4 cm^{-1} at -0.55 ps. At -0.2 ps the resonance frequency increases again. The calculated shift starts increasing slightly earlier as the measured shift at -3 ps and reaches its maximum at -0.2 ps. (B) Measured (squares) and calculated (circles) width versus pump-probe delay. The measured width of the cavity resonance starts increasing at -1.1 ps and reaches its maximum at -0.3 ps. At -0.1 ps the measured width decreases again and after a local minimum increases again due to free carrier generation. The calculated width increases at -0.9 ps and reaches its maximum value at -0.2 ps after which it decreases.*

Figure 5.10 A shows the measured and calculated resonance frequency as a function of delay. The calculations, which were done using the dynamic Fabry-Pérot model, agree quantitatively very well with the measurements. The measured resonance frequency starts to shift to the red at -2.5 ps and reaches its maximum apparent shift of -0.4 cm^{-1} at -0.55 ps. The shift is smaller than $\frac{1}{Q}$, since the cavity is only pumped during a fraction (1/20) of the cavity storage time. Taking this into account leads to a shift of 1.4 linewidths, which agrees with 0.1 % change in refractive index. The resonance shift due to the optical Kerr effect can be enhanced by matching the pump pulse duration to the photon dwell time in the cavity in order to measure the full linewidth shift. At -0.2 ps the resonance frequency increases again due to free carrier generation. The red shift starts at -3 ps and reaches its maximum at -0.2 ps, very close to the measured values. The amplitude of the measured and calculated shifts agree very well.

Figure 5.10 B shows the measured and calculated width as a function of delay. The measured width increases at -1.1 ps and reaches its maximum value at -0.3 ps, after which it increases further due to free carrier generation. The calculated width agrees very well with the measured one. The small difference in unswitched width is attributed to inhomogeneous broadening (see chapter 3) The width starts to increase at -0.9 ps and reaches its maximum at -0.2 ps, very close to the maximum of the measurement. The decrease of the width before -1.1 ps is the result of the fringe pattern, originating from the interference between the injected and reflected pulses.

5.6 Nonlinear coefficients GaAs

5.6.1 Kerr coefficient n_2 for GaAs

The non-degenerate Kerr coefficient n_2 can directly be extracted from the data $\Delta n'$ in figure 5.7 using the relation [48, 49],

$$n_2 = \frac{\Delta n'}{2I_0} \tag{5.7}$$

where I_0 is the pump intensity. Since n_2 scales with E_{gap}^{-4} [49], the contribution of AlAs is only 20% of the total n_2. For simplicity we therefore assume that mainly the GaAs is switched.

The resulting Kerr coefficients are plotted in figure 5.11. Figure 5.11 shows the raw data extracted from figure 5.7 (open circles) and the data averaged over the width of a fringe (solid squares). The order of magnitude of n_2 is $10^{-4} GW cm^{-2}$. The non-degenerate Kerr coefficient decreases with increasing wavelength. This dispersive behavior was already observed in figure 5.6.

The values of n_2 measured in our non-degenerate pump-probe experiment are similar to the ones reported in the literature for degenerate pump-probe experiments [106–108]. We find this surprising since we pump at a wavelength twice as long as in the degenerate case. This result enables us to modify efficiently the refractive index with a far detuned pump wavelength.

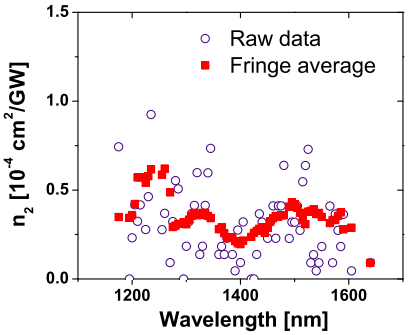

FIGURE 5.11: *Measured non-degenerate Kerr coefficient n_2 as a function of probe wavelength (open circles). We averaged the data over the period of one fringe, since the coefficients are correlated within this fringe period (solid squares). We observe dispersion in n_2 towards the blue side of the spectrum as expected from figure 5.6.*

5.6.2 Three-photon absorption coefficient γ for GaAs

Figure 5.7 shows that we are able to derive a carrier density from the measured change in refractive index with the use of the Drude model. We will discuss in this section the three-photon absorption coefficient γ. Figure 5.12 shows the three-photon absorption coefficient

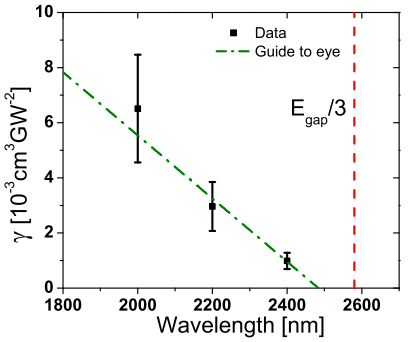

FIGURE 5.12: *Three-photon absorption coefficient as a function of wavelength extracted from the differential reflectivity data. The relative error of 30 % is indicated.*

γ as a function of pump wavelength. The order of magnitude of γ is $10^{-3} cm^3 GW^{-2}$. Our

data are two orders of magnitude smaller than the values reported in the literature [106], measured with the z-scan method. We tentatively attribute this difference to the fact that our data have been obtained on an epitaxially-grown GaAs/AlAs heterostructure, instead of a GaAs wafer obtained with a different technique.

The three-photon absorption coefficient decreases as a function of wavelength since the summed energy of a pump and probe photon, and therefore the probability of generating an electron hole pair, decreases with increasing wavelength. The three-photon absorption edge is at 2580 nm.

5.7 Conclusion and outlook

We have studied ultrafast all-optical switching of a GaAs/AlAs planar optical microcavity. We demonstrate conditions where the instantaneous electronic Kerr effect prevails over two-photon absorption. Contrary to prior expectations, we find that the electronic Kerr effect is even larger than free carrier effects.

We have demonstrated for the first time switching of a GaAs cavity at telecom wavelengths, using the electronic Kerr effect. Since switching using the electronic Kerr effect is pulse duration limited, switching rates of 10 THz are possible. We demonstrated that for an ultrafast cavity with a moderate storage time of 1 ps, the switching rate would be limited by the cavity storage time. The 1 ps storage time results in a potential switching rate of 1 THz. Our results also open an avenue towards quantum electrodynamical switching of the fastest possible light sources (see e.g. chapter 8) including quantum wells.

In the experiments discussed in this chapter we used a power of 1 μJ/pulse. If we want to switch a micropillar cavity, which has a diameter of 1 μm, we only need a pump spot of the size of 1 μm, instead of the 100 μm we used in this chapter. We conclude that it is possible to switch a micropillar using the Kerr effect with 100 pJ/pulse. Therefore, the Kerr effect is much faster than the free carrier effect, but it needs 10 times more energy per pulse.

Our experimental results are supported by calculations using a dynamic Fabry-Pérot model, which shows a very good agreement with the measurement. With the instantaneous Kerr effect we were able to switch the reflectivity of the resonance at telecom wavelength ultimately fast from 70% to 60% and back at 1 THz rate.

For such an experiment a pump wavelength of 2400 nm or larger is required and a cavity resonance at a wavelength of 1300 nm or larger. The refractive index change is in the order of the required 0.1%. From the switching measurements we extracted the non-degenerate Kerr coefficients over a broad wavelength range. Furthermore we extracted the free carrier three-photon absorption coefficients for three different wavelengths in the near infrared.

CHAPTER 6

Ultrafast optical frequency conversion in a passive transient microcavity [1]

6.1 Introduction

There is a fast growing interest to control and manipulate information encoded as photons, as this promises much broader information bandwidths than with electronic integrated circuits [109]. Therefore, it is important to realize time-dependent control of photonic systems, in other words, photonic switching. Furthermore, it is crucial that two photons can be made to interact, notably that a photon's energy is converted to a different value. As it is well-known that the interaction between two photons is exceedingly weak in free space, one resorts to the well-established methods of nonlinear optics, although these still require elevated field strengths typical of short pulses [110]. Recently, the switching of photonic bandgap crystals and nanophotonic cavities has been advocated to enhance nonlinear optical interactions [2, 81, 111, 112], since these devices permit a judicious tweaking of optical dispersion, considerably enhanced field strengths occur in tiny volumes, and their small footprints make these systems amenable to large-scale integration.

In usual nonlinear frequency conversion [110], a probe pulse is overlapped in space and time with another pulse that is either derived from the probe pulse itself (called self-phase modulation (SPM)) or a light pulse obtained from another source (called cross-phase modulation (XPM)). Typically, the pulses are incident on (semiconductor) crystals

[1] Work done in close collaboration with Philip Harding, Huib Bakker, Allard Mosk and Willem Vos.

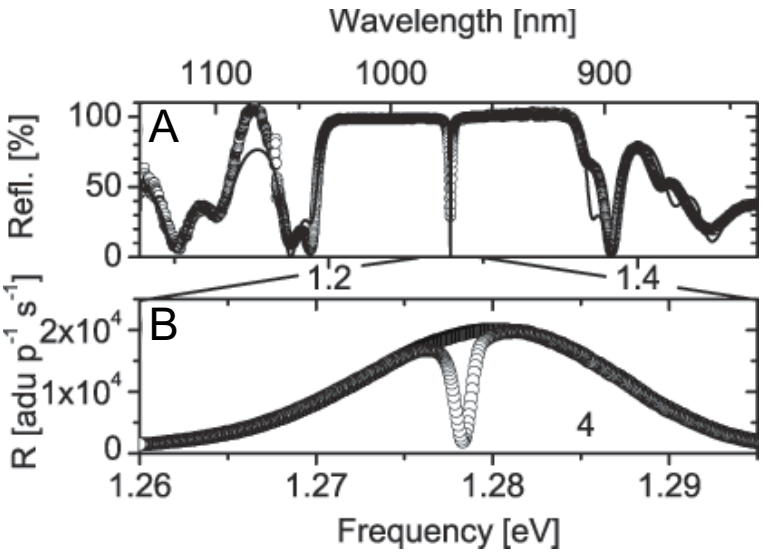

FIGURE 6.1: *(a) Broad-band reflectivity spectrum measured with a white-light source. The reflectivity is calibrated by normalizing to a spectrum of a gold mirror. The trough at 1.278 eV is the cavity resonance, the broad intense peak between 1.192 and 1.376 eV is the photonic stopband of the Bragg mirrors. (b) High-resolution reflectance spectrum measured with the probe laser showing the cavity resonance at 1.278 eV.*

to enhance the photon-photon interactions by second or third order nonlinearities. For the nanophotonic cases, pump-probe overlap is ensured by charging a cavity with probe light *before* the pump pulse arrives, leading to adiabatic light conversion by the cavity resonance [2, 53, 54]. Thus, both cases share a crucial feature, namely that they require a spatiotemporal overlap of the pump and probe pulses. In this paper, we present a novel nonlinear frequency conversion mechanism that does not require pump-probe overlap. Therefore, we have performed a frequency-resolved ultrafast pump-probe study of a semiconductor microcavity. We observe frequency conversion of light *after* the pump pulse has long gone, and identify the mechanisms by which this conversion occurs.

6.2 Experimental

We have studied our planar 980 nm microcavity consisting of a GaAs λ-layer with a thickness $d = 275.1 \pm 0.1$ nm that is sandwiched between two Bragg mirrors made of 12 and 16 pairs of $\lambda/4$-thick layers of nominally pure GaAs or AlAs, see Refs. [13].

A normal-incidence reflectivity spectrum reveals the inhomogeneously broadened cavity resonance at $E_{cav} = 1.278$ eV ($\lambda = 970.2$ nm) centered in the 14.3% wide stopband of the Bragg mirrors, see figure 6.1 A. In separate time-resolved experiments, we have determined the average storage time for photons in the cavity to be $\tau_{cav} = 780 \pm 50$ fs, corresponding to a quality factor $Q = 1500 \pm 100$, and a homogeneous cavity linewidth $\Delta E_{cav} = 0.85$ meV, see chapter 3.

Time-resolved pump-probe spectroscopy was performed on the cavity in reflection geometry [64], see chapter 2. The 140 ± 10 fs duration pump and probe pulses emanate from two independently tunable optical parametric amplifiers. The pump pulses are incident obliquely to avoid scattering into the detection path. The pump frequency was tuned to 0.72 eV ($\lambda = 1720$ nm) to switch the refractive index in all GaAs layers by exciting free carriers by two-photon absorption [104]; the pump is not resonant with the cavity. Our observations were reproduced in runs with the pump tuned to 0.62 eV, 0.56 eV and 0.52 eV in the three-photon regime, see figure 4.2 A. To ensure that only the flat central part of the pump focus is probed, the pump beam had a large Gaussian focus of 113 μm width, much wider than the probe focus of 28 μm. The probe intensity of 1.0 ± 0.3 mJcm^{-2} energy per pulse was kept well below the pump intensity of 30 ± 3 mJcm^{-2}, to prevent inadvertent pumping by the probe pulses. Transient probe reflectivity spectra were resolved with a high spectral resolution of 0.12 meV [(2)]. The probe pulses have a relative spectral bandwidth of 2.7%, from 1.260 to 1.295 eV ($957 < \lambda < 984$ nm), much broader than the cavity's relative linewidth of $1/Q = 0.07\%$, see figure 6.1 B. Therefore, we are able to probe the time-resolved cavity resonance without having to tune the probe. We averaged over probe pulses reflected from pumped and unpumped cavities; the absence of changes in the unswitched resonance confirms that the cavity remains intact during the experiment. Furthermore, the unswitched resonance provides an *in-situ* reference for the switched events.

6.3 Results and discussion

The cavity's time-dependent resonance is presented in a photon energy versus time $(E, \Delta\tau)$-diagram, shown in figure 6.2 A. In such an $(E, \Delta\tau)$-diagram, the "footprint" of photons

[(2)] We used a PI/Acton sp2558 monochromator, and a OMA-V InGaAs diode array with 1024 channels. Due to inadvertent misalignment in the switch experiment, a slant occurred in the raw spectra that was corrected with a straight line, and assuming constant near 100% reflectivity in the stopband (see figure 6.1).

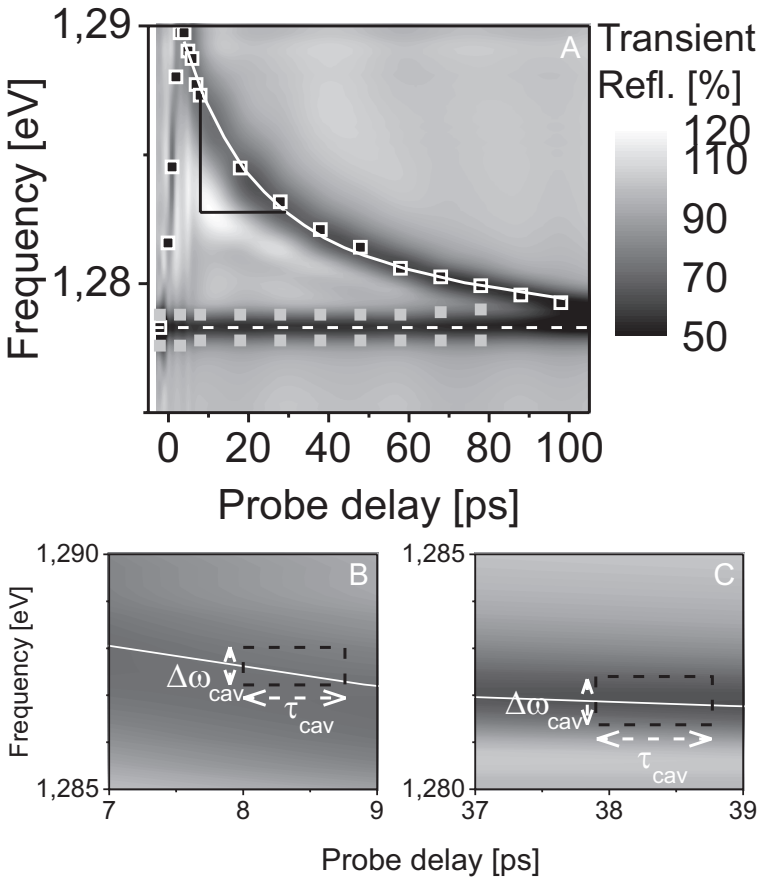

FIGURE 6.2: *(a) Transient reflectivity versus pump-probe delay and probe frequency. The spectra are averaged over both switched and unswitched events. The switched-cavity resonance at select delays is shown by white squares. The white curve is a model of the measured resonances using Drude free-carrier dispersion. (b) and (c) Zoom-in near 8 ps and 38 ps, respectively. The "cavity-photon footprint" (dashed lines) has size ΔE_{cav} by τ_{cav}. The full curve traces the transient cavity resonance whose slope defines the magnitude of light conversion. In (b), the slope is steep compared to the photon footprints, signalling strong light conversion. In (c), the slope is shallow, typical for weak light conversion.*

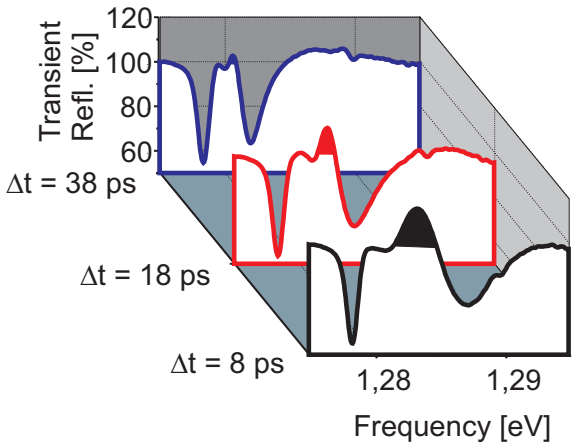

FIGURE 6.3: *Transient reflectivity spectra measured at select pump-probe delays $\Delta\tau$ = 8, 18, 38 ps (cross-sections from figure 6.2).*

stored in the cavity is a rectangle of extent ΔE_{cav} by τ_{cav} (see figure 6.2 B and C), which are inversely related in steady-state: $\Delta E_{cav} = (2\pi\hbar)/\tau_{cav}$. figure 6.2 A shows the transient reflectivity spectrum of the cavity as a function of pump-probe time delay $\Delta\tau$. The transient reflectivity is the time-integrated signal that exits the cavity as a result of a short probe pulse at $\Delta\tau$ (and should not be confused for the instantaneous reflectivity at $\Delta\tau$). The experimental feature at 1.278 eV independent of time is the unswitched cavity. When the cavity is optically switched with a short pump pulse, free carriers are excited leading to an ultrafast reduction of the refractive index. As a result, the cavity resonance frequency rapidly increases within 3 ps from E_{cav} = 1.278 to 1.290 eV, corresponding to as much as 14.5 linewidths ΔE_{cav}, a signal of a strongly modulated cavity. Subsequently, the carriers relax and the refractive index increases with a double-exponential relaxation, see chapter 4.

To investigate the spectral features in more detail, we plot in Figure 6.3 transient reflectivity spectra at selected time delays. The trough at 1.278 eV in all spectra is the resonance of the unswitched cavity. For the switched cavity, we observe that the trough of the transient cavity resonance (E_{cav} = 1.2876 eV at 8 ps) is clearly asymmetric. We attribute this asymmetry to the time-integrating nature of the experiment and the dynamics of the cavity resonance: the field leaking from the cavity is recorded while the resonance is shifting. Strikingly, regions appear in the spectra where the transient reflectivity exceeds 100%, in particular 131% near 1.283 eV and 8 ps (also 122% near 1.282 eV at 18 ps).

This excess transient reflectivity is the result of photons that are stored in the cavity by probe pulses at a delay $\Delta\tau = 8$ ps when the transient cavity resonance is centred at 1.2876 eV. The stored photons are then frequency-converted by 4.5 linewidths to 1.283 eV as a result of the fast downshift of the cavity resonance, and released at a later time $\Delta\tau' = \Delta\tau + \tau_{cav}$. Since the cavity is not resonant with the pump beam, the pump pulses have long vanished at $\Delta\tau = 8$ ps. Therefore, we conclude that this observation represents the first ever frequency conversion of light by the action of a passive optical device - a transient microcavity - *in absence* of a pump pulse.

Returning to figure 6.2, one might naively think that the peak at $E = 1.283$ eV and $\Delta\tau = 8$ ps (vertical solid line) is the result of light being converted adiabatically in the cavity before leaking at a later time $\Delta\tau'$. From figure 6.2, however, one sees that the cavity resonance reaches $E_{\mathrm{cav}} = 1.283$ eV only *much* later, at $\Delta\tau' = 29$ ps (horizontal solid line). This invites the absurd conclusion that light would be trapped during $29 - 8 = 21$ ps or 27 times the cavity storage time τ_{cav}. We conclude that the frequency of trapped photons is not adiabatically converted by the strongly modulated cavity.

We postulate that frequency conversion occurs if the cavity frequency change becomes of the order of one linewidth within a cavity storage time, *viz.*, $dE_{\mathrm{cav}}/dt > \Delta E_{\mathrm{cav}}/\tau_{\mathrm{cav}}$ In the framework of the cavity-photon footprint, we thus expect an effect of the cavity resonance's transient if the resonance crosses the abscissa of the cavity-photon footprint. Indeed, while the footprint reveals a crossing of the cavity's resonance with the abscissa for $\Delta\tau = 8$ ps (figure 6.2 B), the gradient of the dynamic cavity resonance decreases with increasing delay (figure 6.2 C). This agrees with the observation of a strong excess transient reflectivity at $\Delta\tau = 8$ ps and subsiding of the the excess at longer probe delays (figure 6.4).

We are now able to interpret the observed features. Since the instantaneous photon energy is equal to the time derivative of the phase, we consider the phase $\Phi(t)$ of the light trapped in the cavity during the switch $\Phi(t) = -(E_{\mathrm{cav}}(t)/\hbar)t + \Delta\phi(t)$, which can be written as:

$$\Phi(t) = -(E_{\mathrm{cav}}(t)/\hbar)t + \frac{d\Delta\phi(t)}{dt}\Delta t \tag{6.1}$$

Here, $E_{\mathrm{cav}}(t)$ is the time-dependent resonance of the cavity, $\Delta\phi(t)$ the phase change of the light due to the time-dependent refractive index in the cavity, and Δt the duration over which light is frequency converted. In standard nonlinear optics, Δt is equal to the duration of the pump pulse, whereas in our case it is equal to the cavity storage time: $\Delta t =$

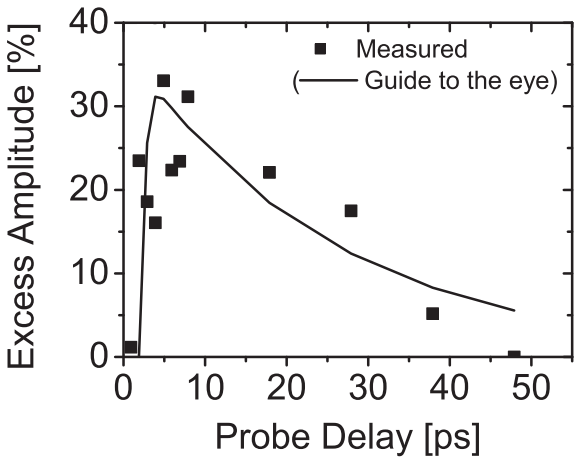

FIGURE 6.4: *Excess amplitude vs. time delay. Squares are our experimental results, and the full curve a guide to the eye. Data calculated with our model are circles and the dashed curve.*

τ_{cav}. Eq. 6.1 reveals that frequency conversion of light in a transient cavity in absence of a pump pulse is due to two effects: The first term is the frequency shifting of the trapped light in sync with the shifting cavity resonance, or adiabatic shifting. However, we have seen above that the trapped photon's frequency shifts more strongly than the adiabatic estimate, which is due to the second term. This term describes how the frequency of the field that circulates in the transient cavity is modulated by the time-derivative of the transient phase, which is proportional to the transient refractive index $n_{\mathrm{cav}}(t)$. Eq. 6.1 reveals that the frequency shift increases with (1) the time duration τ_{switch} over which the light is trapped, (2) the gradient of the cavity resonance's relaxation, (3) the magnitude of the frequency shift of the cavity. In our experiment, the frequency conversion amplitude is large, since the cavity is switched by 14 linewidths (3^{rd} point), and the amplitude is especially large at short positive probe delays where the resonance decays fast (2^{nd} point). Interestingly, with Eq. 6.1 we can also interpret frequency conversion methods that do require spatiotemporal pump-probe overlap [2, 53, 54]: then, the second term will vanish, since Δt is short compared to the cavity dwell time. We propose to call the nonlinear conversion of photon frequency by the action of a transient yet passive cavity "transient cavity phase modulation" (TCPM).

Finally, we discuss several ways to control and apply the TCPM frequency conversion, based on calculations with our model. While switching harder initially increases the

frequency conversion amplitude, the efficiency decreases at even higher pump intensities due to the increasing mismatch of the probe spectrum and the shifted cavity resonance. By matching the probe frequency and bandwidth to those of the switched cavity, the conversion efficiency increases continuously with switching magnitude. Optimized sample growth can provide faster relaxation times in the order of ps [91]. Such a property will increase the conversion efficiency, since the cavity resonance transient will be even steeper compared to the cavity photon footprint. In the present work the trapped photons are red-shifted by the cavity, due to the nature of the switching mechanism, namely free-carrier effects. Conversely, a switch mechanism to blue-shift light requires a decreasing refractive index, for example using heating effects. Finally, we note that TCPM frequency conversion may well be used at the single-photon level, thus opening avenues in quantum optics and quantum information processing.

CHAPTER 7

Addressing single optical resonances of micropillar cavities

7.1 Introduction

In this work we study GaAs/AlAs micropillar cavities because they show a large Purcell effect [11] and they are used for the observation of strong coupling [3]. Micropillar cavities are photonic structures that are typically a few micrometers high with a diameter between 1 μm and 20 μm. Up to now micropillar cavities are extensively studied by probing them from the inside using photoluminescence of quantum dots to determine the frequencies of optical resonances [20]. Here, we identify and interpret single optical resonances of multi-mode micropillar cavities from the outside by performing reflectivity measurements. Probing the resonances in reflectivity is essential for ultrafast switching experiments as have been performed on planar cavities [13] and chapter 6. We show that we can address single modes and show mode profiles of different modes together with their calculated mode profiles. Addressing single modes is interesting for ultrafast switching experiments, but can also be used to select a spatial subset of an ensemble of quantum dots in the pillar. The latter is relevant for determining the distribution of decay rates [40] and chapter 8.

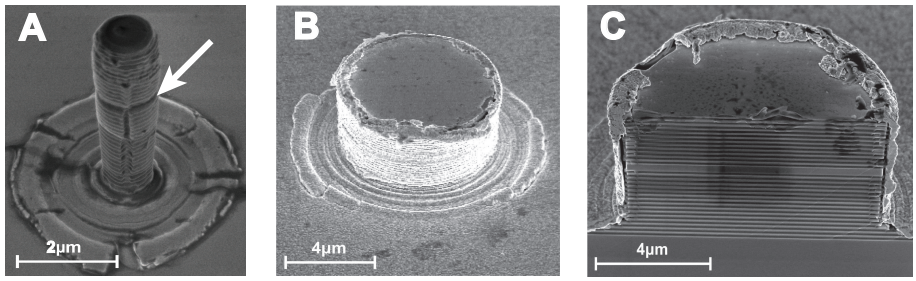

FIGURE 7.1: *(A) SEM image of a micropillar cavity with 1 μm diameter and a height of 5.7 μm. At the pillar edge one can see an alternating light- and dark-gray color pattern associated to the GaAs/AlAs Bragg stack with 13 $\lambda/4$ layer pairs, a GaAs λ cavity layer, and a second Bragg stack with 25 $\lambda/4$ layer pairs. The λ cavity is indicated with a white arrow. (B) SEM image of a pillar with 8 μm diameter. The substrate and the pillar edge are covered with gold. The top facet is clean. The alternating pattern on the edge is associated to the GaAs/AlAs Bragg stack with 12 $\lambda/4$ layer pairs, a GaAs λ cavity layer, and a second Bragg stack with 16 $\lambda/4$ layer pairs. At the base of the pillar a ring pattern is visible. (C) Cross section of a cleaved gold-coated pillar with 8 μm diameter. The GaAs/AlAs Bragg stack with 12 $\lambda/4$ layer pairs, a GaAs λ cavity layer, and a second Bragg stack with 16 $\lambda/4$ layer pairs are clearly visible.*

7.2 Experimental

7.2.1 Sample fabrication

The fabrication process [(1)] of micropillar resonators starts with the growth of a planar microcavity by molecular beam epitaxy on a GaAs substrate, see chapter 2. From the planar cavity, micropillars have been structured by reactive ion etching (RIE) at room temperature. A layer of SiO_x with a thickness between 100 nm and 200 nm is deposited after RIE and protects the AlAs from oxidizing. The deviation of the pillar diameter obtained in the λ cavity layer from the specification is smaller than $\pm 1\%$.

Figure 7.1 A shows a scanning electron micrograph (SEM) of a micropillar cavity with a diameter of 1 μm and a height of 5.7 μm. At the pillar edge one can see an alternating light- and dark-gray color pattern associated to the Bragg stacks. The cavity layer is indicated with a white arrow. A ring pattern, visible at the base of the pillar, is a result of the reactive ion etching step. The ring at the basis of the pillar does not influence the optical measurements, since we focus on the top of the micropillar, and the Rayleigh length of the focus (1 μm) is smaller than the pillar height (5.7 μm). Inhomogeneities on

[(1)] The micropillar cavities were fabricated by Julien Claudon and colleagues in the CEA-CNRS group "Nanophysique et Semiconducteurs" at CEA-CNRS Grenoble lead by Jean-Michel Gérard.

the pillar sides, like the vertical crack on the pillar shown in figure 7.1 A, increase the roughness of the pillar and thereby the scattering losses [113]. The scattering losses will not influence the frequency of cavity resonance but will affect the quality factors of the resonances.

We also studied a sample with gold-coated pillars. The gold coating on the substrate prevents leakage of light through the substrate if the pillars are probed in transmission. Furthermore, the gold coating around the pillar prevents coupling to leaky modes [27]. To fabricate the gold-coated pillars, gold is deposited on a bare pillar sample after reactive ion etching and removed from the top facets of the pillars by focussed ion beam milling using Argon ions. Figure 7.1 B shows an SEM image of a gold-coated pillar with a diameter of 8 μm and a height of 4.3 μm. The substrate and the pillar edge are covered with gold, and the top facet is clean. At the pillar edge one can see the imprint of the multiple Bragg layers and a ring pattern due to the etching step is visible at the base of the pillar. Figure 7.1 C shows a cross section of a cleaved gold-coated pillar with 8 μm diameter. The Bragg stacks and the cavity layer are clearly visible.

Both the gold coated sample and the uncoated sample contain a number of pillar fields consisting of micropillars. The fields are identified using x (1-4) and y (A-E) coordinates (see also figure 7.2).

7.2.2 Optical imaging

Figure 7.3 A shows an image taken with the microscope of a gold-coated pillar with a diameter of 20 μm. The illuminated part of the sample and a micropillar with 20 μm diameter are clearly visible. Even the gold coating can be resolved. Focussed white light from the probe beam is visible in the center of the pillar.

Figure 7.3 B shows a pillar field imaged using a glass microscope objective (Melles Griot 40X) with NA 0.65 and a 100 mm tube lens. Pillars with a diameter between 1 μm and 10 μm are visible. The focussed probe beam on the pillar with a diameter of 4 μm is indicated with a black arrow. The magnification is 2 times smaller than with the 200 mm tube lens, as expected. The images show that pillars with a diameter of 1 μm and larger are successfully located with the setup and that the probe beam is accurately positioned.

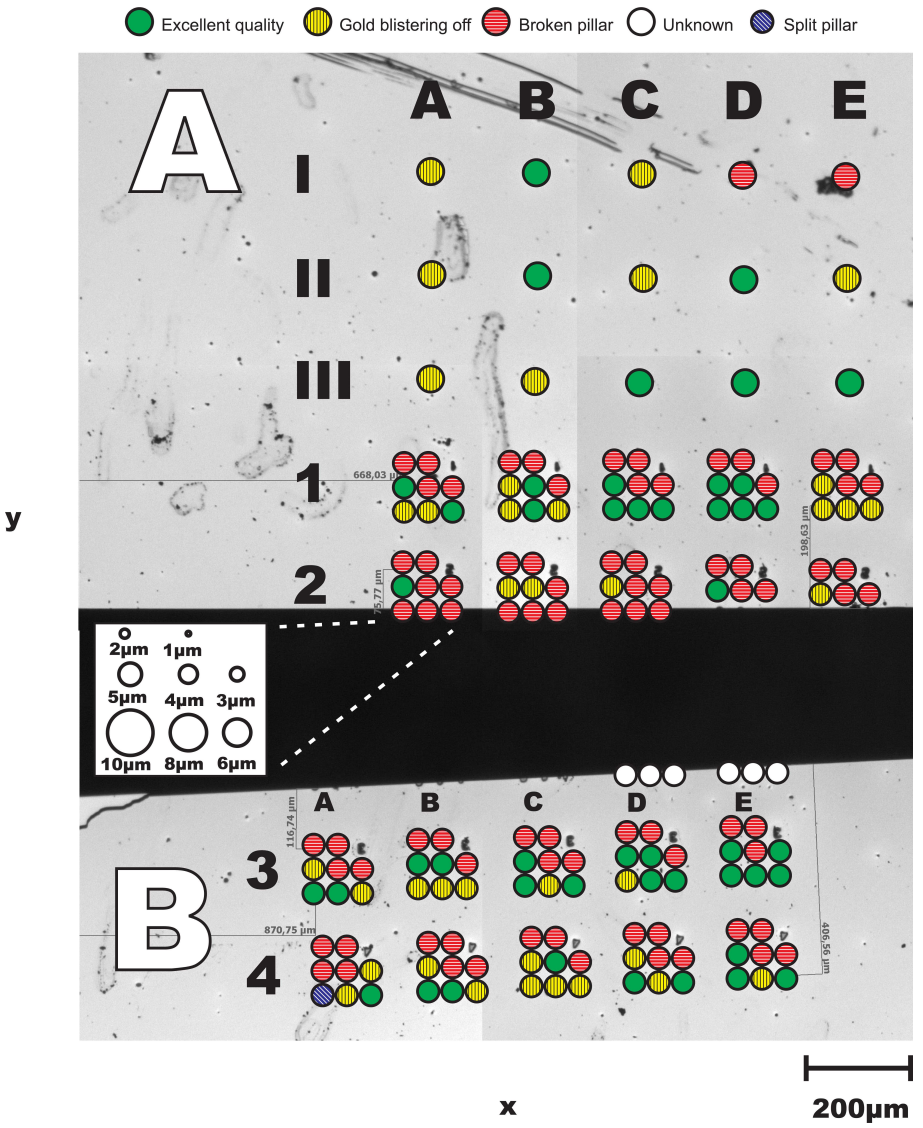

FIGURE 7.2: *Map of a sample containing gold-coated micropillars. Four optical microscope images are merged to create the figure. The upper three rows contain pillars with diameter 20 μm. The fields having 8 circles contain pillars with diameters between 1 μm and 10 μm. A homogeneously filled green circle indicates the position of an "excellent" micropillar. A vertically patterned yellow circle is a "blistered" pillar and a horizontally patterned red circle is a "broken" pillar. The diagonally patterned blue circle indicates a pillar that is cut in half. The status of the pillars located at the six white circles is unknown.*

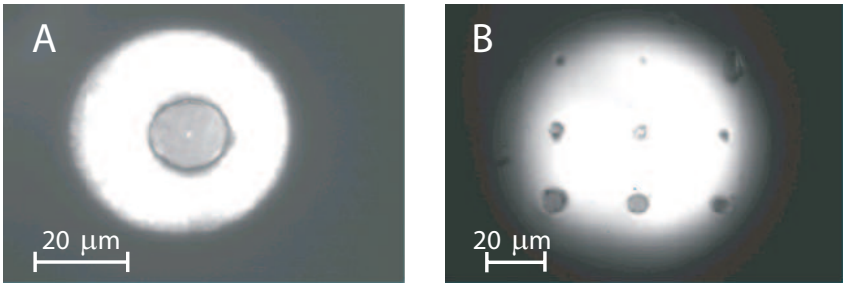

FIGURE 7.3: *(A) Microscope image of a micropillar cavity with 20 μm diameter. The image is made with a microscope consisting of a reflecting microscope objective with NA 0.65 and a 200 mm tube lens. White and black corresponds to a high and low light intensity, respectively. The white circular area is the illuminated part of the sample. The pillar appears as a grey circle with a dark edge. The dark edge corresponds to the gold coating. The white spot in the center of the pillar is focussed white light from the probe beam. (B) Microscope image of a field of pillars using a refracting microscope objective with NA 0.65 and a 100 mm tube lens. Pillars with a diameter between 4 μm and 10 μm and the base of pillars with a diameter of 1 μm and 3 μm are visible. The focussed probe beam impinges on the center pillar with diameter 4 μm.*

7.2.3 Reflectivity measurements

We probe the sample with a broadband white-light source (Fianium SC-450) and analyze the reflected light using an interferometer (Bio-Rad FTS-6000) and a silicon photo diode. The reflectivity of a sample is referenced to a gold mirror in order to account for the spectral response of the setup. Thereby, the reflectivity of the gold mirror is measured before and after each measurement session to take into account slow time-dependent changes in the spectrum of the supercontinuum source. The two resulting spectra are averaged and used for referencing.

7.2.4 Dielectric waveguide theory

In micropillar cavities light is confined in three dimensions, see figure 7.4. In the axial direction, optical confinement is achieved by two Bragg-mirrors facing each other. Transverse optical confinement is achieved by total internal reflection due to a high refractive index contrast at the pillar edges. The calculations we present are based on the decoupling of the axial and transverse wave vector of the resonances in the micropillar cavity [26], as illustrated in figure 7.4 B. The same dependence on time t and the position along the pillar is thereby assumed. The vertical solid curve (A) indicates the intensity distribution of the longitudinal modes, as a result of the axial confinement. The intensity distributions

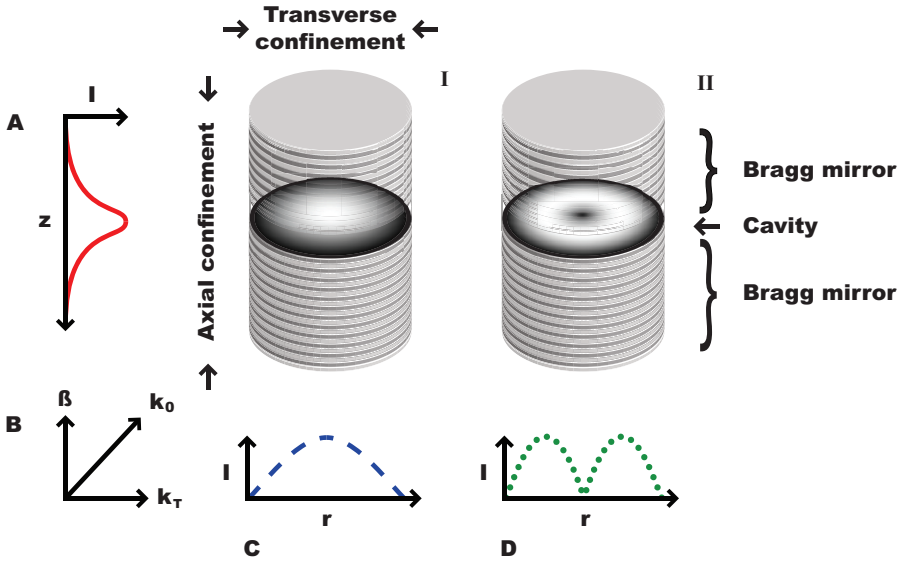

FIGURE 7.4: *Three-dimensional optical confinement in a micropillar cavity. In the axial direction, confinement is achieved by two Bragg-mirrors. Transverse optical confinement is achieved by total internal reflection at the pillar edges. The vertical solid curve (A) represents the intensity distribution of the longitudinal modes, as a result of the axial confinement. The horizontal dashed (C) and dotted (D) curves show transverse intensity distributions of two modes. The corresponding 2D intensity distributions are plotted in perspective in the cavity of the pillars (I and II), where white and black corresponds respectively to a high and low light intensity. The vector diagram (B) relates the wavenumber k_0 outside the pillar to the propagation constant β and the transverse wavenumber k_T.*

can be calculated using the eigenmode model described in Refs. [26, 114]. The horizontal dashed (C) and dotted (D) curves represent the intensity distributions of two distinct transverse modes. The corresponding two-dimensional intensity distributions are plotted in perspective in the cavity of the pillars (I and II). To model longitudinal profile, we approximate the pillar as a homogeneous dielectric waveguide with a cylindrical shape having an effective index of refraction n_{eff} and an air cladding. For a Bragg stack it is known that an effective refractive index can be used to approximate the Bragg condition very well [115, 116]. We assume an effective refractive index since the mode extends into the mirrors. Then, the wavenumber outside the pillar k_0 is related to the propagation

constant β (longitudinal wavevector) and the transverse wavenumber k_T as follows:

$$n_{\text{eff}}^2 k_0^2 = k_T^2 + \beta^2. \tag{7.1}$$

β is determined by the Bragg condition and is therefore fixed by the distance d between the Bragg mirrors and the refractive index of the cavity-layer n_{GaAs}, given by $\beta = 2\pi n_{\text{eff}}/(n_{\text{GaAs}} d)$ [117]. The cavity thickness d and the refractive index n_{GaAs} are obtained from the fit of the transfer matrix calculation to the measured reflectivity spectrum as shown in figure 7.5. The effective refractive index n_{eff} is assumed to be $n_{\text{eff}} = (d_{\text{GaAs}} n_{\text{GaAs}} + d_{\text{AlAs}} n_{\text{AlAs}})/d_{\text{tot}}$, where d_{GaAs} is the total thickness of the GaAs layers, d_{AlAs} is the total thickness of the AlAs layers, n_{GaAs} is the refractive index of GaAs, n_{AlAs} is the refractive index of AlAs, and d_{tot} is the pillar height. Both β and n_{eff} are similar for every mode of every pillar with the same vertical geometry.

By determining the electromagnetic fields of a guided wave that satisfy Maxwell's equations and the boundary conditions imposed by a cylindrical dielectric waveguide with radius r, we obtain the following mode condition [26]:

$$\left(\frac{J_l'(k_T r)}{k_T r J_l(k_T r)} + \frac{K_l'(q_T r)}{q_T r K_l(q_T r)}\right)\left(\frac{n_{\text{eff}}^2 J_l'(k_T r)}{k_T r J_l(k_T r)} + \frac{n_{\text{air}}^2 K_l'(q_T r)}{q_T r K_l(q_T r)}\right) = l^2\left[\left(\frac{1}{k_T r}\right)^2 + \left(\frac{1}{q_T r}\right)^2\right]^2 \left(\frac{\beta}{k_0}\right)^2, \tag{7.2}$$

where J_l are the Bessel functions of the first kind, K_l are the modified Bessel functions of the first kind, q_T is the transverse wavenumber in air, and n_{air} is the refractive index of air. The primes on J_l and K_l refer to differentiation with respect to their arguments. Equation (7.2) has two solutions that are designated as the EH (7.3a) and HE (7.3b) modes

$$\frac{J_{l+1}(k_T r)}{k_T r J_l(k_T r)} = \frac{n_{\text{eff}}^2 + n_{\text{air}}^2}{2n_{\text{eff}}^2} \frac{K_l'(q_T r)}{q_T r K_l(q_T r)} + \left(\frac{l}{(k_T r)^2} - R\right) \tag{7.3a}$$

$$\frac{J_{l-1}(k_T r)}{k_T r J_l(k_T r)} = -\left(\frac{n_{\text{eff}}^2 + n_{\text{air}}^2}{2n_{\text{eff}}^2}\right) \frac{K_l'(q_T r)}{q_T r K_l(q_T r)} + \left(\frac{l}{(k_T r)^2} - R\right), \tag{7.3b}$$

where

$$R = \left[\left(\frac{n_{\text{eff}}^2 - n_{\text{air}}^2}{2n_{\text{eff}}^2}\right)^2 \left(\frac{K_l'(q_T r)}{q_T r K_l(q_T r)}\right)^2 + \left(\frac{l\beta}{n_{\text{eff}} k_0}\right)^2 \left(\frac{1}{k_T^2 r^2} + \frac{1}{q_T^2 r^2}\right)^2\right]^{1/2}. \tag{7.4}$$

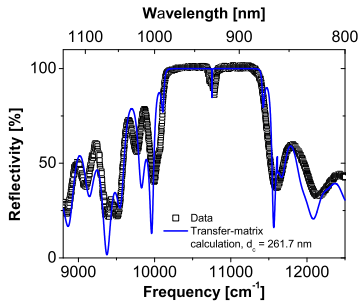

FIGURE 7.5: *Reflectivity spectrum of an uncoated pillar with 20 μm diameter (squares) fitted by a transfer-matrix calculation (line). The stopband extends from 10200 cm^{-1} to 11400 cm^{-1} corresponding to a relative bandwidth of 11.1 %. The resonance of the λ-cavity ($\Delta\omega/\omega_{sb}$ = 0.75%) is visible at ω_{cav} = 10755 cm^{-1}.*

To obtain k_T, Eq. (7.3a) and (7.3b) can be solved graphically by plotting both sides of the equations as a function of $k_T r$, letting $(q_T r)^2 = (n_{\text{eff}}^2 - n_{\text{air}}^2)k_0^2 r^2 - (k_T r)^2$ on the right-hand side. For the special case where $l = 0$, the EH and HE modes correspond to the TE and TM modes of a slab waveguide, respectively.

7.3 Results

7.3.1 General properties of micropillar reflectivity spectra

Figure 7.5 shows the reflectivity spectrum of an uncoated pillar with a diameter of 20 μm. The resonance of the λ-cavity is visible at ω_{cav} = 10755 cm^{-1}. The measured maximum reflectivity R = 101.7% slightly exceeds 100% since the reflected signal was normalized to a gold mirror reflecting 95 %. The maximum possible reflectivity relative to the gold mirror is therefore 105 %.

To determine the thickness of the cavity layer to calculate the propagation constant β, we performed a transfer matrix calculation to fit the reflectivity spectrum of a 20 μm pillar. We assume that the pillar with a diameter of 20 μm can be approximated as an infinite planar cavity, since the focal diameter is 4.2 μm. The transfer-matrix calculation [50] is performed with a GaAs/AlAs Bragg stack with 13 pairs of $\lambda/4$-thick layers, a 261.7 nm thick GaAs λ-layer, and a second Bragg stack with 25 pairs of $\lambda/4$-layers. The thickness of the GaAs layers is 65.4 nm and the thickness of the AlAs layers is 78.3 nm.

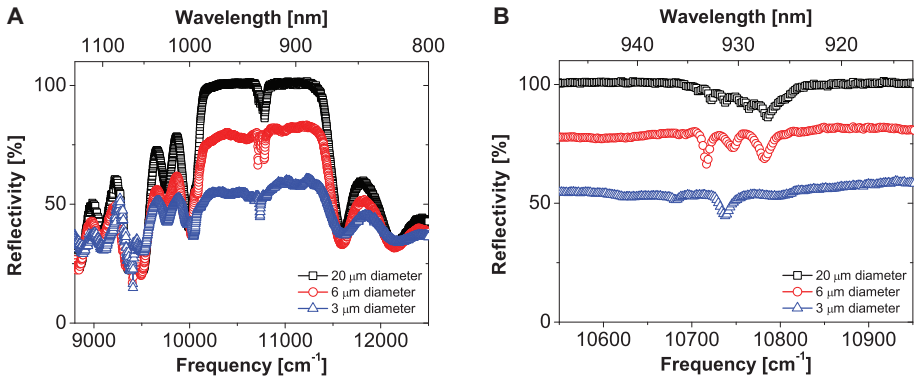

FIGURE 7.6: *(A) Reflectivity spectra of three different micropillar cavities with 20 μm, 6 μm, and 3 μm diameter. The reflectivity of the stopband decreases with decreasing pillar diameter. For pillars with diameter 6 μm and smaller the stopband is not perfectly flat. (B) A zoom-in on the cavity resonances of figure (A). The plots show 7, 3, and 2 troughs (resonances) at the cavity resonance of pillars with 20 μm, 6 μm, and 3 μm, respectively. The total number of resonances decreases, but the resonance spacing increases with decreasing pillar. The cavity resonance of the 20 μm pillar is asymmetric: it is steeper at the blue side than at the red side.*

The calculated spectrum corresponds well to the measured one. The measured features are less pronounced than the calculated ones because the high NA microscope objective broadens the measured spectrum.

Reflectivity spectra of three different micropillar cavities with diameter 20 μm, 6 μm, and 3 μm are shown in figure 7.6 A. The reflectivity of the stopband decreases with decreasing pillar diameter. The reason is that for small pillars the diameter of the probe beam is larger than the pillar diameter, which means that only a fraction of the beam is reflected by the pillar. In addition, small pillars have more losses than large pillars due to optical scattering at the edges [113]. We also observe that for pillars with diameters of 6 μm or less, the stopband is not perfectly flat. Because the modulation of the stopband reproduces among different pillars with the same diameter it is not due to microscopic irregularities or the probe beam position. The exact cause of the modulation of the stopband for smaller pillars remains currently an open question.

The cavity resonances are shown in figure 7.6 B for a more detailed investigation. The figure shows 7, 3, and 2 troughs for pillars with 20 μm, 6 μm, and 3 μm diameter, respectively. This is the first time micropillar resonances are resolved using reflectivity measurements. Until now micropillar resonances have only been observed with photoluminescence measurements. The troughs are attributed to the confinement of electro-

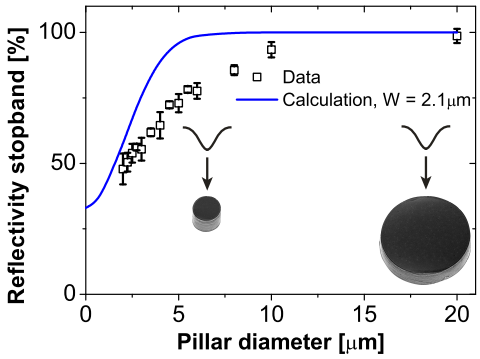

FIGURE 7.7: *Mean reflectivity of the stopband versus micropillar diameter (squares). The distribution bars represent the standard deviation of the mean value. The reflectivity decreases with decreasing pillar diameter. The data is compared to the model presented in Eq. (7.6) (curve) by the power ratio of a Gaussian beam within a circle of radius ρ having a $1/e^2$ beam radius of 2.1 μm. The calculation agrees fairly well with the measurements.*

magnetic radiation in the transverse plane. Each trough is a resonance associated to a mode of the resonator and they have distinct transversal spatial frequencies. The modes are discrete solutions of Maxwell's equations for the boundary conditions of a cylindrical dielectric waveguide, like a micropillar [20]. The identification of single resonances will be discussed in the next section. As shown in figure 7.6 B, the total number of resonances decreases with decreasing pillar diameter as expected [20]. The sum of all cavity resonances of the 20 μm pillar yields a surprisingly asymmetric line profile: it is steeper at the blue side than at the red side. The asymmetry in resonance amplitude is observed both in reflectivity measurements performed with the reflecting objective and in measurements performed with a glass objective. We can therefore exclude the reflecting objective as a cause of the asymmetry. The origin of the asymmetry needs to be investigated further to obtain more insight.

To explain the decreasing reflectivity of the stopband with decreasing micropillar diameter, we have plotted the mean reflectivity of the stopband measured at gold-coated and uncoated pillars versus the pillar diameter in figure 7.7. The reflectivity decreases with decreasing pillar diameter as was seen in figure 7.6 A. The calculated ratio of power carried within a circle of radius r in the transverse plane at position z to the total power of

a Gaussian beam, given by

$$\frac{P_r}{P_{tot}}(r) = 100\%\Big[1 - exp\Big(\frac{-2r^2}{W^2(z)}\Big)\Big], \tag{7.5}$$

where $W(z)$ is the beam radius at distance z from the focus [75]. The part of the beam that does not impinge on the surface of the pillar is reflected by the gold layer, which is not in focus. The background reflection due to the gold layer is found to be 33 %, which means that 33 % of the light not reflected by the pillar is reflected by the gold surface. Only 33 % is reflected by the gold layer, because the layer is not in focus. The model for the stopband reflectivity including background reflectivity to which the data in figure 7.7 are compared, becomes:

$$\frac{P_r}{P_{tot}}(r) = 100\%\Big[1 - 0.67exp\Big(\frac{-2r^2}{W^2(z)}\Big)\Big], \tag{7.6}$$

In figure 7.7 the data are compared to the model with the beam radius of 2.1 μm, measured with a knife edge. Therefore, the model has no free parameters and shows a fairly good agreement with the data. We attribute the difference between the calculation and the measurement for 5 μm and larger pillars to scattering losses at the edges of the pillar due to surface roughness, which has a larger contribution for smaller pillars [113]. The deviation for smaller pillars we attribute to the simplicity of our model.

Figures 7.8 A and B show reflectivity spectra of the cavity resonance for gold-coated micropillar cavities with 5 μm diameter from different pillar fields with the same x-coordinate and for pillars with 6 μm diameter from different pillar fields with the same y-coordinate on the sample, respectively. It is clear that the spectral shapes of the resonances reproduce very well among different pillars of the same diameter. This excellent reproduction is a confirmation of the high reproducibility in the micropillar fabrication. Similar resonances are indicated by a dashed line, showing that in both x- and y-direction on the sample the center frequency of the resonances increases. The resonance frequency increases because there is a spatial gradient in the cavity thickness in both the x and y direction, due to the growth process.

Figure 7.9 shows the mean scaling factor of the frequency axis of reflectivity spectra per pillar field versus the position on the sample. To obtain the scaling factors, the resonance frequency of the most well-pronounced resonance at the cavity resonance of a spectrum is divided by the resonance frequency of the same resonance of a pillar with the

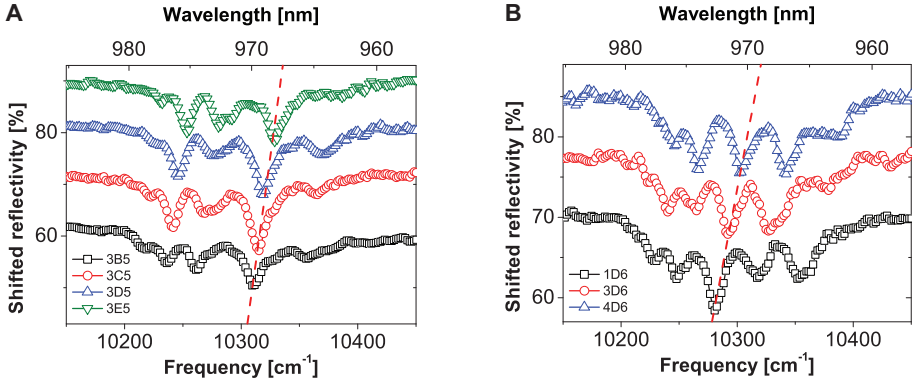

FIGURE 7.8: *High resolution reflectivity spectra of the cavity resonances for gold-coated micropillar cavities with (A) 5 μm diameter from different pillar fields with the same x-coordinate and (B) for pillars with 6 μm diameter from different pillar fields with the same y-coordinate (B). A refracting microscope objective is used for this measurement. The reflectivity axis has been offset with 10 %, only the lowest spectra (squares) in (A) and (B) have not been offset. The resonances reproduce among different pillars of the same diameter. Similar resonances are indicated by a dashed line, showing that in both x- and y-direction on the sample the center frequency of the resonances increases due to spatial gradient in the cavity thickness.*

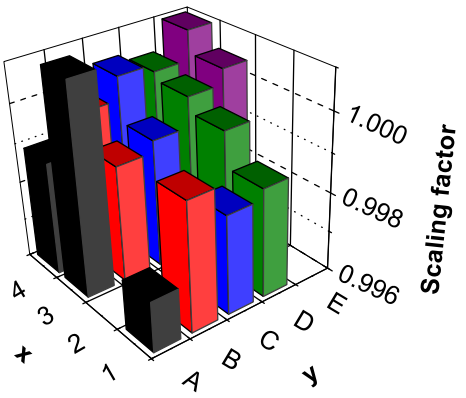

FIGURE 7.9: *Mean scaling factor (f) of the frequency axis of reflectivity spectra per pillar field versus the position. The spectra of each pillar field is scaled to field 3D. The highest mean scaling factor of 1.00094 is found at field 4E and the lowest mean scaling factor of 0.99728 is found at field 1A. A trend is visible in both x- and y-direction. The scaling factor of field 3A does deviates from the trend because it is based on an odd resonance from a single measurement.*

same diameter in field 3D. The reflectivity spectra from pillars in field 3D were used as a reference since they showed the most pronounced and clear troughs. The highest mean scaling factor of 1.00094 is found at field 4E and the lowest scaling factor of 0.99728 is found at field 1A. An increasing trend is visible in both x- and y-direction. The scaling factor of field 3A deviates from the trend because the resonance that is used for calculating this scaling factor has a shape and amplitude that deviates from other spectra.

The resonance frequency ω of a resonance is related to the cavity thickness d, as can be derived from equation (7.1). We attribute the spectral shift $\Delta\omega$ of resonances for different locations on the sample to an inhomogeneously distributed cavity thickness. Therefore, the mean scaling factor f can directly be related to the cavity thickness d: $\Delta\omega/\omega = \Delta d/d = f$. The difference in cavity thickness Δd between extreme fields 4E and 1A is less than 1 nm, assuming that the cavity thickness of field 3D is 261.4 nm, which we obtained from the fit of the transfer matrix calculation to the reflectivity spectrum in figure 7.5. The spatial gradient of the cavity thickness is very small compared to the cavity thickness and allows us to test our model on pillars with different propagation constants. Similarly, in future experiments it allows us to select different ensembles of quantum dots, since quantum dot emission in a resonance at a different frequency, means emission from different size quantum dots and therefore a different ensemble.

7.3.2 Mode identification

Figures 7.10 A shows the reflectivity spectra of pillars with a diameter of 3 μm after scaling of the resonance frequencies. Each resonance is indicated with a circle. The resonances reproduce among different pillars with the same diameter and there is little variation between the scaled center frequencies of the resonances and the pillar position. The resonances are not equidistantly spaced, which agrees with the calculations and reference [20]. With data as in figure 7.10 A we can analyse the origin of the resonances by comparing the scaled positions with the resonance frequencies calculated with the waveguide model.

The reflectivity spectra of uncoated pillars with diameters between 1.25 μm and 3.50 μm are shown in figure 7.10 B. The HE11 and HE01 modes are indicated with bold squares and bold circles. A clear evolution of the resonances is visible: the frequency of a resonance as well as the resonance spacing increases with decreasing pillar diameter. The

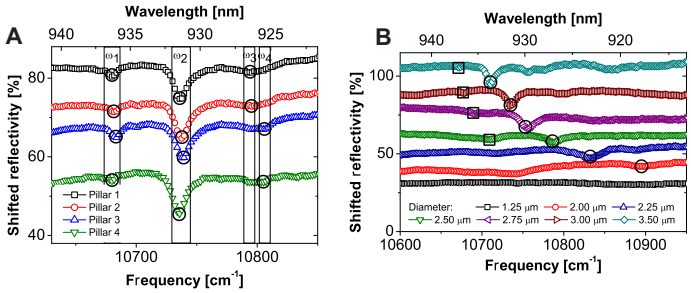

FIGURE 7.10: *Reflectivity spectra of the cavity resonance for uncoated micropillar cavities with (A) 3 μm diameter. The reflectivity axis has been offset with steps of 10% except for the lowest. Each resonance is indicated with a bold circle. The center frequency of the resonances shows little variation among different pillars of the same diameter (within vertical lines). (B) Reflectivity spectra of the cavity resonance for micropillar cavities with diameters between 1.25 μm and 3.5 μm. The reflectivity axis has been offset. Resonances are indicated with bold squares and bold circles. A clear evolution of the resonances is visible: the frequency of a resonance increases with decreasing pillar diameter, as well as the resonance spacing. The reflectivity spectra for pillars with 2 μm diameter and smaller show weakly pronounced resonances or no resonances at all.*

reflectivity spectra for pillars with 2 μm diameter and smaller show weakly pronounced resonances or no resonances at all since the signal level is low.

Figure 7.11 shows the measured and calculated resonance frequencies versus micropillar diameter for uncoated micropillars. The resonance frequencies of the modes decreases with increasing pillar diameter and more resonances appear as the pillar diameter increases. We see a very good agreement between the measurement and the calculation. We can assign to each resonance a label using the standard notation for guided modes as used in dielectric waveguides [26]. The solid line, labeled with HE11, represents the fundamental mode. With figure 7.11 we can identify the resonances.

The resonance frequency of a mode decreases with increasing pillar diameter. The resonances converge to a horizontal asymptote at $\omega = 10650\ cm^{-1}$ on the abscissa, which is the frequency of the propagation vector β in air. Using a cavity thickness d=261.7 nm from the transfer matrix calculation of a pillar with 20 μm diameter, we calculated the frequency of β to be 10722 cm^{-1}. We used a micropillar with a diameter of 20 μm since it approaches the planar case for our focus diameter of 2.1 μm. We attribute the difference between the experimentally found and calculated β to the spatial gradient in the cavity thickness, since the 20 μm pillar from which we derived β experimentally is at a different

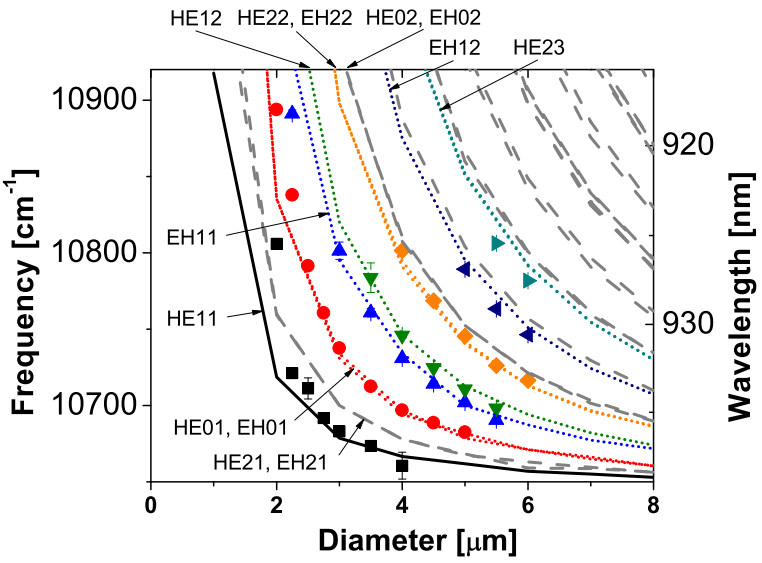

FIGURE 7.11: *Measured (symbols) resonance frequency and calculated (lines) mode frequency versus micropillar diameter for the uncoated micropillars. The agreement between the calculation and the reflectivity measurements is very good. The resonance frequency of a mode decreases with increasing pillar diameter. The modes converge to a horizontal asymptote ($\omega = 10650\ cm^{-1}$). The modes are labeled after the standard name of their guided modes as used in optical fibers [26]. The solid line, labeled with HE_{11}, represents the fundamental mode. The dotted lines indicate the calculations of the other modes we have observed in reflectivity. Modes indicated by a dashed line are not observed in reflectivity.*

location on the pillar sample. With figure 7.11 we can identify the resonances and we can continue the investigation of the mode profiles and how to address single modes.

7.3.3 Addressing single mode

To investigate the position dependent coupling to the resonances, we varied the transverse position of the probe beam while keeping the top facet in focus. In this way we probe the mode profile of the resonance, which shows a spatial dependent field distribution. What profile the resonances have can be derived using the labeling of the modes from figure 7.11.

The amplitude of a resonance equal to the difference between the stopband reflectivity and the reflectivity of a resonance is plotted versus position in figures 7.12 A (HE11 mode) and B (HE01 mode) for a micropillar with a diameter of 6 μm. Figures 7.12 A and B show that the amplitudes of the resonances strongly depend on position. It is clear that the

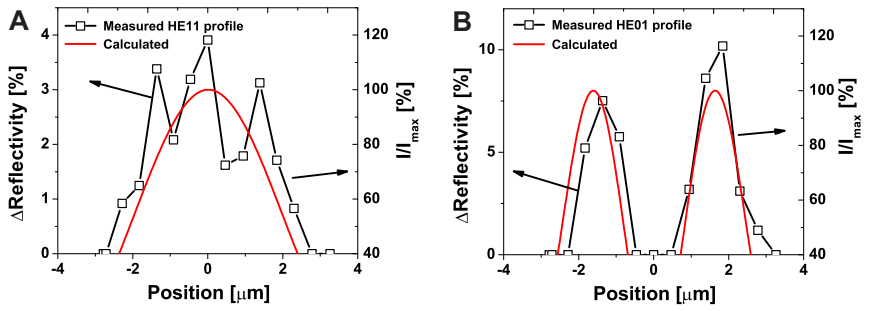

FIGURE 7.12: *(A) Measured (symbols) and calculated (line) modeprofile of the fundamental HE11 mode for a 6 μm pillar. (B) Measured (symbols) and calculated (line) modeprofile of the HE01 mode for a 6 μm pillar. mode*

shown modes have symmetrical profiles. Figures 7.12 A and B show that the measured mode profile agrees very well with the mode profile calculated with the waveguide model. The HE11 mode shows one maximum as expected, the HE01 shows two. From figures 7.12 A and B it is clear that we can excite the HE11 mode at the zero position without exciting the HE01 mode. In a micropillar with a diameter of 2 μm the HE11 and HE01 mode are the only ones present, which means that in these pillars it is possible to address a single mode in reflectivity. For larger pillars more modes are present and a more extensive scheme is needed to address single modes: not only do we need to excite at the antinode of a mode, but also at the right frequency.

7.3.4 Resonance characteristics versus micropillar diameter

Figure 7.13 shows the number of resonances versus micropillar diameter obtained from our reflectivity measurements, and from calculations. For both measurements and calculations the number of resonances increase with increasing pillar diameter. The calculated number of modes is larger than the measured number of resonances. Due to the difference in field symmetry between optical resonances and the probe beam it is not possible to couple to all resonances. The intensity of the probe beam is Gaussian and the beam is linearly polarized, while this is not the case in general for the mode profiles.

Figure 7.14 shows the quality factor Q versus micropillar diameter for reflectivity measurements and photoluminescence. The quality factor was determined from the in-

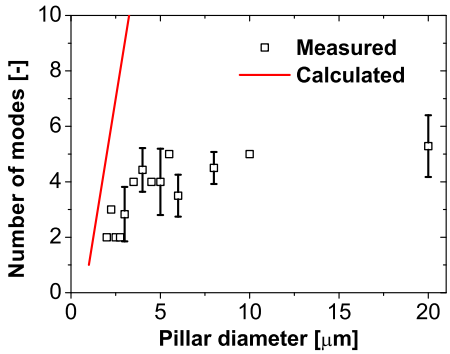

FIGURE 7.13: *Number of resonances versus micropillar diameter for reflectivity (squares) and photoluminescence (circles) measurements on uncoated micropillars and for calculations (line). For both the measurements and calculations the number of resonances increase with increasing pillar diameter. The calculated number of modes is larger than the number of resonances observed in the measurements.*

verse of the relative linewidth of the HE01 mode. Q decreases with decreasing pillar diameter, due to additional losses caused by optical scattering on the edges [113].

We have compared the experimental quality factor with a model from literature [113]

$$Q = \frac{rQ_\infty}{r + \eta_Q Q_\infty J_0^2(k_T r)}, \tag{7.7}$$

where r is the radius of the pillar, Q_∞ the quality factor for a pillar with an infinite radius (i.e., a planar microcavity), η_Q is a measure for the efficiency of the scattering at the edges,

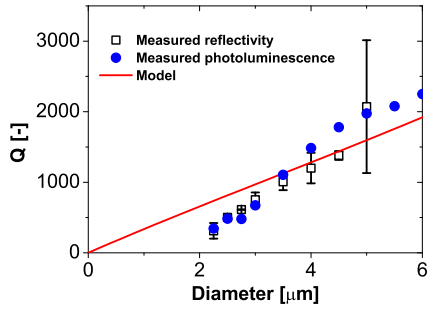

FIGURE 7.14: *Quality factor Q of the HE01 mode versus micropillar diameter for reflectivity (squares) measurements. Q increases with increasing pillar diameter.*

and the Bessel function term $J_0^2(k_T r)$ is a measure for the amplitude of the field at the edge of the pillar, which is assumed to be a measure for the amount of scattering. The fit of Eq.7.7 is shown in figure 7.14 with $Q_\infty = 10000$, $\eta_Q = 1.44 \times 10^{-3}$. A fixed parameter is $k_T = 0.24\ rad/\mu m$, which we calculated using the waveguide model. The values for Q_∞ and η_Q agree well with literature values [113].

The solid circles in figure 7.14 shows the value for the quality factor as found in photoluminescence measurements at room temperature, at lower temperatures the quality factor increases [(2)]. There is a very good agreement between the quality factor measured in reflectivity and with photoluminescence.

7.4 Conclusion

We have shown that we could spatially resolve mode profiles and address single modes in multi-mode micropillars by scanning the probe beam over the pillar surface. In this way we obtained modeprofiles that match the calculated modeprofiles.

We have probed and spectrally resolved optical resonances from outside the pillars. The number of resonances decreases with decreasing pillar diameter. The resonance frequency shifts with the sample location due to an inhomogeneous cavity thickness distribution.

We have identified modes by comparing experimental resonance frequencies with the calculated ones. The agreement between the waveguide model and the reflectivity measurements is very good. The calculated number of modes is larger than the measured number of resonances, from which we conclude that external Gaussian beams can not couple to all resonances, because of the difference in field symmetry between resonances and the probe beam.

The number of modes decreases with diameter as expected from waveguide theory. The quality factor Q of a resonance decreases with decreasing pillar diameter due to scattering losses [113]. We found good agreement between the measured and calculated quality factor.

We have demonstrated the optical characterization of micropillar cavities with diameters between 2 μm and 20 μm using reflectivity measurements. The reflectivity measurements agreed very well with the transfer matrix calculation.

[(2)] J. Claudon and J.M. Gérard, private communication

CHAPTER 8

Switching the decay rate of an emitter inside a cavity

8.1 Introduction

Light is essential for myriad processes around us: in nature, to human life, and to technological applications and everyday appliances. It is known that an elementary light source such as an atom emits a photon either spontaneously or stimulated by an external field [35]. It is also well-known that the rate of spontaneous emission is not an immutable property of an atom [36, 37]. The rate also strongly depends on its surroundings. In quantum mechanics, the rate of spontaneous emission of an excited two-level atom is described by Fermi's golden rule [38]: the rate is determined by a product of atomic matrix elements of the dipole operator with the local density of optical states (LDOS), that typifies the surroundings. The LDOS is thereby a measure of the number of modes in which a photon can be emitted, and it can be interpreted as the density of vacuum fluctuations at the atom's position. A main feature of spontaneous emission is its dynamics: an emitted photon is measured at a random time after the atom is excited with a short pulse. Both the distributions of emitted photons and of the excited-state population decay exponentially in time, and are determined by the decay rate.

To modify the average spontaneous emission rate of a source in the frequency domain a resonant cavity can be tuned to the source's emission frequency. In this way much progress has been made in controlling spontaneous emission with nanophotonic structures [11, 119, 123]. In all microcavities and photonic crystals, however, the control is

stationary in time. Thus, the distribution of emitted photons and the emission rate do not change in time.

In this work, we propose a novel tool to quickly modify the environment of an ensemble of two-level sources during their lifetime. As a result, we anticipate deterministic bursts of dramatically enhanced (or inhibited) emission within short intervals. Our approach is a novel tool to control excited two-level quantum sources and opens new vistas: We envision a bright ultrafast light source whose statistics differs from known laser action (Q-switching or cavity dumping). We also imagine novel control of quantum information against decoherence. In the long run, our method offers a novel tool to realize the breakdown of the weak-coupling approximation and non-Markovian dynamics in cavity quantum electrodynamics.

Here, we introduce the general equation that describes the population density of an ensemble of two-level sources with a time dependent decay rate due to a time dependent local density of states. With this equation we derive the emitted intensity as a function of time for continuous wave and pulsed excitation of an ensemble of two-level sources. The decay rate of the ensemble is determined by a local density of states that is switched using free carriers. This switching mechanism is well studied in literature [13, 24, 94, 96, 102]. Finally, we will show that the derived equations apply to an ensemble of quantum dots in the cavity of micropillar resonators.

8.2 Switching the decay rate

8.2.1 Rate equations

We consider an ensemble of two-level sources (such as an ensemble of quantum dots) in a medium with a local density of optical states (LDOS) ρ that is spectrally shaped by, for example, a photonic microcavity. We investigate what happens if the LDOS changes in time by generating free carriers as described in this thesis, thereby changing the radiative decay rate and the decay dynamics of the ensemble of two-level sources.

To derive the rate equation of an ensemble of two-level sources we start with the equation of motion of the probability amplitude of the excited two-level source (TLS) c_a [39]

$$\frac{dc_a(t)}{dt} = -\frac{d^2}{2\hbar\epsilon_0}\int_0^t\int_0^\infty c_a(t')\omega\rho(\omega, \mathbf{e}_d, \mathbf{r}, t')e^{i(\omega-\omega_d)(t'-t)}d\omega dt', \tag{8.1}$$

with d the amplitude of the transition dipole moment, $\hbar$ the reduced Planck's constant, ϵ_0 the dielectric constant of vacuum, ρ the local density of states, $\mathbf{e}_d$ the transition dipole orientation, $\mathbf{r}$ the dipole position, and ω_d the dipole frequency. For notational convenience, we explicitly write only the time dependency of c_a, but it should be kept in mind that c_a also depends on $\mathbf{r}$ and $\mathbf{e}_d$.

We are in the weak coupling limit if we assume that the product $\omega\rho$ varies very little over the linewidth of the emitter. This approximation is also known as the *Markov approximation* [6] or the *Weisskopf-Wigner approximation* [35]. Using the Markov approximation Eq. 8.1 can be simplified to

$$\frac{dc_a(t)}{dt} = -\frac{d^2}{2\hbar\epsilon_0}\int_0^t c_a(t')\pi\delta(t-t')\omega_d\rho(\omega_d,\mathbf{e}_d,\mathbf{r},t')dt'. \tag{8.2}$$

The integral in Eq. 8.2 can be solved [39]:

$$\frac{dc_a(t)}{dt} = -\frac{d^2}{2\hbar\epsilon_0}c_a(t)\pi\omega_d\rho(\omega_d,\mathbf{e}_d,\mathbf{r},t), \tag{8.3}$$

which can be written as

$$\frac{dc_a(t)}{dt} = -\frac{\gamma_{rad}}{2}c_a(t), \tag{8.4}$$

with $\gamma_{rad}(t) = \frac{d^2\omega_d}{\hbar\epsilon_0\pi}\rho(\omega_d,\mathbf{e}_d,\mathbf{r},t)$, which is well known as Fermi's golden rule [38]. Fermi's golden rule holds in the weak coupling limit, which means that coherence effects of the emitter such as dephasing do not play a role. Equation 8.4 shows that in the case of a time-independent LDOS, $c_a(t)$ decreases exponentially with a decay rate $\frac{\gamma_{rad}}{2}$. It follows from Eq. 8.4 that the probability $|c_a|^2$ of a TLS to be excited decreases exponentially with a decay rate γ_{rad} according to

$$|c_a(t)|^2 = |c_a(t=0)|^2 e^{-\gamma_{rad}t}. \tag{8.5}$$

With Eq. 8.4 the population density $N_2(t)$ of an ensemble of N equal (no inhomogeneous broadening) and non-interacting two-level sources is given by

$$\frac{dN_2(t)}{dt} = -\left(\Gamma_{rad}(t) + \Gamma_{nrad}(t)\right)N_2(t), \tag{8.6}$$

with the radiative decay rate of the ensemble $\Gamma_{rad}(t) = \frac{d^2\omega_d}{\hbar\epsilon_0\pi}\rho(\omega_d,\mathbf{e}_d,\mathbf{r},t)$ and the non-radiative decay rate $\Gamma_{nrad}(t)$. We have introduced the non-radiative decay rate since it

plays an important role in physical time-resolved emission experiments. For convenience we will continue writing N_2 only as function of time t as in Eq. 8.6. For any sub-ensemble of the N two-level sources N_2 also depends on $\mathbf{r}$, ω_d, and $\mathbf{e}_d$. In the derivation of Eq. 8.6 we have neglected contributions from the excitation of the TLS [19]. If we insert these contributions, Eq. 8.6 becomes [19]

$$\frac{dN_2(t)}{dt} = \eta_{abs}\frac{P_{exc}(t)}{\hbar\omega_{exc}} - (\Gamma_{rad}(t) + \Gamma_{nrad}(t))\,N_2(t), \tag{8.7}$$

with $P_{exc}(t)$ the excitation power, ω_{exc} the excitation frequency, and η_{abs} the absorption efficiency. The general solution of Eq. 8.7 is

$$N_2(t) = N_{20} + \int_0^t \left(\eta_{abs}\frac{P_{exc}(t')}{\hbar\omega_{exc}} - (\Gamma_{rad}(t') + \Gamma_{nrad}(t'))\,N_2(t')\right)dt', \tag{8.8}$$

where N_{20} is the population density at t=0. We can calculate the radiated emission I_{em} from the time-derivative of the population density with [40]

$$I_{em} = -\frac{dN_2(t)}{dt} = \Gamma_{rad}(t)N_2(t), \tag{8.9}$$

which means that the emitted light intensity is proportional to the decay rate and the population density. Eq. 8.8 is the general solution for the population density N_2 of an ensemble of two-level sources with a time dependent decay rate. Eq. 8.8 and Eq. 8.9 form the basis for the further discussion in which the equations will be used to numerically calculate the emission in the case of continuous wave excitation and to analytically calculate the emission in case of pulsed excitation.

8.2.2 Direct excitation and free carrier excitation

In this section we focus on the excitation of the emitters, described by the term $P_{exc}(t)$ of Eq. 8.8. There are two main contributions to the excitation power. The first one results from the excitation pulse, which excites the ensemble of two-level sources. The time behavior of the excitation pulse is thereby conveniently modeled with a Gaussian function, see Ref. [55]. The second contribution results from the recombination of excitons created by the switch pulse. This contribution is assumed to be proportional to the free carrier density and therefore has the same temporal behavior as the free carrier density. The total

excitation power is thus given by:

$$P_{exc}(t) = P_{0exc} e^{\frac{-2(t-t_{0exc})^2}{\tau_{exc}^2}} + \frac{P_{0pu}}{\tau_{pu}} \sqrt{\frac{2}{\pi}} \eta_{rec} e^{\frac{-(t-t_{0pu})}{\tau_{rec}}} \int_0^t e^{\frac{-2(t'-t_{0pu})^2}{\tau_{pu}^2}} dt'. \tag{8.10}$$

Here P_{0exc} is the amplitude of the excitation pulse, t_{0exc} the time at which the excitation pulse excites the quantum dots, τ_{exc} the duration of the excitation pulse, P_{pu} the amplitude of the pump pulse, η_{rec} the fraction of the carriers that will recombine at the quantum dots, t_{0pu} the moment the photonic structure is pumped, τ_{pu} the duration of the pump pulse, and τ_{rec} the recombination time of the carriers. The full width at half maximum of the pump pulse is given by $\tau_{puFWHM} = \frac{1}{\sqrt{2ln2}} \tau_{pu}$. We have assumed in Eq. 8.10 that the recombination is slower than the pump process: $\tau_{pu} << \tau_{rec}$, which is usually the case in our experiments where the pump pulse duration is $\tau_{pu} = 0.120$ ps and the recombination time of carriers in GaAs is $\tau_{rec} = 35$ ps [13].

Solving the integral in Eq. 8.10 yields

$$P_{exc}(t) = P_{0exc} e^{\frac{-2(t-t_{0exc})^2}{\tau_{exc}^2}} + P_{0pu} \frac{\eta_{rec}}{2} e^{\frac{-(t-t_{0pu})}{\tau_{rec}}} \left[1 + erf\left(\frac{\sqrt{2}(t-t_{0pu})}{\tau_{pu}} \right) \right], \tag{8.11}$$

where *erf(x)* is the Gaussian error function. The excitation power as a function of time is plotted in figure 8.1. Figure 8.1 shows the direct quantum dot excitation at 5 ps and the start of the quantum dot excitation due to free carriers at the moment the pump pulse arrives at 10 ps. The size of the excitation due to free carriers is taken to be $P_{0pu} \frac{\eta_{rec}}{2} = 10\%$ of the amplitude of the direct excitation pulse. The figure shows that the excitation power due to free carrier recombination decreases with a typical time constant $\tau_{rec} = 35ps$.

The factor η_{rec} can be decreased by shielding the quantum dots with intermediate layers[(1)]. The intermediate layers act as recombination surfaces preventing the electron hole pairs from reaching the quantum dots and use them as recombination centers instead.

After the quantum dots are excited they will decay. The rate at which they decay is time dependent, due to the relaxation of the excited free carriers. This will be the subject of the next section.

[(1)] J.M. Gérard and J. Claudon, private communication

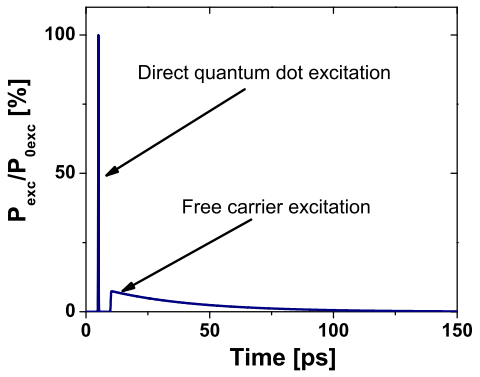

FIGURE 8.1: *Excitation power of the quantum dots normalized to the amplitude of the direct excitation pulse as a function of time for an excitation pulse with duration of 0.110 ps at the time t_{0exc}. The excitation due to free carrier recombination starts at $t_{0pu} = 10$ ps, the moment that free carriers are generated.*

8.2.3 Radiative decay rate as a function of time

The central goal of this work is to describe the time-dependent radiative decay rate $\Gamma_{rad}(t)$ being switched by changing the LDOS at the position of the quantum dots. The LDOS depends nonlinearly on the refractive index, while the refractive index depends nonlinearly on the carrier density. The largest nonlinearity is in the refractive index dependence of the LDOS, the free-carrier dependence of the refractive index can well be approximated by a linear relation (see [13]). For simplicity we assume that the LDOS depends linear on the free carrier density during the switch even though in real systems the situation is more complex (see [13] and chapter 4 and chapter 5). The recombination of the generated free carriers is exponential in time [13, 46, 47] and therefore we model the LDOS change as being exponential. Since in the weak coupling limit Γ_{rad} is proportional to the LDOS, the decay rate is given by:

$$\Gamma_{rad}(t) = \Gamma_{0rad} + \frac{\Delta\Gamma_{srad}}{2} e^{\frac{-(t-t_{0pu})}{\tau_{rec}}} \left[1 + erf\left(\frac{\sqrt{2}(t-t_{0pu})}{\tau_{pu}}\right)\right], \tag{8.12}$$

where $\Gamma_{0rad} = \frac{2\pi d^2 \omega_d}{\hbar\epsilon_0}\rho_0$ is the unswitched decay rate and $\Delta\Gamma_{srad} = \frac{2\pi d^2 \omega_d}{\hbar\epsilon_0}\Delta\rho$ is the magnitude of the switch. We have again made the reasonable assumption that the pulse duration $\tau_{pu} = 0.120$ ps is very short compared to the free carrier recombination time $\tau_{rec} = 35$

ps [59]. With the decay rate given in Eq. 8.12 we can state that the simplification from Eq. 8.2 to Eq. 8.3 is valid if $\omega_d \tau_{pu} >> 1$, which is the case for a pump-pulse duration $\tau_{pu} = 0.120$ ps. In this case the smallest variation of the LDOS in time has a characteristic time that is much longer than the width of the delta function in Eq. 8.2.

The radiative decay rate as a function of time is plotted in figure 8.2. Figure 8.2 shows

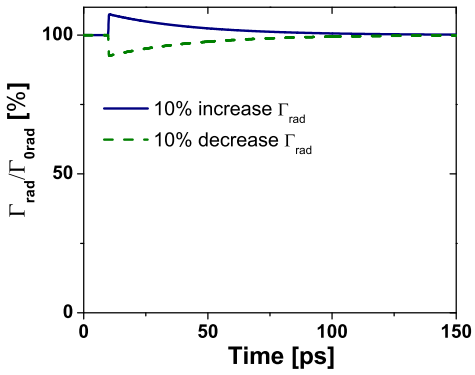

FIGURE 8.2: *Radiative decay rate as a function of time normalized to the initial radiative decay rate in the case the radiative decay rate is increased (solid) and decreased (dashed).*

an increase of 10 % (solid) and decrease of 10 %(dashed) of the decay rate at $t = 10ps$. We chose 10 % for illustrational purposes. Experimentally the change in decay turns out to be bigger [11]. The decay rate is assumed to be proportional to the free carrier density and therefore exponentially decreases with the same time constant as the free carrier recombination time.

8.2.4 General equation for population density

In this section the general equation, including the parameters $P_{exc}(t)$ and Γ_{rad} describing the population density of the ensemble of two-level sources will be given. Substituting

Eq. 8.12 and Eq. 8.11 into Eq. 8.8 yields

$$N_2(t) = N_{02} + \frac{\eta_{abs}}{\hbar\omega_{exc}} \int_0^t \left(P_{0exc} e^{\frac{-2(t'-t_{0exc})^2}{\tau_{exc}^2}} + P_{0pu} \frac{\eta_{rec}}{2} e^{\frac{-(t'-t_{0pu})}{\tau_{rec}}} \left[1 + erf\left(\frac{\sqrt{2}(t'-t_{0pu})}{\tau_{pu}} \right) \right] \right) dt' \tag{8.13}$$

$$- \int_0^t \left(\Gamma_{0rad} + \frac{\Delta\Gamma_{srad}}{2} e^{\frac{-(t''-t_{0pu})}{\tau_{rec}}} \left[1 + erf\left(\frac{\sqrt{2}(t''-t_{0pu})}{\tau_{pu}} \right) \right] + \Gamma_{nrad}(t'') \right) N_2(t'') dt'',$$

which is the general equation for the population density. We used two time arguments *t'* and *t"* for clarity. The equation has three terms: the first is the initial population density N_{02}, the second represents the excitation term, and the third is the emission term.

8.2.5 Population and emission dynamics for continuous wave excitation

In the case of continuous wave (CW) excitation of the two-level sources the direct excitation is constant and equal to P_{0exc}. Therefore, Eq. 8.13 simplifies to:

$$N_2(t) = N_0 + \frac{\eta_{abs} P_{0exc} t}{\hbar\omega_{exc}} + \frac{\eta_{abs}}{\hbar\omega_{exc}} \int_0^t \left(P_{0pu} \frac{\eta_{rec}}{2} e^{\frac{-(t'-t_{0pu})}{\tau_{rec}}} \left[1 + erf\left(\frac{\sqrt{2}(t'-t_{0pu})}{\tau_{pu}} \right) \right] \right) dt' \tag{8.14}$$

$$- \int_0^t \left(\Gamma_{0rad} + \frac{\Delta\Gamma_{srad}}{2} e^{\frac{-(t''-t_{0pu})}{\tau_{rec}}} \left[1 + erf\left(\frac{\sqrt{2}(t''-t_{0pu})}{\tau_{pu}} \right) \right] + \Gamma_{nrad}(t'') \right) N_2(t'') dt''.$$

Since Eq. 8.14 cannot be solved analytically, we have solved it numerically and plotted the results in figure 8.3. Figure 8.3 A shows the influence of the switch and the carrier recombination on the emission dynamics. In the switched case we have chosen $\Gamma_{rad} = 5\Gamma_{tot}$ and $\eta_{rec} = 0$, since a 5 fold Purcell enhancement was reported in literature [11]. In the first 100 ps after the switch at $t = 0$, we see an increase of the emission from 100 % to 600 %. After the excited free carriers have recombined (at $t = 200$ ps), the emission decreases and drops below the unswitched emission. After about 600 ps the emission increases again to the unswitched steady state emission as the carriers recombine. The emission becomes smaller than the unswitched emission because the population density decreases rapidly due to the increased decay rate as is shown in figure 8.3 B. The equilib-

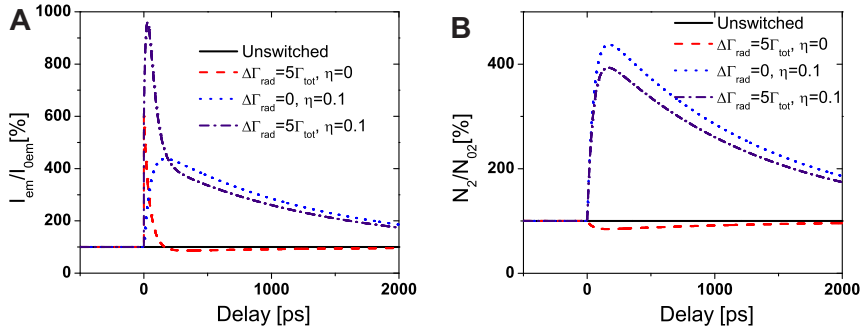

FIGURE 8.3: *Emitted intensity (A) and population density (B) as a function of time for a CW-excited ensemble of two-level sources. The unswitched (solid and dotted) and switched (at t=0 ps, dashed and dash dotted) solutions are plotted with (dotted and dash dotted) and without (solid and dashed) extra excitation of the ensemble due to free carrier recombination at the two-level sources with* $\eta_{rec} = 0.1$. *The dotted curve shows the influence of the recombination in case of a switch, while the dashed curve shows the influence of the change in decay rate. The dash-dotted line is the sum of the dashed and dotted line.*

rium population density cannot be restored instantaneously and therefore the population density drops below the density of the unswitched emission.

To analyse the effect of quantum dot excitation by the free carrier recombination we compare the case of $\Gamma_{rad} = 5\Gamma_{tot}$ and $\eta_{rec} = 0.1$, to the case $\Gamma_{rad} = 0$ and $\eta_{rec} = 0.1$. We see that the emission for the increased decay rate increases at first, and ends up lower than the emission in the case of only excitation by recombination ($\Gamma_{rad} = 0$ and $\eta_{rec} = 0.1$). The emission increases with respect to the case of $\Gamma_{rad} = 5\Gamma_{tot}$ and $\eta_{rec} = 0$ as well, since extra excitons are generated in the quantum dots by the carriers that use quantum dots as recombination sites.

We conclude from figure 8.3 that switching the decay rate leads to a strong enhancement of the emission compared to the unswitched case. The duration of the emission enhancement is determined by the recombination rate of the free carriers, while the moment of increase is determined by the switch pulse. By applying the switch pulse we are able to deterministically enhance the spontaneous emission of an emitter and create an emission burst. The population density decreases and increases again due to the repopulation of the levels by the continuous wave excitation.

8.2.6 Population dynamics for pulsed excitation

The dynamics for pulsed excitation of the system are different from the dynamics for continuous wave excitation of the two-level sources. Equation 8.13 also describes the dynamics of the ensemble of two-level sources under pulsed excitation but it cannot be solved analytically. To obtain more insight, we will continue with the rate Eq. 8.7, which can be solved analytically for excitation with a Dirac pulse. We assume that the excitation pulse with amplitude P_{0exc} initializes the system at $t = t_{0exc}$ such that we have an intial population density $N_2(t = t_{0exc}) = N_{02}$. At times after excitation ($t > t_{0exc}$) Eq. 8.7 simplifies to:

$$\frac{dN_2(t - t_{0exc})}{dt} = -\left(\Gamma_{rad}(t - t_{0exc}) + \Gamma_{nrad}(t - t_{0exc})\right) N_2(t - t_{0exc}). \tag{8.15}$$

Equation 8.15 can be integrated to yield:

$$N_2(t - t_{0exc}) = N_{02} exp\left(\int_0^{t-t_{0exc}} -\left(\Gamma_{rad}(t') + \Gamma_{nrad}(t')\right) dt'\right). \tag{8.16}$$

Equation 8.16 shows that the population density can be calculated for any decay rate as a function of time after the excitation process is over.

The general solution of the rate Eq. 8.7 for a pulsed direct excitation of quantum dots can also be solved in case of a switched radiative decay rate as described in Eq. 8.12. Inserting Eq. 8.12 into Eq. 8.16 and solving the integral over the constant part of the decay rate yields

$$N_2(t - t_{0exc}) = N_{02} e^{-(\Gamma_{0rad} + \Gamma_{0nrad})(t - t_{0exc}) - \Delta\alpha_{rad}(t)}, \tag{8.17}$$

where we assumed that the non-radiative decay rate is time-independent $\Gamma_{nrad}(t) = \Gamma_{0nrad}$, since the non-radiative decay rate does not depend on the change of the LDOS. Furthermore, we define a dimensionless time-dependent switch parameter $\Delta\alpha_{rad}(t)$

$$\Delta\alpha_{rad}(t) = \int_0^t \frac{\Delta\Gamma_{srad}}{2} e^{\frac{-(t' - t_{0pu})}{\tau_{rec}}} \left[1 + erf\left(\frac{\sqrt{2}(t' - t_{0pu})}{\tau_{pu}}\right)\right] dt'. \tag{8.18}$$

The dimensionless time-dependent switch parameter $\Delta\alpha_{rad}(t)$ is the important figure of merit that describes the change in population density due to the switch of the decay rate. A negative $\Delta\alpha_{rad}(t)$ indicates that the population density decays slower, while a positive $\Delta\alpha_{rad}(t)$ indicates a faster decay compared to the unswitched situation.

If we reasonably assume that the duration of the switch pulse τ_{pu} is very short with respect to the recombination time τ_{rec}, the integral in Eq. 8.18 can be split into two parts - before and after the switch $t = \tau_{pu}$ - and $\Delta\alpha_{rad}$ becomes

$$\Delta\alpha_{rad}(t) = \frac{\Delta\Gamma_{srad}\tau_{rec}}{2}\left(1 - e^{\frac{-(t-t_{0pu})}{\tau_{rec}}}\right)\left[1 + erf\left(\frac{\sqrt{2}(t - t_{0pu})}{\tau_{pu}}\right)\right], \tag{8.19}$$

where we have multiplied with $erf\left(\frac{\sqrt{2}(t-t_{0pu})}{\tau_{pu}}\right)$ to account for the fact that there is no response of the system before $t = t_{0pu}$. The solution of Eq. 8.19 in the limit where time t tends to infinity is

$$\lim_{t\to\infty} \Delta\alpha_{rad}(t) = \Delta\Gamma_{srad}\tau_{rec}. \tag{8.20}$$

Equation 8.20 shows that the switch parameter is indeed dimensionless and is given by the product of a decay rate and a time constant. The switch parameter therefore describes the product of the duration and the magnitude of the switch, which makes it useful as a figure of merit.

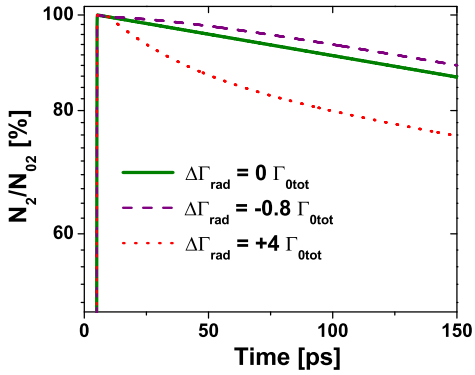

FIGURE 8.4: *Population density on a log scale as a function of time. The population density decreases faster if the decay rate is increased from 1 ns^{-1} to 5 ns^{-1} and decreases slower if the decay rate is decreased from 1 ns^{-1} to 0.2 ns^{-1}. The slope is the same for all three curves after the carriers recombination time τ_{rec} = 35 ps and the decay rate is back to its initial value.*

Figure 8.4 displays Eq. 8.17 for three cases: no change in decay rate, a decrease of the decay rate by 80 % and an increase of the decay rate by 400 %. The latter two

cases correspond to a decrease of the Purcell enhancement with a factor 5 and an increase of the enhancement by a factor of 5, as was reported in literature [11]. The population density decays clearly non-single exponentially. During the carrier recombination there is a strong deviation from the unswitched case, because the free carriers modify the decay rate. After recombination of the free carriers the population density does not converge to the unswitched case as for continuous wave excitation, because there is no continuous excitation of the ensemble. However, the ratio of change is the same as in the unswitched case.

Equation 8.20 and 8.17 show that the ratio of the switched population density N_{2s} and the unswitched population density N_{2us} in the limit of t tending to infinity is equal to

$$\lim_{t\to\infty} \frac{N_{2s}(t)}{N_{2us}(t)} = e^{-\Delta\Gamma_{srad}\tau_{rec}}. \tag{8.21}$$

Equation 8.21 states that for an increase of the decay rate the population density has decreased, due to the factor $\Delta\Gamma_{srad}\tau_{rec}$, after the effect of the switch has faded out. The population density increases due to a decrease of the decay rate. In the limit to infinity, when the excited free carriers have recombined, the ratio between the switched and unswitched cases is given by Eq. 8.21. In the case of a decreased decay rate (dashed in figure 8.4) the population density is larger than in the unswitched case as expected from Eq. 8.21. In the case of an increased population density, the population density is decreased as expected from Eq. 8.21.

8.2.7 Emission dynamics for pulsed excitation

The emitted intensity I_{em} is according to Eq. 8.9 equal to minus the time derivative of the excited state population, which is given by Eq. 8.7. Inserting the decay rate from Eq. 8.12, the population density from Eq. 8.17, and switch parameter from Eq. 8.19 into the rate in Eq. 8.15 with $\eta_{rec} = 0$ yields:

$$I_{em} = (\Gamma_{0rad} + \Delta\Gamma_{rad}(t))\,\frac{N_{02}}{2} e^{-\Gamma_{0tot}(t-t_{0exc})-\Delta\alpha_{rad}(t)} \left[1 + erf\left(\frac{\sqrt{2}(t-t_{0exc})}{\tau_{exc}}\right)\right], \tag{8.22}$$

with $\Delta\Gamma_{rad}(t) = \frac{\Delta\Gamma_{srad}}{2} e^{\frac{-(t-t_{0pu})}{\tau_{rec}}} \left[1 + erf\left(\frac{\sqrt{2}(t-t_{0pu})}{\tau_{pu}}\right)\right]$ and $\Gamma_{0tot} = \Gamma_{0rad} + \Gamma_{0nrad}$. The error function is present in Eq. 8.22 to describe that the emission starts at the moment the system is excited by the excitation pulse. Eq. 8.22 shows that the influence of the

switch remains visible in the emission after the free carriers have recombined. Because of the switch parameter $\Delta\alpha_{rad}(t)$ the emission is increased or decreased with respect to the unswitched case for a decreased or increased decay rate respectively. The shape of the emission is determined mainly by the factor $(\Gamma_{0rad} + \Delta\Gamma_{rad}(t))$ in the transient state.

Figure 8.5 shows the time-resolved emission in two switched cases and in the unswitched case on a logarithmic scale for clarity. It is clear that the emission increases if the decay

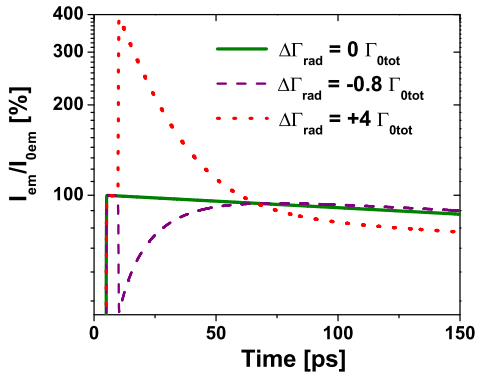

FIGURE 8.5: *Switched and unswitched emission (solid) as a function of time. The dotted line shows the switch in case of a decay rate that increases from 1 ns^{-1} to 5 ns^{-1}, while the dashed line represents a decay rate that is decreased from 1 ns^{-1} to 0.2 ns^{-1}. The decay dynamics of the ensemble is plotted showing the influence of the switch parameter after the carriers have recombined with a recombination time $\tau_{rec} = 35$ ps.*

rate is increased by the switch. A decreased emission is the result from a decreased decay rate. Figure 8.5 shows that after the carriers have recombined the emission is lower for the ensemble for which the decay rate was increased, while the emission is higher for the ensemble for which the decay rate was decreased. The reason is that the population density has changed as shown in Eq. 8.21. The emission after recombination of the excited free carriers is a measure for the population density and for the switch parameter.

Figure 8.5 shows that the emission can dynamically be increased or decreased by switching the LDOS. The speed of the effect shown in figure 8.5 is increased if the LDOS is not proportional to the carrier density as was assumed in the derivation of Eq. 8.22. We can see that this is the case near a cavity resonance for example. The LDOS as a

function of wavelength changes fast within the linewidth of the resonance. A change of the refractive index equal to the relative linewidth of the cavity resonance can change the Purcell factor experienced by quantum dots emitting off-resonance by a factor of 5, since the resonance frequency has shifted due to free carrier excitation. During recombination the Purcell factor of the quantum dots that were on-resonance right at the switch decreases steeply. When the free carrier concentration has decreased sufficient, the cavity resonance frequency no longer overlaps with the quantum dot emission line and the Purcell enhancement is equal to the initial value. At that moment the Purcell factor has become low again. In the case that the emission is switched using the resonance of a cavity, where the LDOS does not linearly depend on the excited free carrier density, the effects shown in figure 8.5 will be enhanced and be even more dramatic.

8.3 A realistic example: quantum dots in micropillars

8.3.1 Introduction to micropillars

One advanced type of optical cavities are micropillar cavities, which are photonic structures that are typically a few micrometers high and have a diameter between 1 μm and 20 μm (see also chapter 7). Micropillar cavities confine light in three dimensions. In the direction perpendicular to the Bragg layers (i.e., axial), optical confinement is achieved by the two Bragg-mirrors facing each other. Optical confinement in the direction parallel (i.e., transverse) to the Bragg layers is achieved by total internal reflection and a high refractive index contrast at the pillar edges [25]. Micropillar cavities support multiple resonances at discrete frequencies. Due to their geometry, micropillars allow direct optical probing and output coupling.

Figure 8.6 shows an SEM image of a micropillar cavity with 6 μm diameter and a height of 5.7 μm. Inside the pillar, parallel to the top facet, an optical cavity layer is sandwiched between two Bragg stacks. The micropillars often consist of GaAs/AlAs layers [3, 20, 27, 28], but pillars with HfO_2/SiO_2 layers for operating in the ultraviolet have also been reported in literature [29]. In the example that we are considering, the Bragg mirrors are made from layers of GaAs and AlAs, while the cavity is made of GaAs. All layers are grown by means of molecular beam epitaxy (MBE). The quantum dots are InAs dots and are placed inside the λ-cavity [20]. The system is optimized for spontaneous emission, therefore a low density of quantum dots is present. Furthermore,

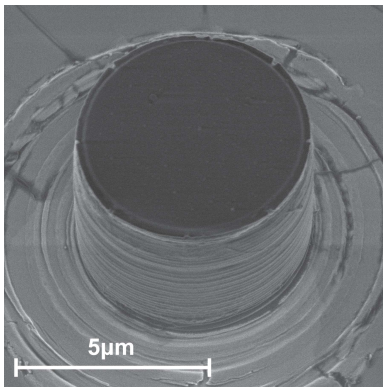

FIGURE 8.6: *SEM image of a micropillar cavity with 6 μm diameter and height of 5.7 μm. At the pillar edge one can see an alternating light- and dark-gray color pattern associated to the GaAs/AlAs Bragg stacks and the GaAs λ cavity.*

the dots' levels are optimally isolated from other levels than the levels participating in the desired transition.

In this work we study GaAs/AlAs micropillar cavities because they show a large Purcell effect [11] and they are used for the observation of strong coupling [3]. Micropillars are extensively studied by probing them from the inside using photoluminescence of quantum dots to determine the frequencies of optical resonances [20].

8.3.2 Micropillar cavities

The system under consideration is a micropillar with quantum dots. The main advantages of such a system are a small volume of the cavity, high Q factor, and directional outcoupling of the light. There are two micropillar resonator specific issues, which have not been incorporated into the general equation Eq. 8.22 for the time-dependent emission: The first category results from the fact that the field strength in a pillar resonator is spatial dependent. The second category results from the angular dependent emission from the various micropillar resonances.

A micropillar resonator supports a number of different resonances, which are often called modes [(2)]. Each resonance has thereby its own spatial field distribution inside the pillar, which influences the quality factor of the pillar [113] and the mode volume

[(2)] A mode can per definition only exist in a closed system. As soon as it couples to the outside world and can be measured, it is no longer a mode, but a resonance consisting of an infinite number of modes, with an infinitely small mode spacing. [7]

[118]. Furthermore, the decay rate of a quantum dot depends on the local field strength at the position of the quantum dot [119], which means that Eq. 8.22 becomes spatially dependent.

The emission is also angular dependent as was shown in [119, 120]. Each resonance of the micropillar couples out of the pillar under a specific angle, because of the angular dependence. Consequently, the outcoupling of emission changes if quantum dots couple to a different resonance due to the switched cavity. Similarly, since the center frequency is different for each resonance [20], emission can be switched between resonances. We will focus in the next sections on the fundamental resonance of the micropillar resonator since it has been studied extensively in literature [11, 20, 113, 118, 120–122].

8.3.3 Modeling of decay in micropillar

In this section we will focus on the spatial dependence of the field strength as introduced in the previous section. The emission of quantum dots inside a single mode cavity has been measured and modeled for the fundamental mode in [11, 119, 123]. It was concluded that the lifetime enhancement of the quantum dots not only depends on the Purcell factor, but also on the lateral position of the quantum dots inside the cavity and on the emission wavelength of the dots. This dependency results from the coupling between the dots and a single mode, which depends on the spatial mode profile, the position of the dots, and the emission wavelength [11, 119, 123]. For InAs quantum dots in a micropillar the decay rate $\Gamma(\omega)$ is given by [119]

$$\frac{\Gamma(\omega, \mathbf{r}, t)}{\Gamma_0} = F_p \frac{|\mathbf{E}(\mathbf{r})|^2}{|\mathbf{E}_{max}|^2} \frac{\omega_0^2(t)}{4Q^2(\omega - \omega_0(t))^2 + \omega_0^2(t)} + \gamma, \tag{8.23}$$

with Q the quality factor of the cavity resonance, $\mathbf{E}(\mathbf{r})$ the field as a function of position in the cavity, $\mathbf{E}_{max}$ the maximum field in the cavity, ω the emission frequency of the quantum dot, ω_0 the resonance frequency of the cavity, Γ_0 the radiative emission rate of the InAs quantum dots in a homogeneous GaAs matrix, $\gamma\Gamma_0$ is the emission rate in the leaky modes of the pillar, and F_p the Purcell factor, which is given by

$$F_p = \frac{3Q\lambda_c^3}{4\pi^2 n^3 V}, \tag{8.24}$$

with n the refractive index of the medium, λ_c the center wavelength of the cavity resonance, and V the effective mode volume of the resonant mode given by the spatial integral of the vacuum field intensity for the cavity mode divided by its maximum value [11].

Figure 8.7 shows the total field amplitude distribution of the HE11 mode calculated for a micropillar with a diameter of 8 micrometer. For an ensemble of non-interacting

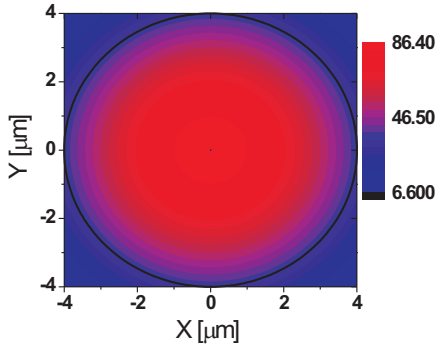

FIGURE 8.7: *Calculated mode profile of fundamental micropillar mode HE11, 2R=8 μm. The colorscale indicates the absolute value of the electric field. The black circle indicates the pillar edge. The fundamental mode has a field maximum in the middle of the pillar. The field amplitude decreases towards the edge of the pillar.*

and equal quantum dots in a micropillar cavity the total emitted intensity is equal to the integral of the intensity of one quantum dot at position **r**:

$$I_{tot}(\omega, t) = \int_0^{2\pi} \int_0^R I_{QD}(\omega, \mathbf{r}, t) d\mathbf{r} d\phi, \tag{8.25}$$

with ϕ the angle of the vector **r** and $I_{tot}(\omega, t)$. From Eq. 8.23 and from figure 8.7 it is clear that the field *E(r)* strongly depends on position, therefore the decay rate Γ and thus the distribution of the decay rates $c(\Gamma(\boldsymbol{r}, t))$ strongly depend on the position **r**. Integrating the integral over ϕ, the integral over **r** in Eq. 8.25 becomes:

$$I_{tot}(\omega, t) = 2\pi \int_0^R c(\Gamma(\mathbf{r}, t)) \Gamma(\mathbf{r}, t) \exp\left(-\Gamma(\mathbf{r}, t)\, t\right) d\mathbf{r}. \tag{8.26}$$

Similarly, the population density is given by:

$$N_2(\omega, t) = 2\pi \int_0^R c(\Gamma(\mathbf{r}, t)) \exp\left(-\Gamma(\mathbf{r}, t)\, t\right) d\mathbf{r}. \tag{8.27}$$

From mode profiles as given in figure 8.7 we obtain the distribution of the decay rates $c(\Gamma(\boldsymbol{r}))$, which is shown in figure 8.8 together with the distribution for $\Gamma(\mathbf{r}, t)c(\Gamma(\mathbf{r}, t))$. We normalized the decay rate axis to the maximum decay rate in the mode, which is found at the maximum field amplitude E_{max}. The distribution $c(\Gamma(\boldsymbol{r}))$ is by definition normalized, since the integral over the decay rate Γ yields 100 %, which corresponds to the total area of the pillar. It is clear from figure 8.8 that there are no decay rates below 16 % of the

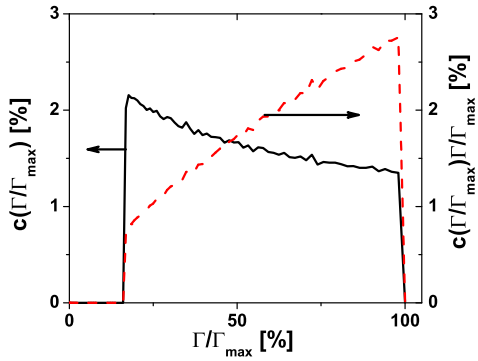

FIGURE 8.8: *Distribution of the decay rates* $c(\Gamma(\mathbf{r}))$ *(black solid) and the distribution for* $\Gamma(\boldsymbol{r}, t)c(\Gamma(\boldsymbol{r}, t))$ *(red dashed) as a function of* Γ. *The decay rate axis is normalized to the the maximum decay rate in the mode, which is found at the maximum field amplitude* E_{max}.

maximum value. The reason is that there is no node in the pillar for the HE11 mode. The multiplication of $c(\Gamma(\boldsymbol{r}))$ with the decay rate changes the shape of the distribution from a downward slope toward the maximum decay rate to an upward slope.

Figure 8.9 shows the population density for quantum dots that emit in the HE11 mode, and a single exponential fit to the population density curve. The timescale τ_{Emax} is the lifetime at the maximum field intensity E_{max}. The curve in figure 8.9 is only based on the position of the quantum dots in the cavity. We assumed a homogeneous quantum dot distribution and used distributions as in figure 8.8 and Eq. 8.27 to calculate the curve in

figure 8.9. Figure 8.9 shows that the population density decays non-single exponentially,

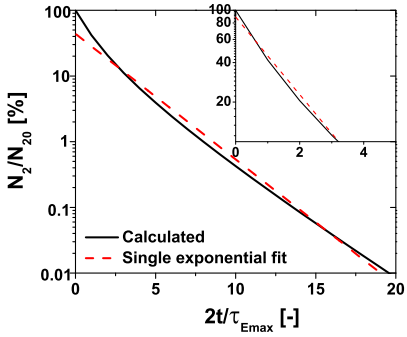

FIGURE 8.9: *Calculated dynamic population density (black solid) and single exponential fit (red dashed) of a homogeneously distributed layer of quantum dots that emit in the fundamental mode. The minimum lifetime τ_{max} corresponds to the lifetime of the quantum dots at areas with a maximum field amplitude and therefore a maximum increase of the decay rate. The decay curve is non-single exponential, but can be quite accurately fitted with a single exponential fit over the four shown decades. The inset shows the population decay curve and single exponential fit over 1 decade.*

because of the distribution of rates shown in figure 8.8. Interestingly, the deviations from single exponential decay are moderate, since a single exponential model fits reasonably well to the decay curve over four decades. We conclude from figure 8.9 that the term $|\mathbf{E}(\mathbf{r})|$ in Eq. 8.23 can be reasonably modeled as a constant independent of position in case of the population density.

With the distribution for $\Gamma(\mathbf{r},t)c(\Gamma(\mathbf{r},t))$ and with Eq. 8.26, we have calculated the intensity decay curve for emission in the HE11 mode as shown in figure 8.10. The intensity decay curve is usually measured in time correlated single photon counted experiments to determine the quantum dot decay rate. As is the case for the population density, the intensity decay curve is non-single exponential. Non-exponential decay due to a distribution of sources has recently been observed for quantum dots in photonic crystals [124] and was modeled with an analytical decay rate distribution. Interestingly, here we do not assume such a distribution but calculate it ab-initio from the known properties of the cavity. In a homogeneous medium, the quantum dots decay single exponentially. We have also plotted in figure 8.10 a single exponential fit that agrees reasonable well with our results. The

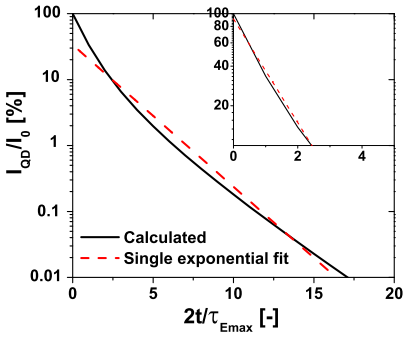

FIGURE 8.10: *Calculated decay curve (black solid) and single exponential fit (red dashed) for a homogeneously distributed layer of quantum dots that emit in the fundamental mode. The minimum lifetime τ_{max} corresponds to the lifetime of the quantum dots at areas with a maximum field amplitude and therefore a maximum increase of the decay rate. The decay curve is non-single exponential, but can be quite accurately fitted with a single exponential fit over the four shown decades. The inset shows the decay curve and single exponential fit over 1 decade.*

single exponential behavior can be explained by the slightly peaked distribution in figure 8.8. This apparently single exponential behavior is in agreement with measurements on GaAs/AlAs micropillars, where a limited dynamical range (1 decade) was measured [11]. We conclude from figure 8.10 that the influence of the spatial distribution of the quantum dots on the emission is very small for the fundamental mode. For higher-order modes we find more strongly non-exponential decay curves.

8.3.4 Influence of leaky modes

The second category of pillar specific issues result from the angular dependence of the emission. Each mode has a preferable emission angle, which compounds the measurement [120]. Here we will focus on the emission in the fundamental mode and the leaky modes and not consider the higher-order modes. We assume that there are only two possible angles of emission, first, the emission angle of the fundamental mode in the axial direction of the pillar and second, the emission angle of the leaky modes perpendicular to the pillar axis.

The measured emission intensity $I(\omega, \mathbf{r})$ from an excited quantum dot, which emits $I_{QD}(\omega, \mathbf{r})$ photons per second, at position $\mathbf{r}$ in a pillar is equal to [119]

$$I(\omega, \mathbf{r}) = AI_{QD}(\omega)\frac{|\mathbf{E}(\mathbf{r})|^2}{|\mathbf{E}_{max}|^2}\frac{\Gamma_0 F_p}{\Gamma(\omega)}\frac{\omega_0^2(t)}{4Q^2(\omega-\omega_0(t))^2+\omega_0^2(t)} + BI_{QD}(\omega)\frac{\gamma\Gamma_0}{\Gamma(\omega)}, \qquad (8.28)$$

with A and B the collection efficiencies for the cavity mode and leaky mode respectively.

It is clear from Eq. (8.23) that if the cavity resonance is much detuned the Purcell enhancement is decreased. For large detuning the Lorentzian term becomes small and the first term in Eq. 8.28 representing emission in the cavity mode becomes small compared to the second term representing the leaky modes. At large detuning the emission mainly results from leaky modes, which means that the emission is redistributed over the out-coupling angles of the leaky modes. In an experiment, one may typically collect all light from guided cavity modes ($A = 1$ in Eq. 8.28), but not all leaky modes ($B < 1$ in Eq. 8.28). This affects the detected signal contrast: during a switch from off- to on-resonance the emission changes from emission into leaky modes (B-term) to emission determined by both sets of modes (A and B). If $B = 0$, which means we do not probe any leaky modes, the contrast between the switched and unswitched case is maximum. It is thus possible to increase the contrast between the switched and unswitched case by detecting as little leaky modes as possible.

From the previous sections we conclude that our model for switching the emission is applicable to the fundamental mode of micropillar resonators. Our model takes into account the spatial distribution of quantum dots and leaky modes of the micropillars. We predict that switching spontaneous emission yields a large signal in both continuous wave or pulsed settings, which should be measurable in an experiment. Therefore, we conclude that it is possible to switch the emission of quantum dots in a micropillar resonator and thereby control spontaneous emission in time.

8.4 Conclusion

We have studied the deterministic switching of spontaneous emission of light sources in a cavity. We have presented a model geared toward quantum dots in micropillars, as studied in chapter 7. We have introduced the product between the radiative decay rate and the switch time as a switch parameter. We have demonstrated that by increasing the radiative

decay rate the emission drastically increases during the switch time for both continuous wave excitation and pulsed excitation. Furthermore, we showed that our modeling can be applied to micropillar resonators that are widely used.

CHAPTER 9

Inequivalence between the von Laue and the Bragg conditions observed for light in 2D photonic crystals

9.1 Introduction

The von Laue and the Bragg conditions describe scattering and propagation of any kind of wave phenomenon (e.g., light, sound, electrons) in periodic lattices [15, 125]. Both conditions are widely used in physics, from semiconductor physics (transistors) to nanophotonics, with applications in optical communication. Furthermore, the von Laue and Bragg conditions are very important for crystallography using x-ray diffraction [126], i.e., for characterization of ionic crystals, of molecular crystals in general and of proteins like DNA and RNA whose structure is crucial in the case of pharmaceutics [127], determining their functionality.

The von Laue condition formulates the band splitting condition for scattered waves with the use of wave vectors in reciprocal space. The famous von Laue condition ($\vec{K}_{out} - \vec{K}_{in} = \vec{G}$) is met, if the difference between the incoming wave vector $\vec{K}_{in}$ and scattered wave vector $\vec{K}_{out}$ is equal to a reciprocal lattice vector $\vec{G}$. A consequence of the von Laue condition as shown for a square lattice in figure 9.1 A, is that the wave vector from Γ to K not only lies on the edge of the first Brillouin zone, but also satisfies the condition for Bragg reflection in the $\Gamma - K$ direction. That the von Laue condition is met can be seen, for the case of elastic scattering, by introducing a diffracted wave vector with the same length as the impinging wave vector, drawn from Γ to K in figure 9.1 A. The scattered wave vector has the same length, but points in the opposite direction as the impinging

wave vector. The vectorial difference between the scattered and impinging wave vector is equal to the reciprocal lattice vector $\vec{K_{out}} - \vec{K_{in}} = \vec{G}_{11}$. Thus, the von Laue condition is satisfied.

The Bragg condition states the band splitting condition for scattered waves with the use of lattice planes in the direct lattice, i.e., in real space. The famous Bragg condition ($\lambda = 2dncos\theta$) is satisfied at normal incidence ($cos\theta = 1$)if the wavelength is equal to twice the interplane distance. The impinging wave vector is therefore equal to half the reciprocal lattice vector representing the set of lattice planes from which the light is reflected. The reciprocal lattice vector $\vec{G}_{11}$ represents the <11>-lattice planes in the direct lattice in real space with an interplane distance d. For this set of planes the Bragg condition is met at an impinging wave vector with a length equal to half the reciprocal lattice vector.

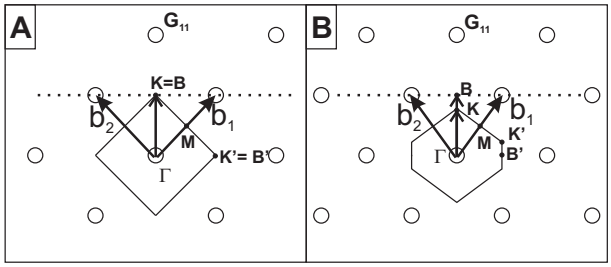

FIGURE 9.1: *Representation of the first Brillouin zone for a square (A) and a $\sqrt{2}$-lattice (B), having a lower symmetry than the square lattice. The vectors b_1, b_2 are primitive vectors of the reciprocal spaces, while G_{11} is a reciprocal lattice point equivalent to the Γ point (hk=11). Γ, K, K', B, B' and M are points of high symmetry of the Brillouin zone. The dotted lines are the hk = 11 Bragg planes.*

From figure 9.1 A we can see the well known situation that the impinging wave vector, for which both the Bragg and the von Laue conditions are met, is the same in the $\Gamma - G_{11}$-direction in the case of a square lattice, because the length of the vector between Γ and the edge of the Brillouin zone is half the length of the reciprocal lattice vector also known as the Bragg plane (dotted line figure 9.1 A). The reasoning also holds in 3D for a cubic lattice.

In periodic systems the Bragg and von Laue conditions are equally general. For non-periodic systems, however, the von Laue condition is expected to be more general [125].

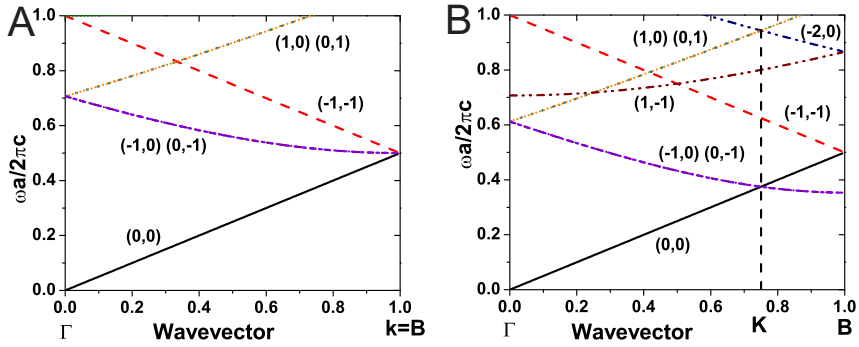

FIGURE 9.2: *Calculated vacuumbands for a square lattice (A) and $\sqrt{2}$-lattice (B).*

Structures with lower symmetry than the square lattice are very common. In certain species of butterflies for example, the lowest symmetry results in a broadband reflection for all directions [128]. Also high-T_c superconductors have a lower crystal symmetry [129, 130]. Furthermore, a 2D crystal lattice with a lower symmetry than square is the basis for 3D woodpile photonic crystal, which promises a broad first order bandgap [57].

In this chapter we will describe a case where the Bragg condition deviates from the von Laue condition. We investigate the bandstructure and give insight into the formation of a stopgap in lattices with a lower symmetry than cubic.

9.2 Brillouin zone and bandstructure in case of no interaction

Simple Bragg The bandstructure can be calculated analytically for a massless wave equation in a square lattice with no interaction, like photons and phonons. If the particles have masses as in the case of electrons, the shape of the bands change. The fact that the position of the stopgap changes due to a lower symmetry of the lattice is valid for all types of particles however. The bandstructure in the limit of zero interaction for the reciprocal lattice shown in figure 9.1 A is shown in figure 9.2 A. In the bandstructure, the band coordinates are given as (hk), which corresponds to reciprocal lattice points $h\vec{b_1} + k\vec{b_2}$ in figure 9.1 A. The *00*-band and the $\bar{1}\bar{1}$-band cross each other at the edge of the Brillouin zone.

This crossing is the origin of the stopgap that opens if the interaction strength is non-zero. This is a case of Bragg splitting.

Multiple Bragg The second set of bands that are curved and start at the edge of the Brillouin zone ($\bar{1}0$- and $0\bar{1}$-band) originate from the reciprocal lattice vectors $G_{0\bar{1}}$ and $G_{\bar{1}0}$. The result is a multiple Bragg condition [131]. As the interaction strength is increased, these bands start to repel the other bands at the edge of the Brillouin zone, thereby forming a composite gap [132] for the same wavevector as the Bragg condition.

The case of a symmetric square lattice, as described above, is well known and confirmed by measurements. The situation changes, however, when the symmetry of the crystal lattice is lowered.

Lower symmetry lattice The reciprocal lattice with the first Brillouin zone of a lower symmetric 2D crystal lattice is shown in figure 9.1 B. The lowered symmetry of the lattice also appears in the reciprocal lattice: Due to the lowered symmetry the *B*- and *K*-point no longer overlap. The *K*-point shifts towards the Γ-point. In a similar way the *B'*- and *K'*-point no longer overlap. The Brillouin zone has six sides instead of four in the lower symmetry case, because a plane appears perpendicular to the $G_{1\bar{1}}$ direction. The von Laue condition is still met at the edge of the Brillouin zone in the *K*-point. The Bragg condition, however, is not met at the edge of the Brillouin zone anymore, but halfway the reciprocal lattice vector $\vec{G_{11}}$ in the Bragg plane through *B*.

The bandstructures of the lower symmetry lattice is shown in figure 9.2 B. It is seen that there are more bands in the low frequency region. The bands originating from the G_{00} and the $G_{\bar{1}\bar{1}}$ reciprocal lattice vectors are unchanged despite the symmetry change. The Bragg condition is therefore fulfilled at the same wavevector (*B*) in both symmetry cases. If the interaction strength is increased, the bands start to split at the B point.

The $\bar{1}0$ and $0\bar{1}$ bands, however, decrease in frequency due to the lower symmetry. Because the $0\bar{1}$ and the $\bar{1}0$ bands are lowered in frequency, they cross the 00 band at the *K*-point. The bands originating from the multiple Bragg diffraction at the edge of the Brillouin zone in the cubic lattice now cross the first 00 band at the edge of the Brillouin zone. If the interaction strength is increased, these bands split and a gap opens up at the *K*-point, at the edge of the Brillouin zone. But this *K*-point is not anymore the Bragg plane. Therefore we conclude that we have identified a condition where the Laue condition and the Bragg condition are not equivalent anymore.

9.3 Results and discussion

To confirm our results, we studied strongly interacting photonic crystals made of silicon, both experimentally and by bandstructure theory. To calculate bandstructures, we used the MIT photonic bandgap program [133][(1)]. For the symmetric lattice case we studied a three-dimensional silicon inverse opal [46, 134], and for the case of a low-symmetry lattice we studied a two-dimensional macroporous crystal. Because of new fabrication techniques it is possible to etch large sets of pores suitable for two-dimensional photonic crystal fabrication. The calculated bandstructure for a symmetric fcc lattice is shown in figure 9.3 A. In this structure the Bragg condition and the von Laue condition are met at the same wavevector: Figure 9.3 A shows that band splitting occurs at the *L*-point of the Brillouin zone. The hatched regions indicate the connection with the reflectivity measurements on a silicon inverse photonic crystal shown in figure 9.3 C. The first hatched region shows the perfect agreement between both the position and the width of the peak in the reflectivity spectrum and the position and width of the stopgap in the bandstructure. Here a splitting occurs at the *L* position, resulting in a peak in the reflectivity spectrum. The reflectivity measurements confirm the validity of the bandstructure calculation. The spectrum was measured by Euser et al. [46]; a similar good agreement was obtained for silica opals studied in chapter 10. The three peaks at higher frequencies in the reflectivity spectrum are associated with three gaps. In this region the bandgap of the silicon inverse opal is predicted to occur [46, 134].

The calculated bandstructure for a low-symmetry lattice with interaction is shown in figure 9.3 B. The measurement on the photonic crystal is presented in figure 9.3 D. Figure 9.3 B shows the bandstructure calculated with the parameters of the fabricated structure. Figure 9.3 D shows the reflectivity measurement on the photonic crystal that confirms the validity of the calculated bandstructure. Figure 9.3 B shows a splitting of bands at four positions indicated with hatched regions, numbered I to IV; only at reduced frequencies of 0.33 and 0.81 two stopgaps form. The other two potential gaps are traversed by bands. Figure 9.3 D shows three broad peaks in regions I, II, III and four spikes. The first broad peak in region I shows excellent agreement with the first gap due to a splitting of the bands at the *K*-point, where the von Laue condition is met. The second broad peak is spectrally positioned were the bands split at the edge of the Brillouin zone due to the Bragg condition. This means that in the reflectivity measurement the von Laue condition is satisfied

[(1)] Calculations were kindly performed by Allard P. Mosk.

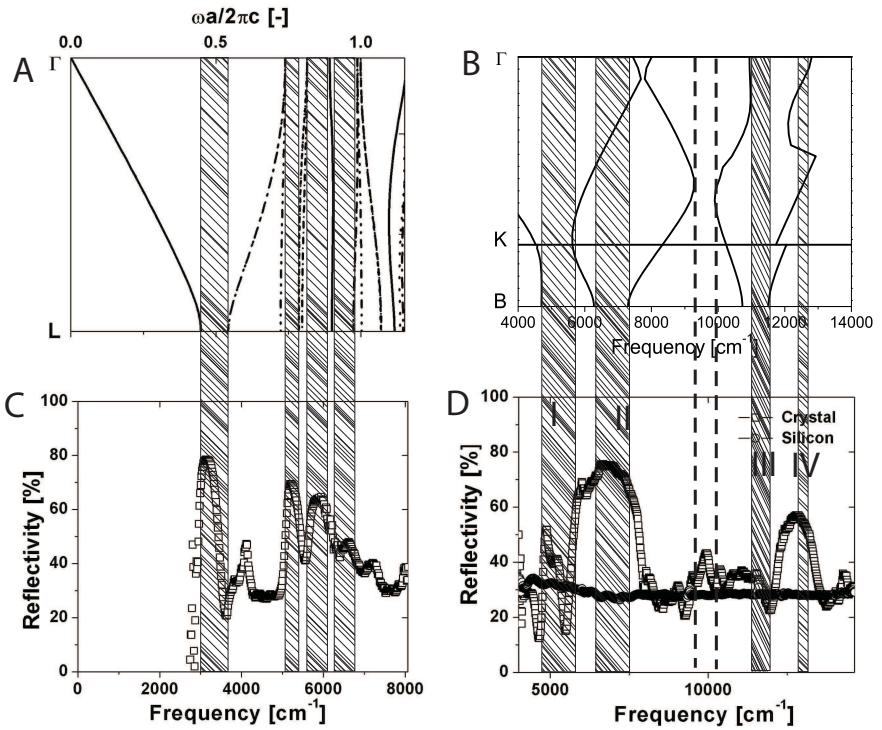

FIGURE 9.3: *(A) Bandstructure of a silicon inverse opal photonic crystal with a symmetric (fcc) lattice, having a band splitting at the* L*-point. In this case the von Laue condition and the Bragg condition are equivalent. The hatched regions indicate the overlap between a gap at the* L*-point in the bandstructure and reflectivity peaks in figure 9.3 C (B) Bandstructure for an infinite two-dimensional crystal with a silicon volume fraction of 77.5%, which corresponds to air pores with a radius of 120 nm. The hatched spectral regions correspond to regions where bands split and stopgaps form (region I, III, IV in figure 9.3 D) and the region where the bands split due to the Bragg condition, but no stopgap is formed (region II). The four dashed vertical lines indicate flat bands in spectral regions where we measured spikes in the reflectivity spectrum (figure 9.3D). (C) Reflectivity spectrum of a silicon inverse opal photonic crystal. The spectrum shows a very clear peak from the* L*-gap at 3117* cm^{-1}*. Three other peaks are visible at 5185* cm^{-1}*, 5848* cm^{-1}*, 6573* cm^{-1}*, data from [46]. (D) Reflectivity spectra of a two-dimensional silicon photonic crystal and bulk silicon. The spectrum of the photonic crystal shows three distinct peaks, at 5000* cm^{-1}*, 6851* cm^{-1} *(compound peak) and 12791* cm^{-1}*. The peak reflectivity values are 50%, 75%, and 60% and the relative linewidths are 15%, 33% (of compound), and 8.9%. The spectrum of the unetched silicon is flat as expected. The hatched areas give the frequency region of stopgaps in the bandstructure. The dashed vertical lines correspond to the frequency positions of zero dispersion bands.*

at a different frequency than the Bragg condition. Both conditions are inequivalent as is also shown by the calculations. The reflectivity peak is the result of the bands traversing the gap. Light does not couple from outside the crystal to this band. Similarly, the peak numbered IV is measured since light does not couple from outside the crystal to these bands either. The shoulder on the reflectivity peak number II is the result from the bended bands at about 0.4 reduced frequency. The latter are indicated with dashed lines to show the agreement of the spectral positions of the spikes and the spectral position of flat bands.

We conclude from the agreement between figure 9.3 A and C and from the agreement between figure 9.3 B and D that the bandstructure calculations agree with the measurements. Therefore, we conclude that in a low-symmetry lattice band-splitting indeed occurs at a lower reduced frequency than in the case of a high-symmetry cubic symmetry.

The calculated bandstructure is valid for massless particles with no interaction and therefore also for phonons. In case of a phonon bandstructure, band-splitting at lower frequencies due to a lower symmetry lattice has consequences for the specific heat. Bending of the bands sets the boundary between the low temperature specific heat and the high temperature specific heat [125]. Band splitting at lower frequencies due to a lower symmetry lattice therefore implies that the boundary shifts to lower frequencies. Furthermore, there is a relation between the phonon density of states and the critical temperature T_c [129]. Therefore our results have also implications for the critical temperature in the case of waves in a lower symmetry lattice.

Our results also have implications for X-ray diffraction, where the interaction strength of the crystal is very small and where we can use the vacuum band structures from figure 9.2. Our results imply that an extra diffraction peak appears for a crystal with an asymmetric lattice. One peak is the result of the edge of the Brillouin zone, the other of the Bragg reflection of the crystal. This should be taken into account when reconstructing the crystal structure from a diffraction pattern.

9.4 Conclusion

We conclude that for a high symmetry lattice the Bragg condition follows from the von Laue condition, but not for lower symmetry lattices. We have shown calculations and measurements on a three-dimensional silicon inverse opal photonic crystal and on a two-dimensional silicon photonic crystal to demonstrate our findings.

CHAPTER 10

Structural and optical properties of opals grown with vertical controlled drying

10.1 Introduction

Monodisperse nanometer-sized particles have the ability to self-assemble into colloidal photonic crystals. These self-assembled photonic crystals, also called artificial opals, have attracted much attention over the last years. They have a face-centered cubic packing and were used by many groups as a template to create so-called inverse opals [134–137]. Both silica and polystyrene nanospheres have been used to create templates for the synthesis of titania [138] and silicon [134, 136] inverse opals for photonic crystal applications.

Methods like sedimentation and vertical controlled drying [139] among others [140] have been introduced to form thick and thin-film opals, respectively. In the sedimentation method the spheres in a suspension are left to sediment naturally [141, 142]. Spheres with radii larger than 400 nm do not have time to arrange themselves in crystalline packing due to a very fast sedimentation, leading to a lower crystalline quality. A solution to this problem was proposed by Holgado *et al.*, who used electrophoresis to slow down the spheres [143]. Control of the shape of the crystal remains limited with sedimentation and therefore vertical controlled drying has become the most favorable method lately. This method is based on the one Dimitrov and Nagayama used to deposit monolayers of submicrometer spheres onto a substrate [144]. The vertical controlled drying technique pioneered by Jiang *et al.* [139] consists of placing a substrate into a dispersion. When the solvent evaporates the spheres form a thin crystalline layer on the substrate.

Much work has been published on the vertical controlled drying method. Despite much work, there is still an ongoing debate about the crystal formation [144, 145], and the size and thickness limits of crystal domains have not been investigated yet. These limits are the subject of this chapter. The thickness of the crystal determines the intensity and the relative linewidth of Bragg reflections [146, 147] and its limits are therefore relevant to optical applications. The lateral sizes of a photonic crystal should be larger than the spot diameter of typically used laser beams. Also, crystals should be large enough to allow functionalization with waveguides [148] and cavities [33]. Interestingly, the shape and size of the domains contain valuable information on the drying process [149–155].

Crack formation during the infiltration of opals has been investigated [156]. It was shown qualitatively that calcination of the spheres increased the crystal domain size of the inverse photonic crystal after an LPCVD infiltration at 823 K.

Here, we have grown opal photonic crystals while varying the growth temperature and the volume fraction of the dispersion. We will focus on two structural parameters, namely the domain size and the thickness of the crystal, to obtain a three-dimensional picture of the crystal domains. We will discuss the limits of the vertical controlled drying technique with respect to crystal domain size and thickness.

10.2 Experimental Section

10.2.1 Opal fabrication

We used silicon dioxide colloidal spheres synthesized with a microemulsion method as were used earlier by Megens *et al.* [157]. These spheres have radii of 113 nm with a polydispersity of 1.5% and were dispersed in ethanol. The opals were grown with the vertical controlled drying method [139] on a 2.5 cm long glass substrate, placed under an angle of 30° with respect to the vertical walls of the beaker (figure 10.1 A). The beaker with the substrate and 2 ml of solution was placed inside an oven. The temperature T of the oven and the initial volume fraction of spheres in the dispersion (Φ_i) were varied in the experiments discussed here. The accuracy of the volume fraction of the bulk is conservatively estimated to be within 5% of Φ_i. The temperature T is estimated to stay constant within 1 degree. We chose temperatures to increase the evaporation speed of the ethanol with respect to room temperature, staying well below the boiling point. Multiple samples were grown at the same time in the oven to check the reproducibility.

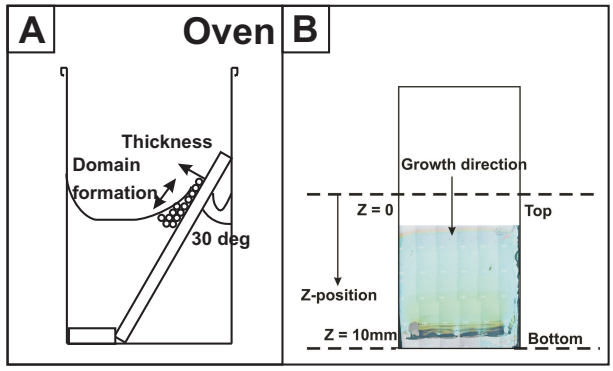

FIGURE 10.1: *(A) Setup used for the growth of the thin film opals. The substrate is placed in a dispersion under an angle of 30 degrees. The crystal domains form in the direction parallel to the surface, while the thickness is defined perpendicular to the sample. (B) Optical microscope picture of a typical opal. The growth direction, the top and the bottom are indicated. The terminology shown in this figure is used in the text.*

For convenience the height variable z is defined as 10 mm minus the actual position on the substrate, see figure 10.1 B. The position $z = 0$ corresponds to a height on the substrate of 10 mm. The position $z = 10$ mm corresponds to the bottom of the substrate since the crystal grows towards this position. The position $z = 10$ mm rests on the bottom of the beaker during the crystallization process.

10.2.2 Thickness measurement

The thickness of each of the thin-film opals was derived from the Fabry-Pérot fringes in optical reflectivity spectra. The reflectivity spectra were measured with a set-up similar to the one in reference [61] using a Fourier-transform spectrometer (Biorad FTS6000). An objective with a small numerical aperture of 0.05 was used to focus the collimated beam onto the sample. Reflectivity spectra were measured at different spots along the z-axis of the substrate. An example of a reflectivity spectrum is shown in figure 10.2.

The main features present in the spectrum are the Fabry-Pérot fringes and the reflectivity peak resulting from the first order photonic stopband of the opal at frequency ω_0, with a reflectivity R_{sb}, and a linewidth $\Delta\omega$. R_{min} and R_{max} give the minimum and maximum reflectivity of a fringe. The thickness d of the sample (in nm) can be calculated from

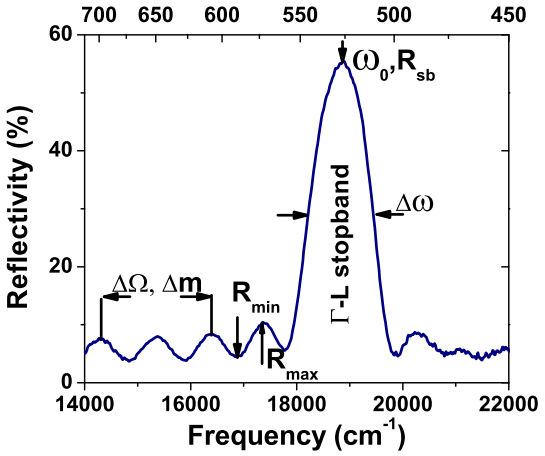

FIGURE 10.2: *The reflectivity spectrum shows a first order stopband and Fabry-Pérot fringes. The high reflectivity peak of 55% at 18880 cm^{-1} is the result of the $\Gamma - L$ stopband. The frequency difference between Δm Fabry-Pérot fringes is indicated by $\Delta\Omega$. Here Δm = 2 and $\Delta\Omega$ = 2083 cm^{-1} are indicated.*

the spacing $\Delta\Omega$ of the fringes with

$$d = \frac{10^7}{2n_{eff}} \frac{\Delta m}{\Delta\Omega}, \tag{10.1}$$

where Δm is the difference in order between the different fringes, the fringe order, and $\Delta\Omega$ is the fringe spacing in cm^{-1}. We used all fringes on the red side of the stopband except the one closest to the stopband, since this fringe closest is affected by photonic band bending. The effective refractive index n_{eff} is taken to be the volume-averaged refractive index $n_{eff} = (1 - \phi)n_l + \phi n_h$, where ϕ is the volume fraction of silicon dioxide ($\phi = 0.74$ for fcc close-packed spheres), n_l is the refractive index of the low refractive index material (in our case $n_l = 1$ for air) and n_h is the refractive index of the high refractive index material ($n_h = 1.465 \pm 0.004$ for silicon dioxide colloids [158]). A thickness $d = 4.79$ μm can be derived from figure 10.2, with $n_{eff} = 1.33$, $\Delta m = 2$, and $\Delta\Omega = 2083$ cm^{-1}. This thickness derived from figure 10.2 is shown in figure 10.4B at a growth position $z = 5.5$ mm. The size of the error bars on the thickness measurements is conservatively estimated as 0.13 times the thickness. The number of 0.13 is derived from statistics performed on sample

spectra taken randomly from the full set of measurements presented in this work. The distance between the lattice planes can be derived from the stopband position with the use of Braggs law: $d_{111} = \frac{\lambda_c}{2n_{eff}}$. With λ_c the position of the stopband. The distance between the lattice planes derived with figure 10.2 is 197 μm.

No thickness data could be recorded if there were no fringes visible in the spectrum. This was in general the case near the bottom of the substrate. The reason is that the opals are so thick near the bottom, that the coherence between the light reflected from the air-opal interface and from the opal-substrate interface is lost due to extinction. The thickest measurable thickness was found to be about 10 μm.

10.2.3 Domain size measurement

The domain size (L) was measured with a scanning electron microscope (SEM, FEI XL30 SFEG). Figure 10.3 A shows a scanning electron micrograph from the surface of an opal. The different crystal domains are irregularly shaped. The spheres are fcc-packed within one domain, see figure 10.3 B. Adjacent crystal domains fit like the pieces of a jigsaw puzzle, indicating that the cracks separating them were formed after the spheres ordered themselves in a crystal structure. The cracks are the result of stress formation during the drying of the crystal.

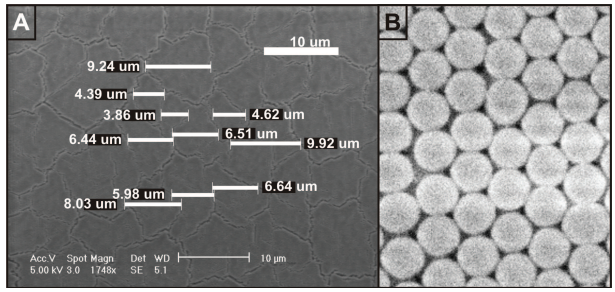

FIGURE 10.3: *(A) Scanning electron micrograph of an artificial opal. The photograph shows single crystal domains that are bounded by grain boundaries or cracks. The labels indicate the measured domain widths. The ten values measured from the scanning electron micrograph form one data set from which the average domain size is calculated. The average domain size (<L>) for this picture is <L> = 6.5 μm ± 2 μm. The crystal growth direction is from top to bottom of the picture. (B) Close-up within one crystal domain, revealing excellent crystalline order. The hexagonal arrangement is typical of a fcc (111) face.*

Each value of the average domain size is derived from a set of ten values taken from a SEM picture like the one shown in figure 10.3 A. The size of the domain is systematically measured in both the horizontal and the vertical direction with respect to the growth direction of the opal. The domain widths are drawn through the estimated center of mass of the domain. The first measurements of the set of ten are always taken in the central domain of the SEM picture, followed by neighboring domains.

10.2.4 Extinction length

The frequency and amplitude of the Fabry-Pérot fringes in the reflectivity spectra are not the same for every sample and even depend on the position on the sample. The fringes contain information on the thickness and the extinction length of the opal on the measured position.

The reflection from a thin film can be calculated with

$$\frac{R_{max}}{R_{min}} = \frac{(r_{01} + r_{top})^2}{(r_{01} - r_{top})^2}. \tag{10.2}$$

With R_{max} the maximum reflectivity of a fringe and R_{min} the minimum reflectivity of a fringe as shown in figure 10.2, r_{01} the Fresnel reflection from the opal-air interface and r_{top} which is given by equation

$$r_{top} = (1 - r_{01})^2(r_{12}e^{-2d/L_{ext}} + r_{01}e^{-4d/L_{ext}}r_{12}^2). \tag{10.3}$$

Where r_{01} is the Fresnel reflection from the opal-air interface, r_{12} the Fresnel reflection from the opal-glass interface, d the thickness of the crystal, and L_{ext} the extinction length of the electromagnetic field intensity.

The maximum value of constructive interference of the fringes is obtained if all reflected waves are in phase, while a maximum of destructive interference is obtained when all components are out of phase. Therefore, the amplitudes of the reflected beams (r_{top}) are subtracted or added respectively to the Fresnel reflection of the opal-air interface.

Refractive indices of 1.33 and 1.5 are assumed for the opal and the glass, respectively, in order calculate the Fresnel reflection coefficients. Only two terms are taken into account in Eq. 10.3, since the contribution of the other reflections can be neglected. In order to find the extinction length, we minimized the difference between the measured ratio of R_{max} and R_{min} and the function as given in 10.2 with the extinction length as parameter.

10.2.5 Relative linewidth

An interesting property of the $\Gamma - L$ stopband that can be extracted from figure 10.2 is the relative linewidth $\frac{\Delta\omega}{\omega_0}$. The relative linewidth is defined as the full width at half maximum of the reflectivity peak, due to the $\Gamma - L$ stopband, divided by the center frequency of the reflectivity peak. The relative linewidth gives information on the photonic strength [159]. In figure 10.2 the relative linewidth is equal to 5.2 %.

10.3 Results and Discussion

10.3.1 Visual sample appearance

Figure 10.1 B shows an optical microscope image of a typical thin film opal photonic crystal. It shows the green color that results from the first order Bragg diffraction. Furthermore, there are domains surrounded by cracks visible. In figure 10.1 B it can be seen that the color of the sample is not homogeneous. The green color at the top of the thin-film crystal is lighter than the green color at the bottom of the sample. A more careful look at the image also reveals large domains at the bottom of the sample. The domains become smaller towards the top and become irresolvable for the optical microscope. The inhomogeneity of the sample is already apparent from the optical microscope picture. In the next sections the inhomogeneity will be quantified.

10.3.2 Thickness of the opal as a function of height

The thickness of opals grown from a dispersion with a volume fraction of Φ_i = 0.05% v/v is shown in figure 10.4 A. The opals start to grow at the initial dispersion level, at z = 2 mm. The figure shows that the opals become thicker with increasing z, that is, near the bottom of the substrate. The thickness profiles that we measured are found to be independent of temperature. We observe that the thickness of each sample is not homogeneously distributed: The thickness is strongly dependent on the position on the sample. We therefore recommend that the thickness is measured for several positions on a sample, as an improvement of the commonly performed characterization of only one thickness measurement.

We know the initial volume fraction of the dispersion Φ_i and we may assume that the amount of crystallized spheres is negligible with respect to the amount left in the

dispersion. In this case the volume fraction of spheres in the solution is doubled, if half of the amount solvent has evaporated. We have assumed a linear relation between the thickness of the crystal and the volume fraction, as proposed in [139]. Therefore, the height-dependent thickness profile is taken to be

$$d(z) = d_0 \frac{10 - z_0}{10 - z} \times \frac{\Phi_i}{\Phi_0}, \tag{10.4}$$

where d is the thickness of the crystal, d_0 is the thickness of the crystal at the start position of the crystal growth and z_0 is the z-position on the substrate where the crystallization started. In the case of figure 10.4 A, z_0 is equal to 2.5 mm and d_0 is equal to 1.1 μm. The resulting curve is plotted in figure 10.4 A and overlaps the data points excellently for all temperatures.

Figure 10.4 B shows the measured thickness for samples grown with an initial volume fraction of $\Phi_i = 0.10\%$. We see that the thickness profiles are strikingly independent of temperature. The data shows the same trend as the data from figure 10.4 A: An increase of thickness towards the bottom of the substrate is observed, and the thickness of the opal is not constant. The model curve is the curve from figure 10.4 A scaled with the ratio of the initial bulk volume fractions Φ_i as given by Eq. 10.4. The data show a very good agreement with the curve from Eq. 10.4, with only a slight deviation for small and large thicknesses.

Figure 10.4 C shows the thickness measurements for two samples grown from dispersions with an initial volume fraction of $\Phi_i = 0.20\%$, at two different temperatures. The z-position of the 303 K data was scaled with the initial volume with respect to the 309 K curve, since the initial dispersion volume was less. Also for this volume fraction the thickness increases with z-position and is independent of temperature. For the model no extra parameters are used. Only the ratio of the initial volume fraction is taken to be Φ_i = 0.20 %. With increasing z, the measured thickness becomes larger than the thickness predicted by Eq. 10.4.

Equation 10.4 holds very well for a volume fraction of $\Phi_i = 0.05\%$ (figure 10.4 A) and for $\Phi_i = 0.10\%$ (figure 10.4 B). The validity of Eq. 10.4 suggests that the volume fraction in either the dispersion or in the meniscus is homogeneous. The increase in volume fraction near the meniscus by the collection of spheres at the meniscus is canceled by the concentration driven diffusion of spheres from the meniscus to the bulk. The curve from Eq. 10.4 agrees for z between 2 mm and 4 mm with the data for a high initial

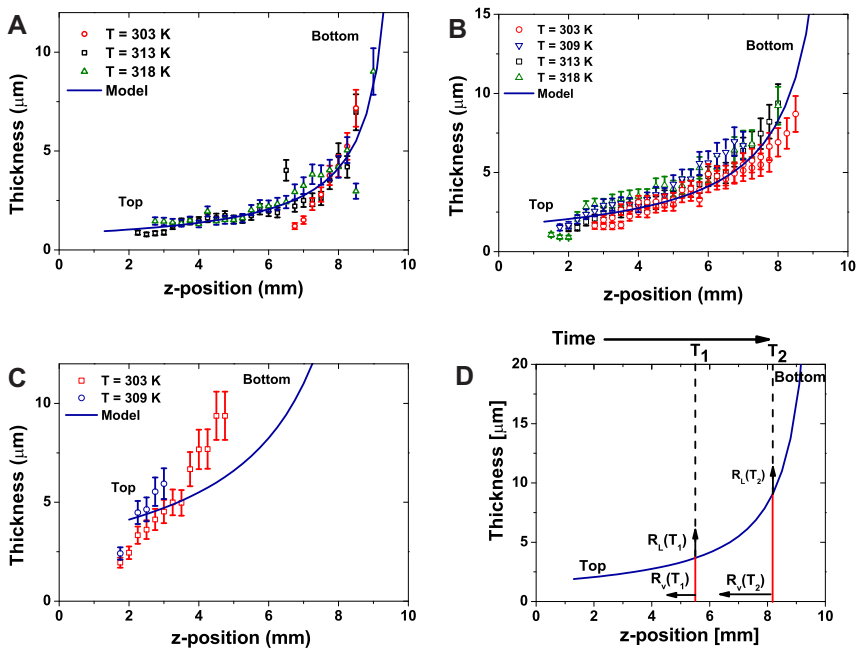

FIGURE 10.4: *(A) Thickness of opals as a function of the z-position on the sample. The opals were grown at different temperatures from dispersions with a volume fraction of 0.05 % (A), 0.10 % (B) and 0.20 % (C). The blue curve represents the model given by equation 10.4. A very good agreement between the theoretical curve and the measured data is observed. An increase in thickness towards the bottom of the sample is observed. (D) Schematic thickness as a function of z-position and time . The vertical lines in the graph indicate the thickness of the crystal at times T_1 and T_2 respectively. R_v and R_l are the vertical and lateral evaporation rates respectively.*

volume fraction $\Phi_i = 0.20\%$ (figure 10.4 C). For larger z the measured thickness is larger than predicted with Eq. 10.4. This observation suggests that there is a larger flow of spheres to the substrate in the case of higher concentration than in the case of lower concentration. The larger flow might be caused by an accumulation of spheres near the meniscus at the air/solvent interface. The reason could be the changed equilibrium of the dispersion dynamics at increased particle density.

10.3.3 Drying and domain formation

Figure 10.5 shows the domain size as a function of thickness for samples grown at five different temperatures, ranging from 298 K to 318 K. Figure 10.5 shows that the average domain size increases linearly with thickness. The total number of data points shown is 300, of which only nine deviate from the linear trend depicted by the orange line. The ratio between the average domain size and the thickness of the thin-film opal is 2.5; This means that on average the opal domains formed on the substrate are 2.5 times wider than thick. We propose that the origin of the linear relation between the average domain size and the thickness might lie in the viscous behavior of the opal layer during the drying process. Forces work at the air wet-opal interface during the drying process and are distributed linearly through the wet layer. If this is the case, the force per unit thickness is inversely proportional to the thickness. If we furthermore assume that there is some force proportional to the perimeter of the domain preventing domain formation, it would follow that the domain size increases with thickness in the case of a viscous layer. The consequences for optical measurements are discussed in section 10.3.5.

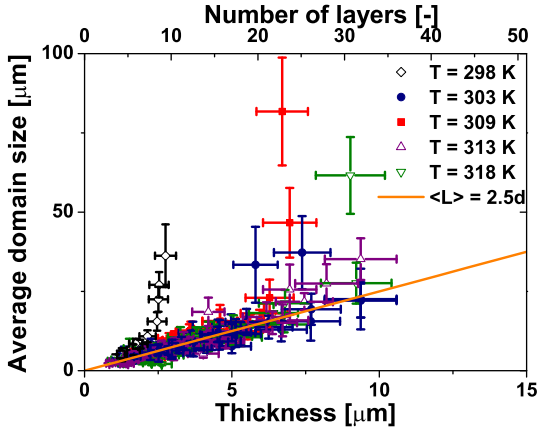

FIGURE 10.5: *Average domain size of opals synthesized at different temperatures and volume fractions as a function of the thickness of the opal, for a total 300 data points. The average domain of an opal is 2.5 time wider than thick. All data points from samples grown at the same temperature have the same color.*

The domain size to thickness ratio of 2.5 can be compared to values in literature. The linear relation that we found agrees with previous results on completely different colloid systems [150]. A ratio between 3.75 and 6.25 was found for layers of an alumina/water slurry [150]. The higher ratio was obtained by using a smoother substrate to reduce the friction between the opal layer and the substrate. Reducing the number of impurities also increases the ratio. We estimated a ratio of 1.5 from data on directional drying of silica particles up to 10 nm in radius [149]. Our results show that the linear relation between domain size and thickness also holds if colloidal spheres crystallize while the dispersion dries. Finally, our observation that crack formation occurs at all thicknesses, including those smaller than 10 μm, contradicts the results of [155] for currently unknown reasons.

Figure 10.6 A shows domains near the top of the substrate at a height z = 5.5 mm. The domains at these positions are very irregularly shaped. The crystal at both sides of the cracks have the same crystal orientation and the domains fit each other like pieces of a jigsaw puzzle despite their irregular shape. This appearence has been observed earlier [139]. Figure 10.6 B shows a scanning electron microscope image of the crystal nearer to the bottom, i.e., at a height of z = 8.25 mm. It can be seen that the domains are rectangular shaped and surrounded with large cracks parallel to the growth direction, which is from top to bottom in the figure.

The difference in domain shape has been investigated by Shorlin *et al.* and indicates a different drying mechanism: Irregularly shaped domains in drying films are found in isotropic drying, while the rectangular shaped domains accompanied by large vertical cracks are a signature of directional drying [150]. This suggests that directional drying is dominant at the bottom of the samples where we find the larger rectangular shaped domains. On the other hand, the crystal dries isotropically at the top of the sample. This can be understood if we also take the thickness of the samples into account as shown in figure 10.4 D: The crystal has two perpendicular interfaces with the air surrounding it. The first one is horizontal and perpendicular to the growth direction, and is indicated in figure 10.4 D with vertical lines. This interface becomes larger when the crystal becomes thicker. The vertical line in figure 10.4 D at time T_1 and the one at later time T_2 illustrate this feature. The vertical evaporation rate R_v increases with time because of the increase of the vertical interface. The second interface is a vertical surface parallel to the growth direction and the substrate. This surface remains constant through the drying process and moves downward, therefore the lateral evaporation rate R_l is constant in time, as indicated by equal lengths for R_2 at time T_1 and R_2 at time T_2 in figure 10.4 D.

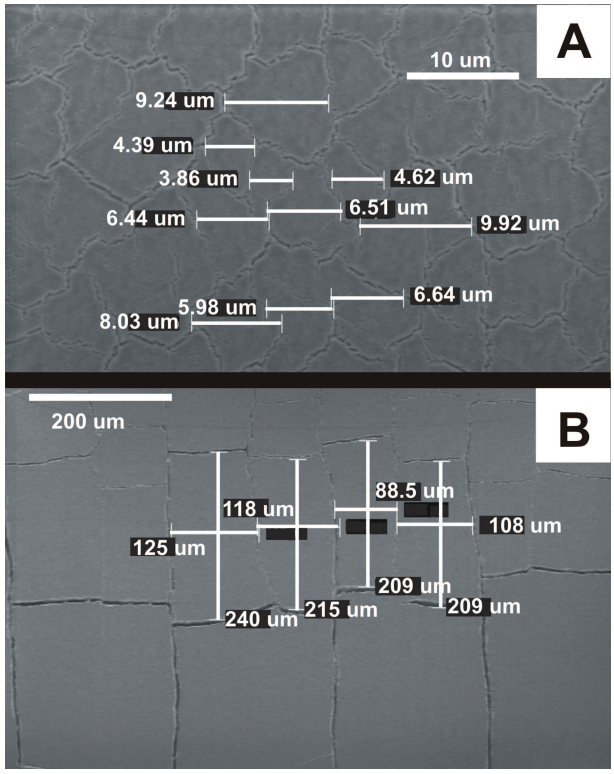

FIGURE 10.6: *(A) Scanning electron micrograph of an opal at a z-position of z = 5.5 mm. The crystal domains can clearly be distinguished. The domains are shaped irregular near the top of the crystal, which indicates isotropic drying. The growth direction of the crystal is from top to bottom. (B) Scanning electron micrograph of an opal at a z-position of z = 8.25 mm. The crystal domains can clearly be distinguished. The domains are shaped rectangular near the bottom of the crystal, which indicates directional drying. The growth direction of the crystal is from top to bottom.*

If we consider a piece of wet crystal at the top (T_1), figure 10.4 D shows that the ratio between horizontal and vertical surface is smaller than in the case of a piece of wet crystal at the bottom of the substrate (T_2). Therefore, the ratio of R_v and R_l is smaller at the top of the sample than at the bottom of the sample. This means that at the bottom of the sample the total evaporation speed is dominated by the vertical evaporation rate R_v; The crystal dries directionally in this area. At the top of the sample the lateral evaporation rate R_l is larger, which results in isotropic drying at the top of the sample. Furthermore, the sum of the interfacing surface between air and wet crystal increases towards the bottom

of the substrate, which means that the evaporation speed is faster at the bottom of the crystal, thus giving the spheres less time to organize themselves. This effect becomes even stronger since there are more spheres that need to be ordered.

We conclude that the crystal dries isotropically at the top of the sample, while it dries directional at the bottom of the sample. Furthermore, we have shown that drying phenomena known from disordered structures [149, 150, 155] also apply to ordered structures. This fact gives us the possibility to conclude that a smoother substrate will lead to crystals with larger domains than the ones we have presented in this chapter [149, 150, 155].

10.3.4 Domain size of the opal as a function of height

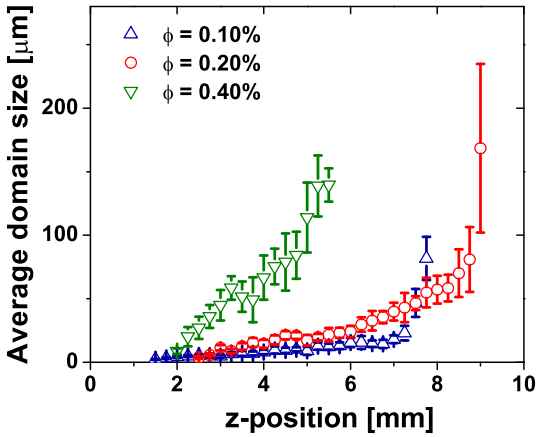

FIGURE 10.7: *Average domain size of opals grown at different volume fractions at T = 309 K as a function of the z-position on the sample. An increase of average domain size towards the bottom of the substrate is observed for all three volume fractions.*

Figure 10.7 shows the average domain size as a function of the z-position for three different samples all grown at 309 K. The initial volume fraction of the three samples was varied. Figure 10.7 shows an increase of domain size with z-position. The largest domains with sizes up to 150 μm can be found at the bottom of the sample. The sample grown at an initial volume fraction of $\Phi_i = 0.40\%$ was damaged due to tension built up during drying so that no more crystal domains were present on the substrate above $z = 6$

mm. A comparison with other samples showed no effect of temperature on the domain size profile. We again observe that the size of the different domains on each sample is inhomogeneous: The size of the domain is strongly dependent on the position on the sample. Therefore, we recommend that the position is also mentioned when data on domain sizes are shown.

10.3.5 Consequences for photonic crystals

For photonic crystals domains are required that are as large as possible combined with a controlled thickness. Our results show that the possible combinations are limited. Since the ratio of thickness and domain size is fixed, this means that the density of grain boundaries is related to the opal thickness. The grain boundaries increase unwanted extinction of light, since the boundaries contribute to the scattering of light out of the coherent beam. The extinction due to scattering from grain boundaries is therefore fixed for each thickness. This means that there is an upper limit to the reflectivity measured in the stopgaps if the focus of the light beam is larger than a crystal domain. This in turn means that there is a lower limit to the range of thicknesses for which the scattering from grain boundaries can be reduced to zero, given a certain focal size of the light beam. The latter being in the order of 1 μm to 30 μm, the typical domain size.

The quality of the opal is likely to be influenced by the drying regime. If the isotropic drying process yields better crystals, there will be an upper limit (around 5 μm) to the thickness of a good crystal, according to figure 10.4 D. If directional drying yields better crystals, there will be a lower limit to the thickness of a good crystal (around 5 μm). To be able to give a prediction about the quality of opals formed in either the two drying regimes, we assume the following mechanism: The spheres self-assembly in a close packed order at the wet crystal-air interfaces, the spheres below the upper layer organize themselves to form another closed packed layer. The second step was discussed by Norris *et al.* [145]. The assumed mechanism suggests that the quality of the crystal in the direction perpendicular to the wet crystal-air interface is higher than in another direction, because the spheres order themselves according to the first crystal layer that formed at the wet-crystal air interface. Therefore, we predict that the quality will be better for films formed in the isotropic drying regime for measurements on the <111>-planes of the crystal, which lie parallel to the substrate.

10.3.6 Relative linewidth as a function of number of layers

An interesting source of information about the photonic crystals is the relative linewidth of the reflectivity peak of the first order stopband. The relative linewidth can be obtained from the spectrum shown in figure 10.2 and is equal to $\frac{\Delta\omega}{\omega_0}$. For thick crystals in absence of structural defects the relative linewidth is equal to the photonic strength S, for thin crystals, however, finite size effects play a role [159]. The relative linewidth of a real photonic crystal can be approximated with

$$\left(\frac{\Delta\omega}{\omega_0}\right)_{meas} = \sqrt{\left(\frac{\Delta\omega}{\omega_0}\right)^2_{phot} + \left(\frac{\Delta\omega}{\omega_0}\right)^2_{fin}}. \tag{10.5}$$

Where $\left(\frac{\Delta\omega}{\omega_0}\right)_{meas}$ is the relative linewidth that is determined from the reflectivity spectrum, $\left(\frac{\Delta\omega}{\omega_0}\right)_{fin}$ is the contribution due to the finite size of the crystal, and $\left(\frac{\Delta\omega}{\omega_0}\right)_{phot}$ is the photonic part of the relative linewidth, given by the photonic strength S. The contribution of the

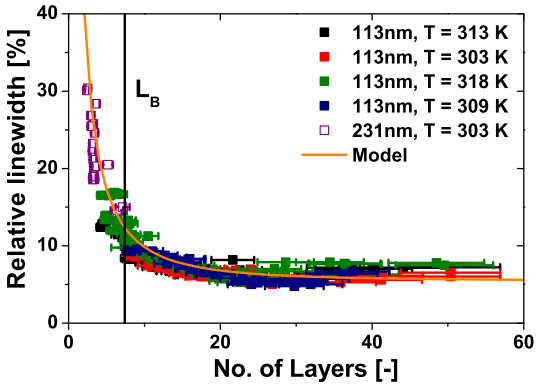

FIGURE 10.8: *Measured and calculated relative linewidth as function of number of layers for opals with 113 nm spheres and 231 nm spheres. The data are measured on samples grown at four different temperatures with volume fractions of 0.05%, 0.10% and 0.20%. The solid curve is calculated with a model taken from X-ray diffraction. The data and the calculated curve show both a qualitatively agreement. The relative linewidth decreases with the number of layers as expected.*

photonic strength to the relative linewidth $\left(\frac{\Delta\omega}{\omega_0}\right)_{phot}$ is given by

$$\left(\frac{\Delta\omega}{\omega_c}\right)_{phot} = S = 3\Phi\frac{m^2-1}{m^2+2}g(K,r), \tag{10.6}$$

where Φ is the volume fraction of high index material, m is the ratio of the refractive indices and $g(K,r)$ is the structure factor [17, 18].

The contribution of the finite size of the crystal $\left(\frac{\Delta\omega}{\omega_0}\right)_{fin}$ can be calculated for a crystal without absorption from the Scherrer-equation [126]:

$$\left(\frac{\Delta\omega}{\omega_c}\right)_{fin} = \sqrt{\frac{log(2)}{\pi}} \cdot \frac{2 \cdot n_{eff}}{N}, \tag{10.7}$$

where N is the number of crystal layers, and n_{eff} is the mean refractive index, which is given by $n_{eff} = (1-\phi)n_l + \phi n_h$.

The relative linewidth that results from inserting Eq. 10.7 and Eq. 10.6 into Eq. 10.5 is plotted in figure 10.8 as a function of the number of crystal layers. The number of layers is calculated from the thickness of the crystal by dividing the thickness through the spacing of the d_{111} planes. The distance between the planes depends on the radius of the spheres and is therefore larger for 231 nm spheres than for 113 nm spheres.

Figure 10.8 shows a very good agreement between the model and the measured data points. At larger number of layers the measured points deviate slightly from the model, which is also the case for the opals measured in [147]. There is an optimum, minimum, linewidth between 20 and 30 layers. We will discuss this in the next section.

10.3.7 Reflectivity versus thickness

Figure 10.9 shows the reflectivity of the $\Gamma - L$ gap (R_{sb} in figure 10.2) versus thickness for samples grown with a dispersion with a volume fraction of $\Phi_i = 0.10\%$. The solid curve is calculated with

$$R = 100\%(1 - e^{\frac{L}{L_B}}). \tag{10.8}$$

Where L is the thickness of the crystal, L_B is the Bragg length. The thickness is derived from the fringes in the measured spectra. The Bragg length, L_B can be calculated using

$$L_B = \frac{2d}{\pi S}, \tag{10.9}$$

where d is the spacing between two crystal planes, and S is the so-called photonic strength, which is given by equation 10.6.

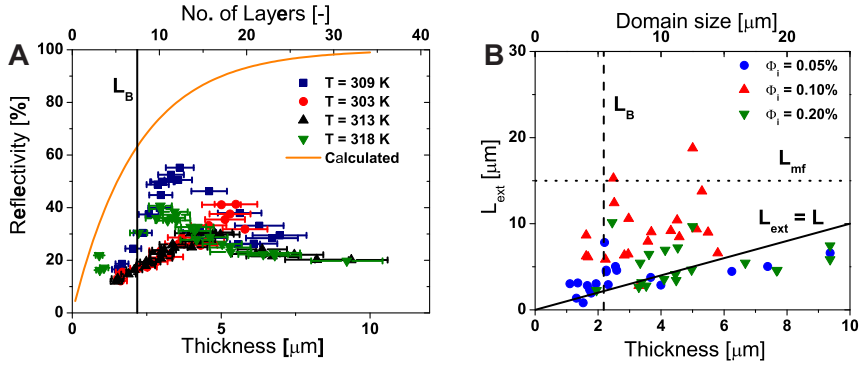

FIGURE 10.9: *(A) Measured and calculated reflectivity of the opal due to the $\Gamma - L$ stopband versus the number of layers of the crystal. The samples are grown at four different temperatures with a dispersion with a volume fraction of Φ_i = 0.10%. The solid curve represents the theoretical expected relation for a crystal with a Bragg length of 2.18 μm. The measured reflectivity shows a maximum value while the calculated curve increases with the number of crystal layers. (B) Extinction length of photonic crystals grown at 303 K as a function of thickness and domain size of the crystal. The crystals are grown with three different initial concentrations. The solid line gives the line at which the thickness is equal to the extinction length. The dashed line represents the Bragg length L_B and the dotted line the mean free path measured for opals L_{mf} [19].*

Figure 10.9 A shows that the reflectivity data from the four different samples have the same behavior. The reflectivity increases as a function of the number of layers to a maximum value after which it decreases again. The number of layers at which there is a maximum reflectivity differs per sample but it is found to be between 20 and 30 layers. There is a difference between the calculated curve (Eq. 10.8) and the measured data points in figure 10.9 A. We can distinguish two regimes. The first regime is for thicknesses lower than the maximum of the datasets. The second regime is after this maximum. In the first regime the measured data points deviate from the calculated values, but they show similar behavior. The trend is an increasing reflectivity with increasing thickness as expected. In the second regime the data points deviate not only in absolute value but also in trend. Figure 10.9 A shows that the reflectivity appears to converge to a value of about 20 % for

all samples. To find the origin of this deviation we will examine the relation between the extinction length, thickness, and reflectivity in the next section.

10.3.8 Extinction length and reflectivity

In the previous sections we showed the difference between the expected and measured reflectivity. We only took the thickness of the sample into account and not extinction of light inside the crystal. In figure 10.9 B we present the relation between the extinction length, thickness, and domain size. We have also plotted the Bragg length and the measured mean free path [19]. Furthermore, we plotted the line were the thickness is equal to the extinction length. Figure 10.9 B shows that the majority of the samples is thicker than the Bragg length, as we have seen in figure 10.9 A. Furthermore, we see that the thickness is smaller than the extinction length. If the extinction length would be smaller than the thickness, we are not be able to measure the extinction length since there would be no Fabry-Pérot fringes in the spectrum. The third line in the figure 10.9 B is the mean free path as measured in bulk opals [19]. Comparison with our data shows first of all that the extinction length is not constant as is the mean free path. Furthermore, the extinction length that we find is smaller than the one found in bulk opals, indicating that there is a larger amount of disorder present in the thin-film opals.

On the two horizontal axis of figure 10.9 B we show the two spatial parameters of the crystal: the thickness and the domain size. These two axis contain all three-dimensional information about the crystal. We used the fact that the domain size of the crystal is proportional to the thickness of the crystal. The extinction length is fluctuating but we do not see a steady increase or decrease but rather an increase followed by a decrease. Since the domain size increases with thickness there are less cracks per unit area, which decreases scattering losses and thereby increases the scattering length. This is clearly visible for a thickness up to 5 μm where the domain size is up to 12 μm. Since the thicker layers are found at the bottom of the sample we attribute the decrease in extinction length for layers thicker than 5 μm to the difference in growth mechanisms at the top and bottom of the sample as discussed in section 10.3.3. The different growth mechanism at the bottom creates more defects and irregularities in the structure, which leads to a shorter extinction length. Figure 10.9 B shows that there is a correlation between the extinction length and the reflectivity of the stopband as expected: if the extinction length increases, the stopband reflectivity increases. We conclude from figure 10.9 B that the best crystals

are grown at the top, where the solvent evaporates mainly perpendicular to the crystal surface.

Figure 10.9 B shows that the extinction length is about one to five times the Bragg length, which is $L_B = 2\ \mu m$. One has to keep in mind that the extinction length gives the extinction of the field and that the light covers twice the thickness when it is reflected. This means that the reflectivity decreases significantly even if the extinction length is only a half or a fourth of the thickness. An extinction length much larger than the Bragg length is favorable.

10.4 Conclusion

We have grown thin-film opals by vertical controlled drying while systematically varying temperature and initial volume fraction. We have measured the thickness of the resulting opals. The thickness increases with z-position, independent of temperature. The thickness profile agrees with a simple model for thickness variation with colloid density.

We have investigated the lateral size of crystal domains of the grown opals. We found that the domain size increases with z-position. We found a surprisingly linear relation between the lateral domain size and the crystal thickness. The ratio between the domain size and the thickness is found to be 2.5. It is interesting to see that the drying behavior is similar to the behavior of drying slurries of polydisperse particles. We compared the obtained domain-size-to-thickness ratio with literature and concluded that a smoother substrate will increase the ratio yielding larger crystal domains. We identified two sample-regions with different drying behavior. We proposed a qualitative explanation of the drying mechanism of self assembled photonic crystals grown with vertical controlled drying.

We conclude that the structural properties of a thin film opal photonic crystal are inhomogeneous. Therefore, we recommend that the position at which the characteristics are measured is given as well. The thickness profile is easily determined with the thickness at a certain position, by using the functional relation presented.

Finally, our data show that the lateral domain size increases with increasing thickness of the crystal. Therefore, in photonic applications grain boundary induced scattering of light is reduced for thick crystals and is prominent for thin crystals. We find this in our optical measurements. However, from our optical measurements we also observe that the extinction length depends on the growth regime of the crystal. At the bottom the

extinction length decreases due to the different growth mechanism, despite the increase in domain size and thereby the decrease in grain boundary induced scattering.

References

[1] K. J. Vahala, Optical microcavities, Nature **424**, 839–846 (2003). — p.1 and 13.

[2] S. F. Preble, Q. Xu, and M. Lipson, Changing the colour of light in a silicon resonator, Nat. Phot. **1**, 293–296 (2007). — p.1, 4, 16, 29, 30, 39, 44, 71, 72, and 77.

[3] J. P. Reithmaier, S. Sek, A. Loffler, C. Hofmann, S. Kuhn, S. Reitzenstein, L. V. Keldysh, V. D. Kulakovskii, T. L. Reinecke, and A. Forchel, Strong coupling in a single quantum dot-semiconductor microcavity system, Nature **432**, 197–200 (2004). — p.1, 4, 9, 13, 29, 30, 79, 110, and 111.

[4] T. Yoshie, A. Scherer, J. Hendrickson, G. Khitrova, H. M. Gibbs, G. Rupper, C. Ell, O. B. Shchekin, and D. G. Deppe, Vacuum Rabi splitting with a single quantum dot in a photonic crystal nanocavity, Nature **432**, 200–203 (2004). — p.1, 4, 13, 29, and 30.

[5] E. Peter, P. Senellart, D. Martrou, A. Lemaître, J. Hours, J. M. Gérard, and J. Bloch, Exciton-photon strong-coupling regime for a single quantum dot embedded in a microcavity, Phys. Rev. Lett. **95**, 067401 (2005). — p.1 and 13.

[6] A. Lagendijk, *Vibrational relaxation studied with light,* in: *Ultrashort Processes in Condensed Matter, Edited by W. E. Bron*, Plenum, New York, 1993. — p.1, 4, 12, 30, 38, and 99.

[7] T. Savels, *Scattering lasers,* University of Twente, available online: http://www.randomlasers.com, PhD thesis, 2007. — p.2 and 111.

[8] R. P. Feynman, R. B. Leighton, and M. Sands, *The Feynman Lectures on Physics Vol. II*, Addison Wesley, 1964. — p.3 and 29.

[9] J. A. Hart, T. M. Antonsen, Jr., and E. Ott, Scattering a pulse from a chaotic cavity: Transitioning from algebraic to exponential decay, Phys. Rev. E **79**, 016208 (2009). — p.3 and 30.

[10] T. Asano, B.-S. Song, and S. Noda, Analysis of the experimental Q factors (~ 1 million) of photonic crystal nanocavities, Opt. Express **14**, 1996–2002 (2006). — p.3, 4, and 30.

[11] J. M. Gérard, B. Sermage, B. Gayral, B. Legrand, E. Costard, and V. Thierry-Mieg, Enhanced Spontaneous Emission by Quantum Boxes in a Monolithic Optical Microcavity, Phys. Rev. Lett. **81**, 1110–1113 (1998). — p.4, 13, 30, 79, 97, 103, 104, 108, 111, 112, 113, and 116.

[12] T. Yoshie, J. Vučković, A. Scherer, H. Chen, and D. Deppe, High quality two-dimensional photonic crystal slab cavities, Appl. Phys. Lett. **79**, 4289 (2001). — p.4 and 30.

[13] P. J. Harding, T. G. Euser, Y. R. Nowicki-Bringuier, J.-M. Gérard, and W. L. Vos, Ultrafast optical switching of planar GaAs/AlAs photonic microcavities, Appl. Phys. Lett. **91**, 111103 (2007). — p.4, 14, 19, 30, 34, 39, 40, 46, 52, 53, 64, 65, 72, 79, 98, 101, and 102.

[14] W. Demtröder, *Laser Spektroskopie*, Springer Berlin, 1996. — p.4 and 30.

[15] R. W. James, *The optical principles of diffraction of x-rays*, G. Bell and Sons, London, 1958. — p.5 and 119.

[16] W. L. Vos, R. Sprik, A. v. Blaaderen, A. Imhof, A. Lagendijk, and G. H. Wegdam, Strong effects of photonic band structures on the diffraction of colloidal crystals, Phys. Rev. B **53**, 16231–16235 (1996). — p.6, 157, and 159.

[17] W. L. Vos, H. M. v. Driel, M. Megens, A. F. Koenderink, and A. Imhof, *Experimental probes of the optical properties of photonic crystals*, 2001. — p.6 and 142.

[18] R. Spry and D. Kosan, Theoretical Analysis of the Crystalline Colloidal Array Filter, Appl.Spectroscopy **40**, 782 (1986). — p.6, 142, and 159.

[19] A. F. Koenderink, *Emission and Transport of Light in Photonic Crystals,* University of Amsterdam, available online: http://www.photonicbandgaps.com, PhD thesis, 2003. —

p.6, 100, 143, and 144.

[20] J. M. Gérard, D. Barrier, J. Y. Marzin, and T. Rivera, Quantum boxes as active probes for photonic microstructures: The pillar microcavity case, Appl. Phys. Lett. **69**, 449–451 (1996). — p.6, 7, 9, 18, 19, 79, 88, 91, 110, 111, and 112.

[21] J. D. Joannopoulos, S. G. Johnson, J. N. Winn, and R. D. Meade, *Photonic Crystals - Molding the Flow of Light*, 2008. — p.7 and 8.

[22] R. P. Stanley, R. Houdré, U. Oesterle, M. Ilegems, and C. Weisbuch, Impurity modes in one-dimensional periodic systems: The transition from photonic band gaps to microcavities, Phys. Rev. A **48**, 2246–2250 (1993). — p.7.

[23] A. Farjadpour, J. D. Joannopoulos, S. G. Johnson, and G. Burr, improving accuracy by subpixel smoothing in FDTD, Opt. Lett. **31**, 2972–2974 (2006). — p.8 and 32.

[24] T. G. Euser, *Ultrafast optical switching of photonic crystals,* University of Twente, available online: http://www.photonicbandgaps.com, PhD thesis, 2007. — p.9, 14, 20, 22, 23, 25, 40, 61, and 98.

[25] G. Khitrova, H. M. Gibbs, M. Kira, S. W. Koch, and A. Scherer, Vacuum Rabi splitting in semiconductors, Nature Phys. **2**, 81–90 (2006). — p.9, 10, and 110.

[26] A. Yariv, *Optical Electronics in Modern Communications*, Oxford University Press, Oxford, 5 edition, 1997. — p.9, 83, 84, 85, 92, and 93.

[27] M. Bayer, T. L. Reinecke, F. Weidner, A. Larionov, A. McDonald, and A. Forchel, Inhibition and Enhancement of the Spontaneous Emission of Quantum Dots in Structured Microresonators, Phys. Rev. Lett. **86**, 3168–3171 (2001). — p.9, 13, 81, and 110.

[28] S. Reitzenstein, C. Hofmann, A. Gorbunov, M. Strauss, S. H. Kwon, C. Schneider, A. Löffler, S. Höfling, M. Kamp, and A. Forchel, AlAs/GaAs micropillar cavities with quality factors exceeding 150.000, Appl. Phys. Lett. **90**, 251109 (2007). — p.9, 10, and 110.

[29] T. Thomay, T. Hanke, M. Tomas, F. Sotier, K. Beha, V. Knittel, M. Kahl, K. M. Whitaker, D. R. Gamelin, A. Leitenstorfer, and R. Bratschitsch, Colloidal ZnO quantum dots in ultraviolet pillar microcavities, Opt. Express **16**, 9791–9794 (2008). — p.10 and 110.

[30] E. Yablonovitch, Inhibited Spontaneous Emission in Solid-State Physics and Electronics, Phys. Rev. Lett. **58**, 2059–2062 (1987). — p.11.

[31] S. Ogawa, M. Imada, S. Yoshimoto, M. Okano, and S. Noda, Control of light emission by 3D photonic crystals, Science **305**, 227–229 (2004). — p.11.

[32] M. Qi, E. Lidorikis, P. T. Rakich, S. G. Johnson, J. D. Joannopoulos, E. P. Ippen, and H. I. Smith, A three-dimensional optical photonic crystal with designed point defects, Nature **429**, 538–542 (2004). — p.11.

[33] L. A. Woldering, A. M. Otter, B. H. Husken, and W. L. Vos, Focused ion beam milling of nanocavities in single colloidal particles and self-assembled opals, Nanotechnology **17**, 5717–5721 (2006). — p.11 and 128.

[34] L. A. Woldering, *Fabrication of photonic crystals and nanocavities,* University of Twente, available online: http://www.photonicbandgaps.com, PhD thesis, 2008. — p.11 and 12.

[35] R. Loudon, *The quantum theory of light*, Oxford University Press, 2nd edition, 1983. — p.12, 97, and 99.

[36] D. Kleppner, Inhibited spontaneous emission, Phys. Rev. Lett. **47**, 233–236 (1981). — p.12 and 97.

[37] S. Haroche and D. Kleppner, Cavity Quantum Electrodynamics, Phys. Today **42**, 24–30 (1989). — p.12 and 97.

[38] E. Fermi, Quantum Theory of Radiation, Rev. Mod. Phys. **4**, 87–132 (1932). — p.12, 97, and 99.

[39] I. S. Nikolaev, *Spontaneous-emission rates of quantum dots and dyes controlled with photonic crystals,* University of Twente, available online: http://www.photonicbandgaps.com, PhD thesis, 2006. — p.12, 98, and 99.

[40] A. F. v. Driel, I. S. Nikolaev, P. Vergeer, P. Lodahl, D. Vanmaekelbergh, and W. L. Vos, Statistical analysis of time-resolved emission from ensembles of semiconductor quantum dots: Interpretation of exponential decay models, Phys. Rev. B **75**, 035329 (2007). — p.12, 79, and 100.

[41] E. M. Purcell, Spontaneous emission probabilities at radio frequencies, Phys. Rev. **69**, 681 (1946). — p.12.

[42] M. A. Nielsen and I. L. Chuang, *Quantum computation and quantum information*, Cambridge University Press, Cambridge, 2000. — p.13.

[43] P. M. Johnson, A. F. Koenderink, and W. L. Vos, Ultrafast switching of photonic density of states in photonic crystals, Phys. Rev. B **66**, 081102 (2002). — p.13, 15, 39, 51, 52, and 53.

[44] K. Sokolowski-Tinten and D. von der Linde, Generation of dense electron-hole plasmas in silicon, Phys. Rev. B **61**, 2643–2650 (2000). — p.14.

[45] L. Huang, J. P. Callan, E. N. Glezer, and E. Mazur, GaAs under Intense Ultrafast Excitation: Response of the Dielectric Function, Phys. Rev. Lett. **80**, 185 (1998). — p.14.

[46] T. G. Euser, H. Wei, J. Kalkman, Y. Jun, A. Polman, D. J. Norris, and W. L. Vos, Ultrafast optical switching of three-dimensional Si inverse opal photonic band gap crystals, J. Appl. Phys. **102**, 053111 (2007). — p.14, 51, 102, 123, and 124.

[47] T. G. Euser, A. J. Molenaar, J. G. Fleming, B. Gralak, A. Polman, and W. L. Vos, All-optical octave-broad ultrafast switching of Si woodpile photonic band gap crystals, Phys. Rev. B **77**, 115214 (2008). — p.14, 27, 51, and 102.

[48] R. Boyd, *Nonlinear Optics*, Academic Press, 1992. — p.14, 16, 52, 53, and 67.

[49] M. Sheik-Bahae, D. J. Hagan, and E. W. V. Stryland, Dispersion and Band-Gap Scaling of the Electronic Kerr Effect in Solids Associated with Two-Photon Absorption, Phys. Rev. Lett. **65**, 96 (1991). — p.14, 61, and 67.

[50] A. Hartsuiker, P. J. Harding, Y.-R. Nowicki-Bringuier, J.-M. Gérard, and W. L. Vos, Kerr and free carrier ultrafast all-optical switching of GaAs/AlAs nanostructures near the three photon edge of GaAs, J. Appl. Phys. **104**, 083105 (2008). — p.14, 40, 46, 48, 65, and 86.

[89] P. J. Harding, T. G. Euser, and W. L. Vos, Identification of competing ultrafast all-optical switching mechanisms in Si woodpile photonic crystals, J. Opt. Soc. Am. B **26**, 610 (2009). — p.14, 40, 44, 53, and 61.

[52] O. Raz, J. Herrera, and H. J. S. Dorren, Enhanced 40 and 80 Gb/s wavelength conversion using a rectangular shaped optical filter for both red and blue spectral slicing, Opt. Express **17**, 1184 (2009). — p.15.

[53] M. W. McCutcheon, A. G. Pattantyus-Abraham, G. W. Rieger, and J. F. Young, Emission spectrum of electromagnetic energy stored in a dynamically perturbed optical microcavity, Opt. Express **15**, 11472 (2007). — p.16, 72, and 77.

[54] T. Tanabe, M. Notomi, H. Taniyama, and E. Kuramochi, Dynamic Release of Trapped Light from an Ultrahigh-Q Nanocavity via Adiabatic Frequency Tuning, Phys. Rev. Lett. **102**, 043907 (2009). — p.16, 72, and 77.

[55] J.-C. Diels and W. Rudolph, *Ultrashort Laser Pulse Phenomena: Fundamentals, Techniques, and Applications on a Femtosecond Time Scale*, Academic press, Burlington, 2 edition, 1996. — p.16, 25, 27, 31, and 100.

[56] L. A. Woldering, R. W. Tjerkstra, H. V. Jansen, I. D. Setija, and W. L. Vos, Periodic arrays of deep nanopores made in silicon with reactive ion etching and deep UV lithography, Nanotechnology **19**, 145304–11 (2008). — p.17 and 18.

[57] K. M. Ho, C. T. Chan, C. M. Soukoulis, R. Biswas, and M. Sigalas, Photonic band gaps in three dimensions: New layer-by-layer periodic structures, Solid State Commun. **89**, 413–416 (1994). — p.17 and 121.

[58] A. Hartsuiker and W. L. Vos, Structural Properties of Opals Grown with Vertical Controlled Drying, Langmuir **24**, 4670–4675 (2008). — p.18.

[59] P. J. Harding, *Photonic Crystals Modified by Optically Resonant Systems,* University of Twente, available online: http://www.photonicbandgaps.com, PhD thesis, 2008. — p.19, 25, 41, 43, and 103.

[60] A. Molenaar, Ultrafast optical switching of woodpile photonic crystals, Master's thesis, 2006. — p.20 and 22.

[61] M. S. Thijssen, R. Sprik, J. E. G. J. Wijnhoven, M. Megens, T. Narayanan, A. Lagendijk, and W. L. Vos, Inhibited Light Propagation and Broadband Reflection in Photonic Air-Sphere Crystals, Phys. Rev. Lett. **83**, 2730–2733 (1999). — p.21 and 129.

[62] C. F. Bohren and D. R. Huffman, *Absorption and scattering of light by small particles*, Wiley-VCH, 1983. — p.21, 22, and 159.

[63] M. J. A. d. Dood, B. Gralak, A. Polman, and J. G. Fleming, Superstructure and finite-size effects in a Si photonic woodpile crystal, Phys. Rev. B **67**, 035322 (2003). — p.22.

[64] T. G. Euser, P. J. Harding, and W. L. Vos, Broadband sensitive pump-probe setup for ultrafast optical switching of photonic nanostructures and semiconductors, Rev. Sci. Instrum. , Accepted (2009). — p.25, 27, and 73.

[65] B. H. Husken, *Spontaneous Emission of Near-Infrared Quantum Dots Controlled with Photonic Crystals,* University of Twente, available online: http://www.photonicbandgaps.com, PhD thesis, 2009. — p.28.

[66] T. Tanabe, M. Notomi, E. Kuramochi, A. Shinya, and H. Taniyama, Trapping and delaying photons for one nanosecond in an ultrasmall high-Q photonic-crystal nanocavity, Nat. Phot. **1**, 49–52 (2007). — p.29 and 31.

[67] T. Tanabe, M. Notomi, E. Kuramochi, and H. Taniyama, Large pulse delay and small group velocity achieved using ultrahigh-Q photonic crystal nanocavities, Opt. Express **15**, 7826–7839 (2007). — p.29.

[68] C. Weisbuch, M. Nishioka, A. Ishikawa, and Y. Arakawa, Observation of the coupled exciton-photon mode splitting in a semiconductor quantum microcavity, Phys. Rev. Lett. **69**, 3314–3317 (1992). — p.29.

[69] J. Kasprzak, M. Richard, S. Kundermann, A. Baas, P. Jeambrun, J. M. J. Keeling, F. M. Marchetti, M. H. Szymanska, R. André, J. L. Staehli, V. Savona, P. B. Littlewood, B. Deveaud, and L. S. Dang, bose-einstein condensation of exciton polaritons, Nature **443**, 409 (2006). — p.29.

[70] S. Marzenell, R. Beigang, and R. Wallenstein, limitations and guidelines for measuring the spectral width of ultrashort light pulses with a scanning fabry-pérot interferometer, Appl. Phys. B **71**, 185–191 (2000). — p.29 and 65.

[71] F. Erden and O. A. Tretyakov, Excitation by a transient signal of the real-valued electromagnetic fields in a cavity, Phys. Rev. E **77**, 056605 (2008). — p.29.

[72] D. K. Armani, T. J. Kippenberg, S. M. Spillane, and K. J. Vahala, Ultra-high-Q toroid microcavity on a chip, Nature **421**, 925–928 (2003). — p.30.

[73] J. S. Blakemore, Semiconducting and other major properties of gallium arsenide, J. Appl. Phys. **53**, R123–R181 (1982). — p.33, 35, 40, and 54.

[74] R. E. Fern and A. Onton, Refractive Index of AlAs, J. Appl. Phys. **42**, 3499–3500 (1971). — p.33, 40, and 54.

[75] B. E. A. Saleh and M. C. Teich, *Fundamentals of photonics*, Wiley Interscience, New York, 1991. — p.35 and 89.

[76] F. de Martini, M. Marrocco, and D. Murra, Transverse quantum correlations in the active microscopic cavity, Phys. Rev. Lett. **65**, 1853–1856 (1990). — p.38.

[77] B. P. J. Bret, T. L. Sonnemans, and T. W. Hijmans, Capturing a light pulse in a short high-finesse cavity, Phys. Rev. A **68**, 023807 (2003). — p.39.

[78] V. R. Almeida, C. A. Barrios, R. R. Panepucci, and M. Lipson, All-optical control of light on a silicon chip, Nature **431**, 1081–1084 (2004). — p.39 and 40.

[79] Q. Xu, P. Dong, and M. Lipson, Breaking the delay-bandwidth limit in a photonic structure, Nature Phys. **31**, 406–410 (2007). — p.39.

[80] Y. Tanaka, J. Upham, T. Nagashima, T. Sugiya, T. Asano, and S. Noda, Dynamic control of the Q factor in a photonic crystal nanocavity, Nat. Mat. **6**, 862–865 (2007). — p.39.

[81] M. Notomi and S. Mitsugi, Wavelength conversion via dynamic refractive index tuning of a cavity, Phys. Rev. A **73**, 051803 (2006). — p.39, 44, and 71.

[82] A. M. Yacomotti, F. Raineri, C. Cojocaru, P. Monnier, J. Levenson, and R. Raj, Nonadiabatic Dynamics of the Electromagnetic Field and Charge Carriers in High-Q Photonic Crystal Resonators, Phys. Rev. Lett. **96**, 093901 (2006). — p.39 and 44.

[83] M. Först, J. Niehusmann, T. Plötzing, J. Bolten, T. Wahlbrink, C. Moormann, and H. Kurz, High-speed all-optical switching in ion-implanted silicon-on-insulator microring resonators, Opt. Lett. **32**, 2046–2048 (2007). — p.39.

[84] T. Tanabe, K. Nishiguchi, A. Shinya, E. Kuramochi, H. Inokawa, and M. Notomi, Fast all-optical switching using ion-implanted silicon photonic crystal nanocavities, Appl. Phys. Lett. **90**, 031115 (2007). — p.40.

[85] H. M. Gibbs, T. N. C. Venkatesan, S. L. McCall, A. Passner, A. C. Gossard, and W. Wiegmann, Optical Modulation by optical tuning of a cavity, Appl. Phys. Lett. **34**, 511–514 (1979). — p.40.

[86] T. Tanabe, M. Notomi, S. Mitsugi, A. Shinya, and E. Kuramochi, All-optical switches on a silicon chip realized using photonic crystal nanocavities, Appl. Phys. Lett. **87**, 151112 (2005). — p.40.

[87] Q. Xu, V. R. Almeida, and M. Lipson, Micrometer-scale all-optical wavelength converter on silicon, Opt. Lett. **30**, 2733–2735 (2005). — p.40.

[88] I. Fushman, E. Waks, D. Englund, N. Stoltz, P. Petroff, and J. Vučković, Ultrafast nonlinear optical tuning of photonic crystal cavities, Appl. Phys. Lett. **90**, 091118 (2007). — p.40.

[89] P. J. Harding, A. P. Mosk, A. Hartsuiker, Y. -R. Nowicki-Bringuier, J. -M Gerard, W. L. Vos, Time-resolved resonance and linewidth of an ultrafast switched GaAs/AlAs microcavity , ArXiv.org 0901.3855 (2009). — p.14, 40, 44, 53, and 61.

[90] J. M. Gérard, B. Sermage, L. Bergomi, and J. Y. Marzin, Differentiation of the non radiative recombination properties of the two interfaces of MBE grown GaAs-GaAlAs quantum wells, Superlattices and Microstructures **8**, 417 (1990). — p.44.

[91] G. Segschneider, T. Dekorsy, H. Kurz, R. Hey, and K. Ploog, Energy resolved ultrafast relaxation dynamics close to the band edge of low-temperature grown GaAs, Appl. Phys. Lett. **71**, 2779 (1997). — p.45 and 78.

[92] A. Haché and M. Bourgeois, Ultrafast all-optical switching in a silicon-based photonic crystal, Appl. Phys. Lett. **77**, 4089–4091 (2000). — p.51.

[93] S. R. Hastings, M. J. A. d. Dood, H. Kim, W. Marshall, H. S. Eisenberg, and D. Bouwmeester, Ultrafast optical response of a high-reflectivity GaAs/AlAs Bragg mirror, Appl. Phys. Lett. **86**, 031109 (2005). — p.51.

[94] S. W. Leonard, H. M. van Driel, J. Schilling, and R. B. Wehrspohn, Ultrafast band-edge tuning of a two-dimensional silicon photonic crystal via free-carrier injection, Phys. Rev. B **66**, 161102 (2002). — p.51, 52, 64, and 98.

[95] A. D. Bristow, J.-P. R. Wells, W. H. Fan, A. Tahraoui, T. F. Krauss, and J. S. Roberts, Ultrafast nonlinear response of AlGaAs two-dimensional photonic crystal waveguides, Appl. Phys. Lett. **83**, 851 (2003). — p.51.

[96] H. Tan, H. van Driel, S. Schweizer, R. Wehrspohn, and U. Gösele, Nonlinear optical tuning of a two-dimensional silicon photonic crystal, Phys. Rev. B **70**, 205110 (2004). — p.51, 52, 64, and 98.

[97] D. A. Mazurenko, R. Kerst, J. I. Dijkhuis, A. V. Akimov, V. G. Golubev, D. A. Kurdyukov, A. B. Pevtsov, and A. V. Sel'Kin, Ultrafast Optical Switching in Three-Dimensional Photonic Crystals, Phys. Rev. Lett. **91**, 213903 (2003). — p.51.

[98] C. Becker, S. Linden, G. v. Freymann, M. Wegener, N. Tétreault, E. Vekris, V. Kitaev, and G. A. Ozin, Two-color pump-probe experiments on silicon inverse opals, Appl. Phys. Lett. **87**, 091111 (2005). — p.51.

[99] H. Nakamura, Y. Sugimoto, K. Kanamoto, N. Ikeda, K. Inoue, H. Ishikawa, and K. Asakawa, Ultra-fast photonic crystal/quantum dot alloptical switch for future photonic networks, Opt. Express **12**, 6606 (2004). — p.51.

[100] M. F. Yanik and S. Fan, Stopping Light All Optically, Phys. Rev. Lett. **92**, 083901 (2004). — p.51.

[101] S. G. Hense and M. Wegener, Ultrafast switch-off of a vertical-cavity semiconductor laser, Phys. Rev. B **55**, 9255–9258 (1997). — p.52.

[102] X. Hu, P. Jiang, C. Ding, H. Yang, and Q. Gong, Picosecond and low-power all-optical switching based on an organic photonicbandgap microcavity, Nat. Phot. **2**, 185 (2008). — p.52, 64, and 98.

[103] D. A. Mazurenko, R. Kerst, J. I. Dijkhuis, D. A. Kurdyukov, and A. B. Pevtsov, Subpicosecond shifting of the photonic band gap in a three-dimensional photonic crystal, Appl. Phys. Lett. **86**, 041114 (2005). — p.52.

[104] T. G. Euser and W. L. Vos, Spatial homogeneity of optically switched semiconductor photonic crystals and of bulk semiconductors, J. Appl. Phys. **97**, 043102 (2005). — p.52, 60, and 73.

[105] M. Born and E. Wolf, *Principles of Optics*, Cambridge University Press, 4th edition, 1997. — p.54 and 65.

[106] W. C. Hurlbut, Y.-S. Lee, K. L. Vodopyanov, P. S. Kuo, and M. M. Fejer, Multiphoton absorption and nonlinear refraction of GaAs in the mid-infrared, Opt. Lett. **32**, 668 (2007). — p.67 and 69.

[107] M. Dinu, F. Quochi, and H. Garcia, Third-order nonlinearities in silicon at telecom wavelengths, Appl. Phys. Lett. **82**, 2954 (2003). — p.67.

[108] T. Ulmer, R. Tan, Z. Zhou, S. Ralph, R. Kenan, and C. Verber, Two-photon absorption-induced self-phase modulation in GaAs-AlGaAs waveguides for surface-emitted second-harmonic generation, Opt. Lett. **24**, 756 (1999). — p.67.

[109] S. Noda and T. Baba, *Roadmap on Photonic Crystals*, Kluwer, Boston, 2003. — p.71.

[110] R. W. Boyd, *Nonlinear Optics*, Academic press, New York, 2008. — p.71.
[111] P. M. Johnson, B. P. J. Bret, J. Gómez-Rivas, J. J. Kelly, and A. Lagendijk, Anisotropic diffusion of light in a strongly scattering material, Phys. Rev. Lett. **89**, 243901–1–243901–3 (2002). — p.71.
[112] E. J. Reed, M. Soljačić, and J. D. Joannopoulos, Reversed Doppler Effect in Photonic Crystals, Phys. Rev. Lett. **91**, 133901 (2003). — p.71.
[113] T. Rivera, J.-P. Debray, and J. M. Gérard, Optical losses in plasma-etched AlGaAs microresonators using reflection spectroscopy, Appl. Phys. Lett. **74**, 911–913 (1999). — p.81, 87, 89, 95, 96, 111, and 112.
[114] D. Marcuse, *Light transmission optics*, van Nostrand Reinhold company, 1972. — p.84.
[115] A. Yariv and P. Yeh, *Optical Waves in Crystals*, John Wiley & Sons, New York, 1984. — p.84.
[116] W. L. Vos, M. Megens, C. M. van Kats, and P. Bösecke, Transmission and diffraction by photonic colloidal crystals, J. Phys.: Condens. Matter **8**, 9503–9507 (1996). — p.84.
[117] M. Karl, S. Li, T. Passow, W. Löffler, H. Kalt, and M. Hetterich, Localized and delocalized modes in coupled optical micropillar cavities, Opt. Express **15**, 8191–8196 (2007). — p.85.
[118] J.-M. Gérard and B. Gayral, Strong Purcell Effect for InAs Quantum Boxes in Three-Dimensional Solid-State Microcavities, J. Lightwave Technol. **17**, 2089 (1999). — p.112.
[119] B. Gayral and J. M. Gérard, Photoluminescence experiment on quantum dots embedded in a large Purcell-factor microcavity, Phys. Rev. B **78**, 235306 (2008). — p.97, 112, and 117.
[120] H. Rigneault, J. Broudic, B. Gayral, and J. M. Gérard, Far-field radiation from quantum boxes located in pillar microcavities, Opt. Lett. **26**, 1595–1597 (2001). — p.112 and 116.
[121] A. J. Bennett, D. J. P. Ellis, A. J. Shields, P. Atkinson, I. Farrer, and D. A. Ritchie, Observation of the Purcell effect in high-index-contrast micropillars, Appl. Phys. Lett. **90**, 191911 (2007). — p.112.
[122] A. G. Silva, C. A. Parra-Murillo, J. S. V. Valentim, P. T. Morais, F. Plentz, P. S. S. Guimarães, H. Vinck-Posada, B. A. Rodriguez, M. S. Skolnick, A. Tahraoui, and M. Hopkinson, Quantum dot dipole orientation and excitation efficiency of micropillar modes, Opt. Express **16**, 19201–19207 (2008). — p.112.
[123] J. M. Gérard, Solid-State Cavity-Quantum Electrodynamics with Self-Assembled Quantum Dots, Topics Appl. Phys. **90**, 283–327 (2003). — p.97 and 112.
[124] I. S. Nikolaev, P. Lodahl, A. F. van Driel, A. F. Koenderink, and W. L. Vos, Strongly nonexponential time-resolved fluorescence of quantum-dot ensembles in three-dimensional photonic crystals, Phys. Rev. B **75**, 115302 (2007). — p.115.
[125] N. W. Ashcroft and N. D. Mermin, *Solid State Physics*, Brooks/Cole, 1976. — p.119, 120, and 125.
[126] W. H. Zachariasen, *Theory of X-Ray Diffraction in Crystals*, Dover, 1994. — p.119 and 142.
[127] C. Giacovazzo, H. L. Monaco, D. Viterbo, F. Scordari, G. Gilli, G. Zanotti, and M. Catti, *Fundamentals of Crystallography*, Oxford science publications, 1992. — p.119.
[128] L. Poladian, M. Large, W. Padden, K. Lee, S. Wickham, and N. Beeton, Cleo IQEC 2004, 2004. — p.121.
[129] M. Calandra and F. Mauri, High-Tc Superconductivity in Superhard Diamondlike, Phys. Rev. Lett. **101**, 016401 (2008). — p.121 and 125.
[130] B. Edegger, V. N. Muthukumar, C. Gros, and P. W. Anderson, Electronic Structure of Strongly Correlated d-Wave Superconductors, Phys. Rev. Lett. **96**, 207002 (2006). — p.121.

[131] S. Chang and H. Höche, *Multiple Diffraction of X-Rays in Crystals*, Springer-Verlag, 1984. — p.122.

[132] H. M. v. Driel and W. L. Vos, Multiple Bragg wave coupling in photonic band-gap crystals, Phys. Rev. B **62**, 9872–9875 (2000). — p.122.

[133] S. G. Johnson and J. D. Joannopoulos, Block-iterative frequency-domain methods for MaxwellŠs equations in a planewave basis, Opt. Express **8**, 173 (2001). — p.123.

[134] Y. A. Vlasov, X. Z. Bo, J. C. Sturm, and D. J. Norris, On-chip natural assembly of silicon photonic band gap crystals, Nature **414**, 289–293 (2001). — p.123 and 127.

[135] J. E. G. J. Wijnhoven and W. L. Vos, Preparation of photonic crystals made of air spheres in titania, Science **281**, 802–804 (1998). — p.127.

[136] A. Blanco, E. Chomski, S. Grabtchak, M. Ibisate, S. John, S. W. Leonard, C. López, F. Meseguer, H. Míguez, J. P. Mondia, G. A. Ozin, O. Toader, and H. M. v. Driel, Large-scale synthesis of a silicon photonic crystal with a complete three-dimensional bandgap near 1.5 micrometres, Nature **405**, 437–440 (2000). — p.127.

[137] F. Meseguer, A. Blanco, H. Míguez, and F. García-Santamaría, Synthesis of inverse opals, Colloid surface A **202**, 281–290 (2002). — p.127.

[138] J. E. G. J. Wijnhoven, L. Bechger, and W. L. Vos, Fabrication and characterization of large macroporous photonic crystals in titania, Chem.Mater. **13**, 4486–4494 (2001). — p.127.

[139] P. Jiang, J. F. Bertone, K. S. Hwang, and V. L. Colvin, Single-Crystal Colloidal Multilayers of Controlled Thickness, Chem.Mater. **11**, 2132–2140 (1999). — p.127, 128, 134, and 137.

[140] F. Meseguer, Colloidal crystals as photonic crystals, Colloid surface A **270** (2005). — p.127.

[141] W. L. Vos, M. Megens, C. M. v. Kats, and P. Bösecke, X-ray Diffraction of Photonic Colloidal Single Crystals, Langmuir **13**, 6004–6008 (1997). — p.127.

[142] H. Míguez, F. Meseguer, C. López, A. Blanco, J. Moya, J. Requena, and A. Mifsud, Control of the photonic crystal properties of fcc-packed submicrometer SiO_2 spheres by sintering, Adv. Mater. **10**, 480 (1998). — p.127.

[143] M. Holgado, F. García-Santamaría, A. Blanco, M. Ibisate, A. Cintas, H. Míguez, S. J. Serna, C. Molpeceres, J. Requena, A. Mifsud, F. Meseguer, and C. López, Electrophoretic deposition to control artificial opal growth, Langmuir **15**, 4701 (1999). — p.127.

[144] A. S. Dimitrov and K. Nagayama, Continuous convective assembling of fine particles into two-dimensional arrays on solid surfaces, Langmuir **12**, 1303 (1996). — p.127 and 128.

[145] D. J. Norris, Opaline photonic crystals: How does self-assembly work?, Adv. Mater. **16**, 1393 (2004). — p.128 and 140.

[146] J.-F. Galisteo-López and W. L. Vos, Angle resolved reflectivity of single-domain photonic crystals, effects of disorder, Phys. Rev. E **66**, 036616 (2002). — p.128.

[147] J. F. Bertone, P. Jiang, K. S. Hwang, D. M. Mittleman, and V. L. Colvin, Thickness Dependence of the Optical Properties of Ordered Silica-Air and Air-Polymer Photonic Crystals, Phys. Rev. Lett. **83**, 300–303 (1999). — p.128 and 142.

[148] P. Braun, S. Rinne, and F. García Santamaría, Introducing defects in 3D photonic crystals: State of the art, Adv. Mater. **18**, 2665 (2006). — p.128.

[149] C. Allain and L. Limat, Regular patterns of cracks formed by directional drying of a colloid suspension, Phys. Rev. Lett. **74**, 2981 (1995). — p.128, 137, and 139.

[150] K. A. Shorlin, J. R. de Bruyn, M. Graham, and S. W. Morris, Development and geometry of isotropic and directional shrinkage-crack patterns, Phys. Rev. E **61**, 6950 (2000). — p.128, 137, and 139.

[151] E. R. Dufresne, E. I. Corwin, N. A. Greenblatt, X. S. Xie, J. W. Hutchinson, and D. A. Weitz, Flow and Fracture in Drying Nanoparticle Suspensions, Phys. Rev. Lett. **91**, 224501 (2003). — p.128.

[152] H. Li and F. Marlow, Controlled arrangement of colloidal crystal strips, Chem. Mater. **17**, 3809 (2005). — p.128.

[153] E. R. Dufresne, D. J. Stark, N. A. Greenblatt, J. X. Cheng, J. W. Hutchinson, L. Mahadean, and D. A. Weitz, Dynamics of fracture in drying suspensions, Langmuir **22**, 7144 (2006). — p.128.

[154] J. Li, B. Jia, G. Zhou, and M. Gu, Fabrication of three-dimensional woodpile photonic crystals in a PbSe quantum dot composite material, Opt. Express **14**, 10740–10745 (2006). — p.128.

[155] K. B. Singh and M. S. Tirumkudulu, Cracking in Drying Colloidal Films, Phys. Rev. Lett. **98**, 218302 (2007). — p.128, 137, and 139.

[156] A. A. Chabanov, Y. Jun, and J. Norris, Avoiding cracks in self-assembled photonic band-gap crystals, Appl. Phys. Lett. **84**, 3573–3575 (2004). — p.128.

[157] M. Megens, J. E. G. J. Wijnhoven, A. Lagendijk, and W. L. Vos, Light sources inside photonic crystals, J. Opt. Soc. Am. B **16**, 1403–1408 (1999). — p.128.

[158] D. O. Riese, W. L. Vos, G. H. Wegdam, F. J. Poelwijk, D. L. Abernathy, and G. Gr"ubel, Photon correlation spectroscopy: X rays versus visible light, Phys. Rev. E **61**, 1676–1680 (2000). — p.130.

[159] L. Bechger, *Synthesis and Flyorescence of Opal & Air-Sphere Photonic Crystals,* University of Twente, available online: http://www.photonicbandgaps.com, PhD thesis, 2003. — p.133 and 141.

[160] O. Levy and D. Stroud, Maxwell Garnett theory for mixtures of anisotropic inclusions: Application to conducting polymers, Phys. Rev. B **56**, 8035–8046 (1997). — p.157.

[161] A. Kirchner, K. Busch, and C. M. Soukoulis, Transport properties of random arrays of dielectric cylinders, Phys. Rev. B **57**, 277–288 (1998). — p.157.

[162] O. L. Muskens, M. T. Borgström, E. P. A. M. Bakkers, and J. Gómez Rivas, Giant optical birefringence in ensembles of semiconductor nanowires, Appl. Phys. Lett. **89**, 233117 (2006). — p.157.

APPENDIX A

Center frequency versus Si filling fraction

An analytic expression to calculate the center frequency of the stopband is useful to provide physical insight, and also since bandstructure calculations are time consuming. A useful input for such an expression is the long wavelength limit of the refractive index [16]. The long wavelength limit for the refractive index for cylinders of material with a low refractive index in silicon is given by the Maxwell-Garnett equations [160–162]. For TE waves (E-field perpendicular to pores),

$$n_{TE}^2 = 1 + \frac{2\Phi\alpha}{1-\Phi\alpha}, \tag{A.1}$$

where n_{TE} is the refractive index of the crystal for TE waves, Φ is the volume fraction of silicon, $\alpha = \frac{n_{Si}^2-1}{n_{Si}^2+1}$ and n_{Si} is the refractive index of silicon. The refractive index for TM waves, n_{TM} is given by

$$n_{TM}^2 = (1-\Phi)n_{Si}^2 + \Phi n_{Air}^2, \tag{A.2}$$

where n_{Air} is the refractive index of air. The center frequency of the stop band in the $\Gamma - K$ direction, calculated with Eq. A.1 and Eq. A.2, is given in figure A.1. Figure A.1 shows a good agreement between the position of the first order stopband estimated with the long wavelength limit refractive index and position from the measurements.

We conclude that the refractive index calculated with the Maxwell-Garnett relations give a good estimate for the position of the first order stopband. Furthermore, we conclude from figure A.1 that the photonic crystal is birefringent.

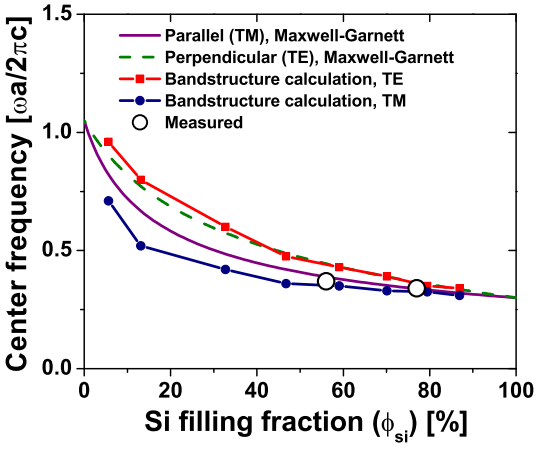

FIGURE A.1: *Center frequency as a function of silicon volume fraction derived from bandstructure calculations (connected symbols) and estimated with the Maxwell-Garnet equations (lines) , for the K point in the Brillouin zone. The frequency is calculated for both TM and TE waves. The center frequency shifts to red for an increasing volume fraction as expected.*

APPENDIX B

Photonic strength

The relative linewidth of a Bragg reflection can be calculated with the use of the photonic parameter S that is derived from dynamical theory of X-ray diffraction [16, 18]. The photonic parameter S is defined as

$$S = 3\Phi \frac{m^2 - 1}{m^2 + 2} g(k, r), \tag{B.1}$$

where Φ is the filling fraction, $m = \frac{n_{Si}}{n_{Air}}$, and $g(k, r)$ is the structure factor, which is given for a cylinder by [62]

$$g(k, r) = \frac{2J_1(u)}{u}, \tag{B.2}$$

where $u = kr$, with r the radius of the cylinder and k the scattering vector given by $k = \frac{4\pi n_{eff}}{\lambda_c}$. With n_{eff} the effective refractive index and λ_c the center wavelength of the stopband.

According to Eq. B.1, the photonic strength is equal to 31% for the $\Gamma - K$ reflection and 17% for the Bragg reflection ($\Gamma - B$ reflection). From the measurements we obtain a width of 15% for the $\Gamma - K$ reflection and 19% for the Bragg reflection. The measured width of the $\Gamma - K$ reflection is smaller than the calculated one, while the measured width of the Bragg reflection agrees very well with the calculated width.

We conclude that the S-parameter gives a good measure for the spectral width of the Bragg peak. For the reflections due to the Von Laue condition the S-parameter in our case does not give an accurate estimate.

Nederlandse samenvatting

Dit proefschrift gaat over het opsluiten en manipuleren van licht in een optische trilholte. Een optische trilholte bestaat uit twee spiegels waartussen een staande lichtgolf kan bestaan. In een optische trilholte kan licht worden opgeslagen. Met behulp van een korte lichtpuls kan de trilholte worden opgeladen, als de lichtpuls verdwenen is blijft een staande golf in de trilholte achter. Doordat licht door de spiegels van de trilholte lekt, neemt de lichtintensiteit in de trilholte exponentieel af. Dit kan worden vergeleken met het aanslaan van een harmonische oscillator.

Een optische trilholte kan worden gevormd door metallische spiegels of door regelmatig gestructureerde diëlektrische materialen met een periode in de orde van de golflengte van het licht: fotonische kristallen. Omdat fotonische kristallen het licht beter reflecteren dan metallische spiegels zijn deze gewild voor optische trilholtes. Fotonische kristallen kunnen zowel een-, twee- of drie-dimensionaal zijn. Dat wil zeggen dat ze licht in een, twee of drie dimensies kunnen opsluiten als er een optische trilholte in het kristal wordt gemaakt. In hoofdstuk 9 worden twee-dimensionale kristallen besproken. In hoofdstuk 10 worden drie-dimensionale fotonische kristallen gemaakt van regelmatig gestapelde bolletjes glas, ook wel opalen genoemd, besproken.

Een alternatieve manier om het licht in drie dimensies op te sluiten wordt besproken in hoofdstuk 7. In dit hoofdstuk laten we zien dat we specifieke resonanties in een zogenaamde micropilaar kunnen aanslaan. Micropilaren zijn cilindervormige trilholtes met een-dimensionale spiegels aan de boven en onderkant van de spiegel. Het aanslaan van micropilaar resonanties is vergelijkbaar met het aanslaan van resonanties van een trommel. De plaats op de trommel waar geslagen wordt, bepaalt op welke resonantie frequentie het trommel vel gaat trillen.

In dit proefschrift laten we verder experimenten zien aan trilholtes met een-dimensionale fotonische kristal spiegels. Hoe lang licht in zo'n optische trilholte kan worden opgeslagen bestuderen we in hoofdstuk 3.

Om het licht te kunnen opsluiten en loslaten op commando schakelen we de optische trilholtes met hoog energetische laser pulsen. Het schakel proces monitoren we met behulp van de reflectie van laserpulsen. Uit de reflectie van die laserpulsen halen we informatie over de toestand van de trilholte. De optische trilholte kan geschakeld worden door vrije ladingsdragers in het diëlektricum te genereren zoals we laten zien in hoofdstuk 4. De brekingsindex hangt af van de concentratie van vrije ladingsdragers. Door de extra vrije ladingsdragers die gegenereerd worden door de laser puls verandert de brekingsindex en daarmee de optische eigenschappen van de trilholte. De tijdschaal van deze manier van schakelen is gelimiteerd door de recombinatie van vrije ladingsdragers, die bepaald wordt door materiaal eigenschappen van het diëlektricum. Door recombinatie van de vrije ladingsdragers verandert de ladingsdragers concentratie en daarmee de brekingsindex. Pas als alle vrije ladingsdragers zijn gerecombineerd is de trilholte weer in zijn oorspronkelijke, ongeschakelde toestand.

We laten in hoofdstuk 5 als eerste ter wereld zien dat het ultiem snel schakelen van de fotonische trilholte mogelijk is door gebruik te maken van het electronische Kerr effect. Bij deze manier van schakelen verandert de trilholte enkel als er een hoog energetische laser puls aanwezig is in het materiaal. Door de hoog energetische laser puls wordt de brekings index namelijk instantaan verhoogd. Zodra de puls weg is, heeft de brekingsindex weer zijn initiële waarde, in tegenstelling tot het schakelen met vrije ladingsdragers. De tijdschaal van deze manier van schakelen wordt beperkt door de duur van de laser puls en is typisch 100-500 keer sneller dan het schakelen met behulp van vrije ladingsdragers. Deze snelheid biedt mogelijkheden voor het moduleren van data met een frequentie van meer dan 1 THz.

Een toepassing van het optisch schakelen van een trilholte laten we zien in hoofdstuk 6. In dit hoofdstuk veranderen we in een experiment de kleur van licht door het op te sluiten in een trilholte waarvan de eigenschappen heel snel veranderen. Deze methode is anders dan de bestaande methoden voor het veranderen van de kleur van licht omdat de laser puls waardoor de eigenschappen van de trilholte veranderen niet tegelijkertijd aanwezig is met het licht dat van kleur wordt verandert. Er worden namelijk eerst vrije ladingsdragers gegenereerd die er voor zorgen dat de eigenschappen van de trilholte veranderen. Als de eerste laser puls allang weg is veranderen de eigenschappen van de trilholte nog steeds door het recombineren van de vrije ladingsdragers. Op dit moment wordt er licht in de trilholte opgeslagen door een tweede laser puls. Het licht van de twee laser puls verandert nu van kleur.

Een tweede mogelijke toepassing van het optisch schakelen van een trilholte bespreken we in hoofdstuk 8. In dit hoofdstuk laten we door middel van een theoretisch model zien dat we het uitzenden van licht door lichtbronnen in de trilholte kunnen beïnvloeden door de eigenschappen van de trilholte te laten veranderen. Zonder het schakelen van de trilholte zenden de lichtbronnen fotonen uit binnen een bepaalde tijd (de levensduur van de lichtbron) na het exciteren van de bronnen, maar precies wanneer is niet te voorspellen. Het is wel te voorspellen binnen welke tijd de kans dat het foton uitgezonden bijna 1 is. Door tijdens de tijd dat de lichtbron uit kan zenden de eigenschappen van de trilholte te schakelen kan er voor worden gezorgd dat de meeste bronnen gaan uitzenden tijdens het schakelen. Hierdoor wordt een zekere mate van determinisme gebracht in het normaal gesproken onvoorspelbare proces. We laten zien in hoofdstuk 8 dat het schakelen van het uitgezonden licht van de lichtbronnen een zeer intense lichtpuls oplevert.

Dankwoord

Het werk van een OIO werkend aan een project in de optica is vaak eenzaam. Het wordt grotendeels uitgevoerd in een donker, koel lab en meetsessies tot diep in de nacht zijn niet ongebruikelijk. Als de OIO na zo'n sessie huiswaarts keert terwijl de stad ligt te slapen bepalen de resultaten van die avond het gemoed, varierend van triomfantelijk en tevreden tot teleurgesteld. Bij thuiskomst, de volgende ochtend of dagen later zijn familie, vrienden en collega's onmisbaar. Zij delen de succesverhalen, zijn er om een hart onder de riem te steken of helpen met het oplossen van praktische problemen en fysische vraagstukken. Dit laatste hoofdstuk is geschreven om deze mensen, zonder wie dit proefschrift niet tot stand zou zijn gekomen en zonder wie de afgelopen vier jaar een stuk minder leuk zouden zijn geweest, te bedanken.

Willem, als dagelijks begeleider wil ik je bedanken voor de opleiding die je me de afgelopen vier jaar hebt gegeven. Ik heb veel van je geleerd en met plezier met je samengewerkt. Naast je tomeloze enthousiasme is voor mij een typische eigenschap van jou, het altijd stellen van de volgende vraag.

Ad, ik heb veel van je geleerd, zowel van fysica als op persoonlijk vlak. Bedankt voor de diverse keren terugkoppeling na presentaties. Daarnaast wil ik je bedanken voor de levendige discussies tijdens de lunch, die waren altijd een waar genoegen.

Allard, bedankt voor je vele advies en je bijdragen aan dit proefschrift. Het blijft voor mij onvoorstelbaar hoe snel je een probleem weet aan te pakken en richting een oplossing weet te sturen.

Jean-Michel, Julien, Yoanna-Reinne, thanks for making the wonderful samples, without which 75 % of this thesis would not exist. Thank you for the cooperation, I am very grateful that you were always ready to answer questions on physics.

Bedankt Léon en Willem, voor het maken van de mooie 2D en 3D structuren. Zonder fib- en ets koningen zoals jullie in je groep ben je als OIO nergens. Léon, bedankt voor de het leren groeien van opalen en nogmaals excuses voor die plas KOH in je lab.

Georgios, bedankt voor het vele leeswerk en de mooie experimenten die je hebt gedaan. Philip, bedankt voor het overdragen van het experiment, het leren van de fijne kneepjes van de switch opstelling en je mooie metingen.

Naast zelf meten heb ik het genoegen mogen proeven om een afstudeerstudent te mogen begeleiden. Edwin, ik vind dat je heel erg goed werk hebt afgeleverd. Het heeft geleid tot een hoofdstuk in dit proefschrift en zal ook worden verwerkt tot een artikel. Ik vond het een leerzame en leuke ervaring.

Ik wil mijn kamergenoten Patrick en Paolo bedanken voor de vele discussies, die in het algemeen meer over taal dan over natuurkunde gingen. Paolo (e anche Eleonora, Birgin e Salvatore), grazia per i lezioni Italiani e grazia per parlare lentemente en italiano per me. Ho imparato molto e espero che posso leggere una gazetta dopo poche tempo. Tijmen, als oud kamergenoot, bedankt voor de leuke voetbalwedstrijden en je advies gedurende de eerste jaren van mijn promotie. Bart, bedankt dat je mijn paranimf wilt zijn en bedankt voor de hulp met de spectrometer. Je staat altijd klaar voor mensen die een vraag of probleem hebben. Bedankt ook daarvoor. Merel, ik heb veel plezier beleefd aan onze reizen van Enschede naar Amsterdam. Ivo, de sporadische avonden in de kroeg waren een genoegen. Bernard, bedankt voor je geduld bij het uitleggen van theorie en de tijd die je altijd vond om vragen te beantwoorden.

For the conversations during lunch, coffee and other times I want to thank the members of PhoGap, PhoScat and COPS: Ad, Adriaan, Bart, Bas, Bernard, Birgin, Charles, Cock, Danang, Dimitry, Edwin, Elbert, Georgios, Hakki, Hannie, Ivan, Ivo, Iwert, Jochen, KaMo, KaMu, Léon, Merel, Niels, Oscar, Otto, Paolo, Patrick, Pedro, Philip, Rajesh, Ramy, Raymond, Sanli, Simon, Steven, Tijmen, Timmo, Tom, Elbert, Willem T., Willem V.,

For the interesting and sometimes heated Thursday morning sessions I want to thank the members of the Center for Nanophotonics. Presenting my work for such a critical audience was very useful and instructive.

Daarnaast wil ik mensen bedanken die door hun ondersteunende werk de afgelopen vier jaar heel veel makkelijker hebben gemaakt. Cock, Ed, Idsart, Iwert, Justine, Karen, Rob Kemper, Rob Troost en Sjoerd, bedankt.

Met het eindigen van mijn promotie periode eindigt ook mijn periode in de centrale ondernemingsraad van FOM (COR) en de ondernemingsraad van AMOLF (ORA). Ik heb er veel geleerd en bedank zowel de leden van de ORA als de COR hiervoor. Betty,

Justine, Maaike, Miranda en Wouter (ORA), Barend, Dick, Egge, Hajnal, Harm, Henk, Ineke, Johan, Maaike, Niels, Ron, Ruth en Yuk Man (COR), bedankt.

De leden van de boks- en schermvereniging wil ik bedanken voor de sparringspartijen die voor voldoende ontspanning hebben gezorgd. Ook bedankt voor alle blauwe plekken en schrammen, waarover ik uitleg heb moeten geven bij de lunch en koffie. In het bijzonder wil ik David, Evelien, Gati, Hein, Henriette, Jacco, Joren, Lorentz, Maarten, Marie-Christine, Paul, Salvatore (buon divertire in Valencia e spero che ci vediamo fra poco.) en Vico bedanken.

Voor de motiverende kroegavonden op verschillende locaties wil ik Arno, Gerbert, Hein, Marcus, Mark, Salvatore, Thijs, Tiemen en Victor bedanken. Martin en Meike, bedankt voor de avondjes Bimhuis. Voor steun met raad en daad wil ik in het bijzonder Doenja bedanken. Bedankt voor de fijne tijd, je bent onmisbaar. Tot slot wil ik mijn ouders en broer speciaal bedanken. Pap, Mam en Rob, bedankt voor jullie steun, het luisterend oor en vooral de goeie tijd samen.